

**WL-TR-95-4083**

**CERAMIC BEARING SPECIMEN  
TECHNOLOGY**



**C. JAMES SHIH  
JOHN W. MCCOY  
ANDRE EZIS**

**CERCOM, INC.  
1960 WATSON WAY  
VISTA CA 92083**

**DECEMBER 1993**

**INTERIM REPORT FOR 02/01/92 -- 07/01/93**

**DTIC QUALITY INSPECTED 2**

**Approved for public release; distribution unlimited**

**19961113 162**


**MATERIALS DIRECTORATE  
WRIGHT LABORATORY  
AIR FORCE MATERIEL COMMAND  
WRIGHT-PATTERSON AIR FORCE BASE, OH 45433-7734**

## NOTICE

When government drawings, specifications, or other data are used for any purpose other than in connection with a definitely related government procurement operation, the United States Government thereby incurs no responsibility nor any obligation whatsoever; and the fact that the government may have formulated, furnished, or in any way supplied the said drawings, specifications, or other data, is not to be regarded by implication or otherwise as in any manner licensing the holder or any other person or corporation, or conveying any rights or permission to manufacture, use, or sell any patented invention that may in any way be related thereto.

This report is releasable to the National Technical Information Service (NTIS). At NTIS, it will be available to the general public, including foreign nations.

This technical report has been reviewed and is approved for publication.

  
KARL R. MECKLENBURG, Project Engineer  
Nonstructural Materials Branch  
Nonmetallic Materials Division

  
KENT J. EISENTRAUT, Chief  
Nonstructural Materials Branch  
Nonmetallic Materials Division

  
CHARLES E. BROWNING, Chief  
Nonmetallic Materials Division  
Materials Directorate

If your address has changed, if you wish to be removed from our mailing list, or if the addressee is no longer employed by your organization, please notify WL/MLBT, Bldg 654, 2941 P Street, Suite 1, Wright-Patterson AFB OH 45433-7750 to help maintain a current mailing list.

Copies of this report should not be returned unless return is required by security considerations, contractual obligations, or notice on a specific document.

REPORT DOCUMENTATION PAGE			Form Approved OMB No. 0704-0188	
<small>Public reporting burden for this collection of information is estimated to average 1 hour per response, including the time for reviewing instructions, searching existing data sources, gathering and maintaining the data needed, and completing and reviewing the collection of information. Send comments regarding this burden estimate or any other aspect of this collection of information, including suggestions for reducing this burden, to Washington Headquarters Services, Directorate for Information Operations and Reports, 1215 Jefferson Davis Highway, Suite 1204, Arlington, VA 22202-4302, and to the Office of Management and Budget, Paperwork Reduction Project (0704-0188), Washington, DC 20503.</small>				
1. AGENCY USE ONLY (Leave blank)		2. REPORT DATE DEC 1993		3. REPORT TYPE AND DATES COVERED INTERIM 02/01/92 -- 07/01/93
4. TITLE AND SUBTITLE CERAMIC BEARING SPECIMEN TECHNOLOGY			5. FUNDING NUMBERS C: F33615-92-C-5903 PE 62712 PR 8355 TA 00 WU 01	
6. AUTHOR(S) C. JAMES SHIH JOHN W. MCCOY ANDRE EZIS				
7. PERFORMING ORGANIZATION NAME(S) AND ADDRESS(ES) CERCOM, INC. 1960 WATSON WAY VISTA CA 92083			8. PERFORMING ORGANIZATION REPORT NUMBER	
9. SPONSORING/MONITORING AGENCY NAME(S) AND ADDRESS(ES) MATERIALS DIRECTORATE WRIGHT LABORATORY AIR FORCE MATERIEL COMMAND WRIGHT PATTERSON AFB OH 45433-7734 POC: K. R. MECKLENBURG, WL/MLBT, WPAFB OH, 937-255-2465			10. SPONSORING/MONITORING AGENCY REPORT NUMBER  WL-TR-95-4083	
11. SUPPLEMENTARY NOTES				
12a. DISTRIBUTION AVAILABILITY STATEMENT  APPROVED FOR PUBLIC RELEASE; DISTRIBUTION IS UNLIMITED			12b. DISTRIBUTION CODE	
13. ABSTRACT (Maximum 200 words) A MANUFACTURING PROCESS FOR A SILICON NITRIDE BEARING MATERIAL IS DEVELOPED. THE PROCESS INVOLVES POWDER HOMOGENIZATION, PRE-NITRIDING, HIGH-SPEED GREEN MACHINING, REACTION BONDING, PRESSURELESS SINTERING AND CONTAINERLESS HOT ISOSTATIC PRESSING. EXTENSIVE EXPERIMENTAL AND ANALYTICAL TASKS ARE PERFORMED IN EACH PROCESS STEP TO DEVELOP A LOW-COST, RELIABLE SILICON NITRIDE BEARING MATERIAL WITH A UNIFORM MICROSTRUCTURE AND A PREMIUM QUALITY.  LOW-COST SILICON POWDER IS USED AS A RAW MATERIAL. A QUALITY ASSURANCE PROCEDURE IS DEVELOPED TO EXAMINE THE POWDER HOMOGENEITY IN THE BLENDED POWDER. CONDITIONS FOR THE PRE-NITRIDING ARE DEFINED TO PROVIDE POWDER COMPACTS WITH SUFFICIENT STRENGTH FOR THE HIGH-SPEED GREEN MACHINING. THE REACTION BONDING PROCESS CONVERTS SILICON TO SILICON NITRIDE COMPLETELY. IT IS DEMONSTRATED THAT SILICON NITRIDE CAN BE SINTERED IN A NON-REACTIVE GAS ENVIRONMENT. PROCESSING PARAMETERS FOR THE HOT ISOSTATIC PRESSING ARE OPTIMIZED TO CONTROL THERMAL DECOMPOSITION AND GAS DISSOLUTION-EVOLUTION REACTIONS TO FABRICATE THE PORE-FREE BEARING MATERIAL WITHOUT USING A GLASS ENCAPSULANT.				
14. SUBJECT TERMS SILICON NITRIDE, CERAMIC BEARINGS, HIGH SPEED GREEN MACHINING, CONTAINERLESS HOT ISOSTATIC PRESSING, POWER HOMOGENEITY, PROCESS			15. NUMBER OF PAGES 169	
			16. PRICE CODE	
17. SECURITY CLASSIFICATION OF REPORT UNCLASSIFIED	18. SECURITY CLASSIFICATION OF THIS PAGE UNCLASSIFIED	19. SECURITY CLASSIFICATION OF ABSTRACT UNCLASSIFIED	20. LIMITATION OF ABSTRACT SAR	

# TABLE OF CONTENTS

FOREWORD.....	xiii
LIST OF FIGURES .....	vi
LIST OF TABLES.....	x
1.0 INTRODUCTION.....	1
2.0 EQUIPMENT AND PROCEDURES.....	11
2.1 Powder Blending.....	12
2.2 Cold Isostatic Pressing .....	12
2.3 Centerless Grinding.....	13
2.4 Prenitriding and Nitride Reaction Bonding.....	15
2.5 Sintering .....	18
2.6 Hot Isostatic Pressing (HIPing).....	19
3.0 EXPERIMENTAL RESULTS: MATERIALS AND PROCESS OPTIMIZATION.....	23
3.1 Selection and Characterization of Raw Materials .....	23
3.2 Powder Blending.....	25
3.2.1 Introduction .....	25
3.2.2 Yttria Comminution .....	26
3.2.3 Homogenization DOE No. 1.....	28
3.2.4 Homogenization DOE No. 2.....	31
3.2.5 Ball-Milling Time.....	36
- 3.3 Cold Isostatic Pressing .....	37
3.4 Prenitriding .....	39
3.5 Green Machining .....	43
3.6 Nitriding .....	53
3.7 Sintering .....	61
3.7.1 Baseline Data Development .....	62
3.7.2 Sintering Taguchi Matrix .....	64
3.8 Hot Isostatic Pressing.....	67
3.8.1 Preliminary HIP cycle development .....	71
3.8.1.1 Microstructure and Properties Characterization.....	74



3.8.1.2	Two-toned cross sections .....	77
3.8.1.3	Influence of TiO <sub>2</sub> on $\beta$ -Si <sub>3</sub> N <sub>4</sub> Grain Morphology .....	78
3.8.1.4	Property Determination .....	84
3.8.1.5	Phase Identification and Chemical Analysis .....	85
3.8.2	First DOE for HIPing.....	87
3.8.2.1	Sintering Kinetics.....	88
3.8.2.2	HIPed Density .....	90
3.8.2.3	Microstructures.....	91
3.8.2.4	Hardness and Fracture Toughness.....	93
3.8.3	Evaluation of Furnace Environment .....	96
3.8.3.1	Microstructural Evaluation.....	96
3.8.3.2	Characterization of Microstructure .....	98
3.8.3.3	Hardness and Toughness .....	101
3.8.3.4	Chemical and Crystallographic Analysis.....	103
3.8.4	Second DOE for HIP Optimization .....	109
3.8.5	Summary of HIP Optimization Studies .....	115
4.0	CHARACTERIZATION OF DELIVERABLE MATERIALS .....	117
4.1	Mechanical Properties .....	117
4.2	Microstructure .....	119
4.3	Dimensional Variation .....	121
4.4	X-Ray Inspection.....	122
4.4.1	The Micro CT Technique.....	123
4.4.2	Inspection of In-Process Materials .....	124
4.4.3	Inspection of Deliverable RCF Specimens.....	130
5.0	SUMMARY .....	133
5.1	Powder Blending.....	136
5.2	Cold Isostatic Pressing.....	137
5.3	Pre-nitriding.....	137
5.4	Green Machining.....	138
5.5	Nitriding.....	139

5.6 Sintering .....	139
5.7 Hot Isostatic Pressing .....	140
5.8 Characterization of Final Materials .....	141
REFERENCES .....	142
APPENDIX A: Selection of Methods for Quality Assurance Procedure for Homogeneity .....	143
APPENDIX B: Evaluation Method for Classifying Microstructures .....	151

# LIST OF FIGURES

	Page
Figure 2.1	On the right half of the photograph, a technician is shown lowering a basket containing a part into the cold isostatic press . 13
Figure 2.2	The Glebar centerless grinder used by Cercom to grind rods and balls ..... 14
Figure 2.3	The special grinding wheel used in the centerless grinder for producing balls from rods ..... 15
Figure 2.4	The Cercom-designed cold-walled nitriding furnace..... 16
Figure 2.5	Cercom's sintering furnace ..... 19
Figure 3.1	Average percentage of white area in BSE images as a function of solvent, $Y_2O_3$ grade, and titania..... 30
Figure 3.2	Average white area in BSE images as a function of $Y_2O_3$ material, 40 $\mu m$ filter or no filter, and solvent for the 2nd Homogenization DOE ..... 33
Figure 3.3	Average surface concentration of $Y_2O_3$ particles $\geq 10 \mu m$ as a function of $Y_2O_3$ material, 40 $\mu m$ filter or no filter, and solvent for the 2nd Homogenization DOE ..... 36
Figure 3.4	The multiple-rod isopress bag assembly ..... 38
Figure 3.5	The measured relationship between isostatic pressing pressure and the resulting density of the silicon powder blend compact ..... 39
Figure 3.6	— Average machining yield as a function of regulating wheel type, regulating wheel feed rate, weight gain, and composition ..... 51
Figure 3.7	Average machining yield as a function of feed rate, weight gain, regulating wheel and composition. Only data from trials with the rubber regulating wheel were considered ..... 53
Figure 3.8	The $\alpha / \beta$ Phase Ratio vs. Aluminum Content in $Si_3N_4$ after full nitriding treatment..... 59
Figure 3.9	The $\alpha / \beta$ Phase Ratio vs. Oxygen Content in $Si_3N_4$ after full nitriding treatment..... 59
Figure 3.10	X-ray angular intensity spectrum from program material after nitriding ..... 60
Figure 3.11	Optical micrograph (bright field illumination) of 6/3/2 HIPed $Si_3N_4$ at 200X..... 64

Figure 3.12	Flow diagram of possible hot isostatic pressing (HIPing) procedures. Cercom's process of choice is the sinter-HIP technique using RBSN processing (shaded route).....	67
Figure 3.13	A map of temperature-pressure space in the HIPing process.....	69
Figure 3.14	Relative densities after HIPing as a function of those before HIPing in $\text{Si}_3\text{N}_4$ containing various amounts of $\text{Al}_2\text{O}_3$ , $\text{Y}_2\text{O}_3$ , $\text{TiO}_2$ and $\text{AlN}$ additives. HIPing conditions are 1825°C and 5000 psi.....	72
Figure 3.15	BSE Micrograph of sintered 6/3/2 at 1000X.....	75
Figure 3.16	BSE Micrograph of sintered 6/3/2 at 5000X.....	75
Figure 3.17	EDX spectrum from Area #1 in Figure 3.16 .....	76
Figure 3.18	EDX spectrum from Area #2 in Figure 3.16 .....	76
Figure 3.19	BSE micrograph of HIPed 6/3/2 in dark region.....	78
Figure 3.20	BSE micrograph of HIPed 6/3/2 in light region.....	79
Figure 3.21	BSE micrograph of 6/3/2 before HIP .....	80
Figure 3.22	BSE micrograph of 6/3/2 after HIP .....	81
Figure 3.23	BSE micrograph of HIPed 6/3/2 .....	81
Figure 3.24	BSE micrograph of HIPed 8/2/2 .....	82
Figure 3.25	BSE micrograph of HIPed 8/1/2 .....	82
Figure 3.26	BSE micrograph of HIPed 5/2/3 .....	83
Figure 3.27	BSE micrograph of HIPed 6/3 .....	83
Figure 3.28	BSE micrograph of HIPed 4/4/1/3 .....	84
Figure 3.29	Sintered density vs. sintering time at 1700°C in inert gas for various program compositions .....	89
Figure 3.30	Relative densities of varying $\text{Si}_3\text{N}_4$ compositions after HIPing at 1850°C as a function of those before HIPing .....	90
Figure 3.31	Relative densities of varying $\text{Si}_3\text{N}_4$ compositions after HIPing at 1750°C as a function of those before HIPing .....	91
Figure 3.32	XRD on the fibrous residues in HIPing using $\text{Cr K}\alpha$ 2 radiation. $\alpha$ : $\alpha$ - $\text{Si}_3\text{N}_4$ ; $\beta$ : $\beta$ - $\text{Si}_3\text{N}_4$ ; O: $\text{SiO}_2$ .....	92
Figure 3.33	SEM/BSE micrograph of 8/2/2 $\text{Si}_3\text{N}_4$ HIPed at 1850°C .....	94
Figure 3.34	SEM/BSE micrograph of 8/2/2 $\text{Si}_3\text{N}_4$ HIPed at 1775°C .....	95

Figure 3.35	Micrograph of 4/4/1/3 from HIP Run C at 200X showing Class I microstructure.....	100
Figure 3.36	Micrograph of 8/1/2 from HIP Run C at 200X showing Class II microstructure with low metallic phase content .....	100
Figure 3.37	Micrograph of 5/2/3 from HIP Run C at 200X showing Class II microstructure with high metallic-phase content.....	101
Figure 3.38	Microhardness and fracture toughness requirement.....	102
Figure 3.39	The O/Si ratio in $\text{Si}_3\text{N}_4$ after each processing step .....	105
Figure 3.40	The $\alpha$ / $\beta$ phase ratio vs. aluminum content in $\text{Si}_3\text{N}_4$ after full nitriding treatment.....	107
Figure 3.41	The $\alpha$ / $\beta$ phase ratio vs oxygen content in $\text{Si}_3\text{N}_4$ after full nitriding treatment.....	108
Figure 3.42	The N / Si Ratio of materials of various compositions during each processing step.....	108
Figure 3.43	An optical micrograph of the porosity within one of the white streaks near the surface of the silicon nitride part .....	110
Figure 3.44	An optical micrograph of the volume porosity typical within the vein-like areas in certain of the silicon nitride materials.....	111
Figure 3.45	Average response of hardness to HIP parameters.....	114
Figure 3.46	Average response of toughness to HIP parameters.....	114
Figure 4.1	Weibull plot of flexural strength test results on deliverable material.....	118
Figure 4.2	Optical micrograph of a polished section from a sintered and HIPed silicon nitride ball. Magnified 200 X.....	119
Figure 4.3	SEM micrograph using back-scattered electron imaging of a polished cross section of a sintered and HIPed silicon nitride ball .....	120
Figure 4.4	The Contrast Dose Detail chart shows flaw detectability of the CT systems optimized for ceramic inspection. The HiRes system detects cracks measuring $0.3\text{ }\mu\text{m} \times 1\text{ mm}$ and $55\text{ }\mu\text{m}$ voids .....	124
Figure 4.5	CT slice of 14 mm nitrided sample .....	126
Figure 4.6	CT slice of 12.5 mm sintered samples.....	127
Figure 4.7	High resolution CT of near-surface void in nitrided sample 8/2/2 #2.....	128

Figure 4.8	High-resolution CT of near-surface, high-density inclusion in nitrided sample 6/3/2 #2 .....	128
Figure 4.9	HiRes CT of sintered part (8/2/2 #2) showing annular density variations of 0.1% .....	130
Figure 4.10	A typical example of a x-ray tomographic image of the deliverable RCF specimens .....	132
Figure A.1	Properly adjusted BSE image.....	147
Figure A.2	Grid for measuring white area of BSE imaging .....	147
Figure A.3	Traverse pattern for counting large bright spots in BSE images ..	148
Figure A. 4	EDXS photo for Ti of a sample with acceptable homogeneity of $\text{TiO}_2$ .....	149
Figure A.5	EDXS map of Al in a sample with acceptable homogeneity of $\text{Al}_2\text{O}_3$ . The image has only one bright area .....	150
Figure B.1	Optical micrograph of a polished PSX $\text{Si}_3\text{N}_4$ cross-section taken at 200X. The black and white "dots" constitute porosity and ceramic second phase, respectively. This microstructure is representative of a Class II material .....	154
Figure B.2	Optical micrograph of a polished PSG-H $\text{Si}_3\text{N}_4$ cross-section at 200X. The white "dots" represent the distribution of ceramic second phase. Absence of black "dots" shows that virtually all porosity has been eliminated during HIP treatment. The microstructure is representative of a Class I material .....	155

# LIST OF TABLES

	Page
Table 1.1 Potential Benefits of Ceramics in Bearings.....	3
Tabel 1.2 Ceramic Bearing Applications.....	4
Table 3.1 Powder Characterization Methods.....	24
Table 3.2 Powders Selected for Use in Program.....	24
Table 3.3 Particle Size of 48-hour-milled Molycorp 5600 $Y_2O_3$ as a Function of Media-to-Powder Ratios .....	27
Table 3.4 Factors and Levels for the First Homogenization DOE .....	28
Table 3.5 Taguchi Array for the First Homogenization DOE .....	29
Table 3.6 Factors and Levels for the Second Homogenization DOE .....	31
Table 3.7 Taguchi Array for the Second Homogenization DOE .....	31
Table 3.8 Taguchi Array for the 2nd Homogenization DOE. Also Listed Are the Results of the BSE Analyses in White Area and Surface Concentration of $Y_2O_3$ Particles $\geq 10 \mu m$ .....	34
Table 3.9 Results of BSE Analysis of NYC $Y_2O_3$ Agglomerates for Varying Milling Times on a 6/3 Silicon Metal Composition .....	37
Table 3.10 Weight Gain from Thermal Treatment (wt. %).....	41
Table 3.11 Quantitative Oxygen and Nitrogen Analysis by ICP for Selected Centerless Ground Rods Used in Machining Yield DOE .....	42
Table 3.12 Oxygen Content as a Function of Composition for Rods Used in Machining Yield DOE .....	43
Table 3.13 Factors Chosen for the DOE for prenitriding and green machining .....	44
Table 3.14 Taguchi DOE Array for Prenitriding and Machining.....	46
Table 3.15 Conditions for the Machining Yield Test Matrix and Corresponding Results .....	47
Table 3.16 Machining Yield as a Function of Regulating Wheel Type.....	48
Table 3.17 Machining Yield as a Function of Regulating Wheel Type and Regulating Wheel Speed .....	48
Table 3.18 Machining Yield as a Function of Regulating Wheel Type and Regulating Wheel Feed Rate.....	49

Table 3.19	Machining Yield as a Function of Regulating Wheel Type and Pre-nitriding Cycle .....	49
Table 3.20	Machining Yield as a Function of Regulating Wheel Type and Composition .....	49
Table 3.21	Percent Contribution of All Factors to Machining Yield .....	51
Table 3.22	Percent Contribution of Factors to Machining Yield Considering Only Trials With the Rubber Regulating Wheel.....	53
Table 3.23	Chemical Analysis of Six Compositions Following Pre-nitriding and Nitriding .....	57
Table 3.24	Intergranular Phase Identification.....	61
Table 3.25	Physical and Mechanical Properties of Sinter-HIPed $\text{Si}_3\text{N}_4$ Using Cercom Standard Cycle .....	63
Table 3.26	Factors and Levels for the Sintering DOE.....	65
Table 3.27	Taguchi Array for the Sintering DOE .....	65
Table 3.28	Results of the Sintering DOE.....	66
Table 3.29	Theoretical Densities of Program Materials Derived Empirically ..	72
Table 3.30	Densities Resulting from First HIP Cycle.....	73
Table 3.31	EDX Analysis for the Two-Toned Cross-Section.....	78
Table 3.32	Physical and Mechanical Properties for Sinter-DOE After HIPing.....	85
Table 3.33	X-ray Diffraction and Chemical Analysis Results for First Set of HIPed Materials.....	86
Table 3.34	DOE HIP.....	88
Table 3.35	Quantitative Analysis of the Fibrous Residues in HIPing .....	92
Table 3.36	Density, Hardness and Toughness of HIPed $\text{Si}_3\text{N}_4$ from Two Different HIP Runs .....	95
Table 3.37	Near-Surface Microporosity for HIPed $\text{Si}_3\text{N}_4$ (0.50 inch Diameter Balls) with Constant Conditions of 1825°C and 5,000 psi, but Varying Compositions and Equipment (Gorham, ABB) ...	98
Table 3.38	Microstructure Assessment of HIPed $\text{Si}_3\text{N}_4$ , (away from near-surface porosity zone).....	99
Table 3.39	Hardness and Toughness of HIPed $\text{Si}_3\text{N}_4$ .....	103
Table 3.40	Chemical Analysis of Materials Following Each Processing Step.....	104



Table 3.41	Intergranular Phase Identification .....	106
Table 3.42	Phase Distributions in $\text{Si}_3\text{N}_4$ After Various Processing Steps .....	107
Table 3.43	Second DOE for HIP Parameters .....	109
Table 3.44	HIPed Density from Taguchi Experimental Array .....	110
Table 3.45	Microporosity in HIPed $\text{Si}_3\text{N}_4$ from Experiment Array .....	111
Table 3.46	Vickers Hardness of HIPed $\text{Si}_3\text{N}_4$ from 2nd HIP Taguchi Array (units in $\text{kg/mm}^2$ ) .....	112
Table 3.47	Toughness of HIPed $\text{Si}_3\text{N}_4$ from 2nd Taguchi Array (units in $\text{MPa}\cdot\text{m}^{1/2}$ ) .....	113
Table 3.48	ANOVA Results: Percent Contribution on Hardness and Toughness .....	113
Table 4.1	Results of Flexural Strength Testing on Deliverable Material .....	118
Table 4.2	Microstructure Assessment; Hardness and Toughness of Deliverable 4/4/1/3 HIPed $\text{Si}_3\text{N}_4$ .....	120
Table 4.3	Dimensional Requirements for As-Fired Ball Blanks .....	122
Table 4.4	Dimensional Inspection of Deliverable Ball Blanks .....	122
Table 4.5	Ceramic Bearing Blank Dimensions and Densities at Four Processing Points .....	125
Table 5.1	Powders Selected for Use in Program .....	136
Table 5.2	Results of Mechanical Testing on Deliverable Material .....	141
Table A.1	Atomic Number and Back-Scatter Coefficient, $\eta$ , of Elements in Powder Blends .....	144
Table B.1	Microstructural Assessment: Determination of the Presence, Level and Distribution of Porosity, Metallic Phases, Ceramic Second Phase and Inclusions .....	152
Table B.2	Maximum Limits for Microstructural Features of Each Material Class .....	153
Table B.3	Maximum Number of Inclusions per $\text{cm}^2$ of Cross-Section .....	154

## FOREWORD

This document is an interim report covering work performed under U.S. Air Force Systems Command Contract No. F33615-92-C-5903. The Air Force Contracting Officer was Frederick D. Rueth. The Air Force Project Engineer was Karl R. Mecklenburg of Wright Laboratory/MLBT (513) 255-2465. This project was sponsored by:

Materials Directorate

Wright Laboratory

Air Force Systems Command (ASD)

United States Air Force

Wright Patterson AFB, OH 45433-6533

The Advanced Research Projects Agency, (ARPA) in Arlington, Virginia, was the original source of the funding. The project was based on a Cercom proposal submitted in response to ARPA Broad Agency Announcement (BAA) 91-11-DARPA.

## INTRODUCTION

The current state of rolling element bearing technology has increasingly become a constraining factor in the design of next-generation gas turbine engines and other very high speed, high precision rotating machinery. The potential of ceramic materials to provide major advancements in this technology has been postulated for decades, but no ceramic bearings have yet been developed that demonstrate sufficient performance benefits and reliability to use in critical applications such as aircraft engines.

One example of the limitation of current bearing technology is in turbine engines for aircraft propulsion and for power generation. An important economic factor in turbine engine design is time between overhauls (TBO). This time interval is largely determined by the life of the mainshaft support bearing system. In order to extend the life of these bearings, engine designers have reduced the shaft speeds below the levels which would result in optimum fuel efficiency. If reliable bearings with longer service lifetimes became available, immediate gains in engine efficiencies could be realized. Ceramic balls and rolling elements have been demonstrated to provide longer life than conventional steel elements in high-speed bearing applications, largely due to their superior resistance to fatigue and wear. They also cause less wear to the outer bearing race surface because their lighter weight produces lower centrifugal forces, which can be quite appreciable at high speeds.

Of all the types of ceramics used in engineering applications, silicon nitride appears to be the best suited to bearing applications because of its high strength, hardness and relatively high toughness. One important advantage that silicon nitride has over steels is its increased hardness. A typical hardness value for silicon nitride is 1400 kg/mm<sup>2</sup>, compared to 800 kg/mm<sup>2</sup> for M-50 case-hardened steel. The increased hardness of the ceramic results in dramatically lower wear rates and fatigue sensitivity. Another major advantage of silicon nitride is its lower density compared to steel. This means reduced weight, which, at very high rotational speeds, translates into dramatically lower centrifugal forces between the rolling elements and the outer bearing race. A third advantage of silicon nitride is its elevated temperature capability. Silicon nitride retains useable strength and hardness to at least 1100°C (2010°F), whereas M-50 steel begins to soften at 325°C (620°F). Many advanced engine designs now being proposed have high operating temperatures which would exceed the limitations of current steel bearings. Such high temperature designs would, of course, also require advanced solid lubricants in addition to ceramic bearing technology. A fourth advantage of silicon nitride is its higher modulus of elasticity. This leads to a stiffer bearing that allows less vibration of the rotating shaft, an important consideration in high-speed applications. The advantages that silicon nitride material brings to bearings is summarized in Table 1.1.

**Table 1.1 – Potential Benefits of Ceramics in Bearings  
(from Katz and Hannoosh<sup>1</sup>)**

Demonstrated Bearing Performance Improvements	Enhanced Systems Performance
Increased Life	Reduced Specific Fuel Consumption (SFC)
Increased Speed	Increased Time Between Overhauls (TBO)
Reduced Heat Generation	Increased Power Density
Increased Stiffness	Lower Vibration
Lubrication Starvation Tolerance	
Increased Operating Temperature Limit	
Increased Corrosion Resistance	
Lower Susceptibility to Abrasion from Foreign Particles	
Brinelling Resistance	

Some potential applications for ceramic bearings are listed in Table 1.2 according to the type of lubrication and the operating speeds required.

The concept of ceramic bearings is not new; in fact, sophisticated testing and evaluation programs of silicon nitride ball bearing assemblies have been conducted sporadically since the early 1970s. Beginning in 1972, the Naval Air Systems Command funded two programs to investigate the use of silicon nitride rolling elements and races. One program was at Norton<sup>2</sup>, and the other at SKF<sup>3</sup>. In the Norton program, silicon nitride rollers and races were fabricated and tested at 10,000 rpm and 2500 lb. load for up to 600 hours. The testing indicated that the silicon nitride has better fatigue resistance than steel, and was well suited for use in bearing applications. The work carried out at SKF encompassed an evaluation of the lubrication elastohydrodynamics of silicon nitride. This work showed that wetting angles

with oil were similar to the ones for steels and that silicon nitride bearings would be compatible in all respects with normal lubricant oils.

**Table 1.2 – Ceramic Bearing Applications**

Category	Application
Marginally Lubricated Systems	Machine tool spindle bearings Fuel-lubricated turbine engine bearings Fuel pumps Fuel hydraulic systems Fuel controls Pump motors & generators for naval auxiliary systems Gyroscopes Turbopumps Computer Disc Drives
High-Speed Liquid Lubricated Systems	High-speed spindle bearings Turbine engine mainshaft bearings
Low-Speed Solid-Lubricated Systems	Turbine engine auxiliaries Air motors Nozzle actuators Space gimbals X-ray tube rotating cathode Electric motors operating in vacuum
High-Speed Solid-Lubricated Systems	Future high-efficiency gas turbine engine mainshaft bearings

Another such early program was carried out by Teledyne CAE Company, in which all-ceramic roller bearing assemblies substituted for steel ones in the Harpoon missile engine<sup>4</sup>. This particular program failed because of ceramic race fractures arising from problems in mounting. Sundstrand conducted a series of ceramic bearing tests between 1976 and 1982 using both hybrid bearings and all-ceramic bearings in a highly instrumented 10 kW turbogenerator<sup>5</sup>. (A hybrid bearing consists of silicon nitride balls or rolling elements in conventional steel inner and outer races.) Almost 4500 hours (181 days) of endurance testing were carried out on the hybrid bearings at speeds up to 110,000 rpm during this program. Some of the conclusions drawn from this testing were<sup>6</sup>:

1. "The fatigue life of the hybrid bearing was computed to be about five times that of its all-M-50 steel counterpart"
2. "High-speed ceramic-element bearings apparently fail much less rapidly than their all-steel counterparts, facilitating detection in time to avert extensive secondary damage."
3. "Ceramic element bearings apparently are more tolerant of ball roundness and size matching deviations than their all-steel counterparts, possibly because of the significantly reduced inertia of the ceramic balls compared to the steel ones."

Many of the world's major precision bearing manufacturers now offer hybrid bearings. None of the manufactured materials used in these finished rolling elements, however, yet meets the quality and reliability criteria needed for man-rated applications. Since the cost of these ceramic bearings is more than ten times higher than comparable steel balls, their performance must be exceptionally good to justify their use in economic terms. To-date, there have been few applications that passed the litmus test of economics. Before widespread use of ceramic bearings can occur, either the performance must be significantly improved, or the cost must be lowered. The performance of existing ceramic bearing materials already surpasses more conventional materials, but laboratory-scale demonstrations of silicon nitride materials have shown that the potential exists for significant further advances. Cost reductions are potentially achievable through the development of more efficient manufacturing methods. Improved knowledge of material formulations and materials processing methods is required to establish a stable domestic capacity for manufacturing premium quality silicon nitride blank material for rolling element manufacture.

The objective of the program described in this report was to optimize the materials processing parameters used in silicon nitride rolling element fabrication to develop a process for producing materials of better quality than any others now available in the United States. Ball and roller bearing

element blanks were fabricated in this program and delivered to the government for further evaluation.

Sintered, reaction-bonded silicon nitride (SRBSN) process technology has been used over the past three decades in the manufacture of silicon nitride materials for advanced engineering applications. This technology begins with a "green body" composed of elemental silicon powder plus sintering aids that have been consolidated into a coherent shape by cold isostatic pressing or simple cold compaction. The green body is reacted with nitrogen by placing it in a nitrogen atmosphere furnace and slowly ramping it over a temperature range from 1100°C to 1350°C over a period of several days. Nitrogen diffuses into the part and reacts with the silicon to form silicon nitride. This reaction produces no volume change in the part but causes a weight gain of approximately 60%. The reaction-bonded part does not reach full density during this process, so a densifying step is performed thereafter. Either sintering, hot-pressing, HIPing, or a combination thereof, may be performed to fully densify the part. Hot-pressing and HIPing both tend to produce materials with better mechanical properties than sintering, but sintering is less expensive. Hot-pressing is only capable of producing simple shapes and may tend to produce anisotropic mechanical properties. HIPing works with any part geometry and yields isotropic properties but is the most expensive of the three methods.

Liquid-phase sintering aids, normally a combination of metal oxides, are added to the silicon powder to promote the attainment of full density in the final product. A mixture of yttria ( $Y_2O_3$ ) and alumina ( $Al_2O_3$ ) is often used for this purpose. A secondary benefit of this liquid phase is that it promotes the formation of  $\beta$ -phase silicon nitride from the  $\alpha$  phase which first forms during nitriding.  $\beta$ - $Si_3N_4$  grains are often acicular (needle-shaped), and this morphology is associated with significantly increased fracture toughness.



The exact chemical composition of the liquid phase sintering agent is a strong determinant of the mechanical and physical properties of the final product. On cooling, this liquid may solidify to form either a crystalline or an amorphous intergranular phase, or both, depending on its composition and thermal history. This phase is a continuous one, so each grain of  $\text{Si}_3\text{N}_4$  is completely surrounded by the intergranular phase. Mechanical strength is therefore largely attributable to the interfacial adhesion between the two materials and the cohesion within the intergranular phase. In general, a glassy phase leads to superior room temperature mechanical properties, while a crystalline phase results in better high temperature properties, especially resistance to creep. The starting composition of the powder blend used to produce the material is an extremely important factor in determining the strength, hardness, and toughness of the finished product. The formulation of the additives is, therefore, probably the single most important aspect of designing an optimized material.

As described above, there are four basic processes involved in the fabrication of RBSN materials:

1. Powder Blending
2. Powder Compaction
3. Nitriding
4. Densification.

Additional steps may be inserted for shape forming, but those listed above are the primary determinants of the microstructure and mechanical properties of the finished material.

The particular approach used in the present program takes advantage of the ability to form  $\text{Si}_3\text{N}_4$ -TiN particulate composites using sintered reaction-bonded silicon nitride (SRBSN) processing technologies. Foreign suppliers

have demonstrated that silicon nitride-based materials with particulate additions of TaN or TiN perform exceptionally well as rolling elements in bearing applications. The exceptional performance not only includes long life during field testing, but also includes excellent lot-to-lot consistency.

These foreign materials are fabricated using mixtures of  $\text{Si}_3\text{N}_4$ ,  $\text{Y}_2\text{O}_3$ ,  $\text{Al}_2\text{O}_3$  and TiN or TaN powders. The starting materials for our program are Si,  $\text{Y}_2\text{O}_3$ ,  $\text{Al}_2\text{O}_3$ , AlN, and  $\text{TiO}_2$ . Titania ( $\text{TiO}_2$ ) is transformed *in situ* to TiN during the RBSN process. This unique approach of introducing TiN into  $\text{Si}_3\text{N}_4$  through the use of  $\text{TiO}_2$  precursors produces a beneficial transient modification of the liquid intergranular phase and alters the glass transition and phase equilibria in the solidifying product. It will be shown later how the titania also produces beneficial modification of  $\text{Si}_3\text{N}_4$  grain morphology.

In addition to the program objectives already stated, some ancillary objectives relating to process optimization have also been addressed, including:

- a) impart handleability to isopressed blanks through the use of prenitriding in lieu of traditional binder/plasticizer additions;
- b) demonstrate green machining as a high-rate, low-cost production technique;
- c) show the feasibility of thermal processing by using pressureless sintering, and;
- d) demonstrate that  $\text{Si}_3\text{N}_4$  can be HIPed without the use of canning materials.

The hardware deliverables in this program were 1.27 cm ( $\frac{1}{2}$  in.) diameter balls and 1.27 cm ( $\frac{1}{2}$  in.) diameter, 15.2 cm (6 in.) long rods made from a down-selected  $\text{Si}_3\text{N}_4$  material. Both the balls and the rods were machined on a centerless grinder from prenitrided rods. The prenitriding process involves

the interruption of the full nitriding cycle after just enough reaction bonding has occurred for the material to possess sufficient cohesive strength to withstand the grinding process. After grinding is completed, the parts are returned to the nitriding furnace and reacted to completion. Compared to more conventional ceramic processing where fugitive binders would be used to produce green strength, this method avoids the contamination of binder residue. It also permits greater control over the strength of the part to be ground, so that the grinding process can be made more efficient. If the strength is too low, then a high breakage rate may occur in the grinder, whereas if the part is too strong, the grinding time becomes unnecessarily long.

Another innovation in process methodology adopted in this program is the use of hot isostatic pressing without reliance on glass envelopes. The usual practice employed in the HIPing of ceramic materials is to encapsulate the articles to be HIPed in glass. This glass softens at the processing temperature to permit the transmission of isostatic pressure while blocking the passage of gas into the residual porosity within the part. The fabrication and later removal of this glass envelope is an expensive and technically difficult additional processing step which we hoped to circumvent. Our successful efforts in this area will be described later in this report.

In the chapters of this report which follow, an 18 month program will be described that sought to develop a manufacturing process and a material composition capable of yielding premium quality silicon nitride bearing balls and rolling elements. The program culminated in the production and delivery of 50 rolling contact fatigue specimens and 50 bearing ball blanks to the Government. An add-on segment to this program will continue through July of 1994, in which material composition will be optimized beyond the state achieved in the original program.



# EQUIPMENT AND PROCEDURES

The work performed in this program consisted of extensive experimental and analytical tasks to develop optimized process parameters for each of the unit processes which together constitute the manufacturing process for the bearing element blank materials. The word "blank" is used because Cercom did not perform the final machining and finishing operations, necessary to create useable bearing elements. The end product of this work is in a form which the bearing manufacturer could use to fabricate the components. The constituent unit processes are:

1. Powder Blending
2. Cold Isostatic Pressing
3. Pre-nitriding
4. Green Machining
5. Nitriding
6. Sintering
7. Hot Isostatic Pressing (HIP)

Each of these processes was studied as a separate task within the program. The first program task was to choose a material composition and to select and characterize the raw materials to be used in the process. All subsequent program tasks were based on each of the seven unit processes listed above. The methods of Statistical Design of Experiments (DOE) were used to make the most efficient use of our research resources. DOE

methods were employed in the layout of test matrices and in the statistical analysis of results.

## **2.1 Powder Blending**

Powder blending and comminution are carried out by ball-milling. Weighed portions of ceramic powders and a liquid vehicle are added to a neoprene-lined steel jar, typically of 8.7 liter (2.3 gallon) capacity. Silicon nitride balls are also added to the jar to fill about 40% of its volume. The powder slurry / grinding medium mixture is sealed into the jar, and the jar is rolled on its side for a period of time, typically 1 to 3 days. Early in the milling process, the viscosity of the slurry may be measured by interrupting the rolling and immersing the probe of a Brookfield viscometer into the jar. If the viscosity is outside the range of 300 to 500 centipoise, then more liquid or powder may be added to bring the viscosity within this range, which is most conducive to efficient milling.

At the completion of ball-milling, the slurry is poured into a pan and placed in an oven to drive off the liquid. A common addition to this process is to filter the slurry before it flows into the pan to remove any particles larger than 40  $\mu\text{m}$  or any agglomerates which were not broken up and dispersed during ball milling. When the liquid has all evaporated, the powder is left in the form of a cracked cake. The cake is placed into a dry milling jar with balls and milled for 1 or 2 hours to break up the cake. The resulting powder is sifted through 5 and 30 mesh sieves and collected in a plastic bag.

## **2.2 Cold Isostatic Pressing**

The blended powders are formed into a solid compact or "*green body*" by cold isostatic pressing or "*isopressing*". In this process, the powder is poured into a shaped rubber bag, which is sealed, immersed in water, and subjected

to hydraulic pressurization for 30 seconds. The resulting part possesses sufficient strength to be handled without breaking, and the shape established by isopressing will be retained through the nitride process.

The isostatic press used in this work was manufactured by Autoclave Engineering, Inc. It has a 30.5 cm (12 in.) diameter by 91.4 cm (36 in.) deep working chamber. Its maximum pressure capacity is 207 MPa (30,000 psi). The device is shown on the right side of the photograph in Figure 2.1.



**Figure 2.1** *On the right half of the photograph, a technician is shown lowering a basket containing a part into the cold isostatic press.*

### **2.3 Centerless Grinding**

A centerless grinder is used to grind the green-formed and prenitrided rods to a uniform diameter. The term "centerless" refers to the fact that this type of grinder does not require the axis of the rod to be carefully centered in the machine, as in a lathe. The rod is laid between two rotating cylinders,

one cylinder does the grinding, while the other keeps the part counter-rotating against the grinding wheel. This centerless grinder design is also capable of cutting a rod into a set of spheres, using a specially shaped grinding wheel.

Cercom uses a centerless grinder manufactured by the Glebar Company. This grinder can be adapted to mass production with special automatic feed attachments, making it capable of producing up to 1400 balls per hour. A photograph of the Glebar grinder is shown in Figure 2.2, and a photograph of the special ball-grinding wheel is shown in Figure 2.3.

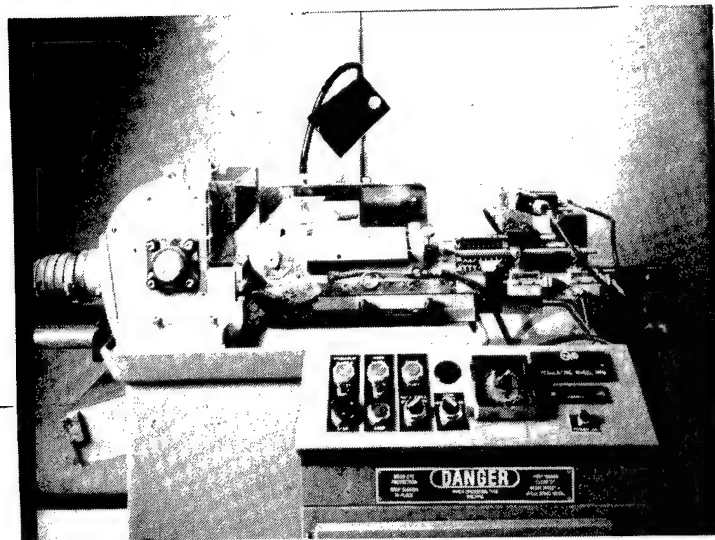


**Figure 2.2** *The Glebar centerless grinder used by Cercom to grind rods and balls*



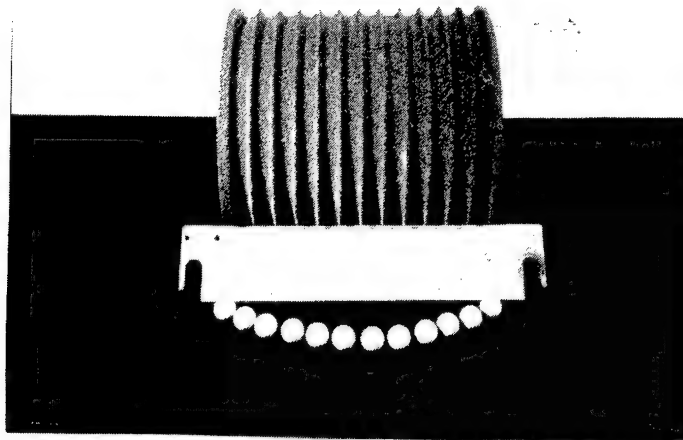


**Figure 2.3** *The special grinding wheel used in the centerless grinder for producing balls from rods.*

## **2.4 Prenitriding and Nitride Reaction Bonding**

Prenitriding and nitriding involve exactly the same process. The only difference between the two is that in prenitriding, the process is interrupted after a few hours, so only a fraction of the silicon in the part is converted to silicon nitride. This partial nitriding is performed to give the green body sufficient strength to survive the centerless grinding operation. After grinding, the part is returned to the nitriding furnace, and the process is carried through to completion.

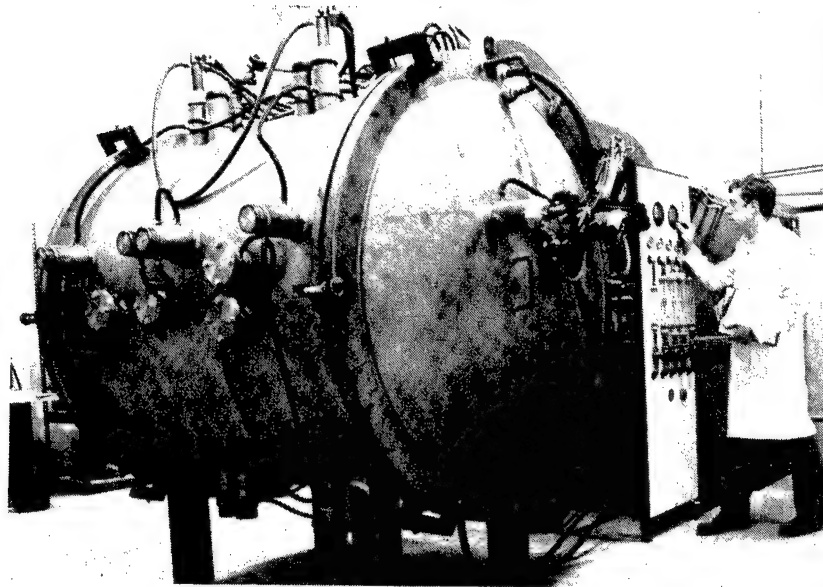
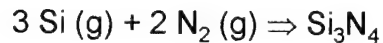
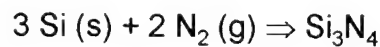


**Figure 2.4**    *The Cercom-designed cold-walled nitriding furnace.*

Nitriding is carried out in a cold-walled vacuum furnace shown in Figure 2.4. All interior materials of construction are selected for their overall inertness. Heating elements, hearth and heat shield are fabricated from molybdenum, and high-purity alumina is used for electrical insulation. The cold-compacted parts are placed in  $\text{Si}_3\text{N}_4$  containers with cover plates and are stacked within the furnace hot zone. The furnace vessel is evacuated to out-gas the green ware and construction materials. Gas back-filling is used to assist this procedure. Once the system integrity is confirmed by a leak check, the temperature is raised to  $600^\circ\text{C}$  ( $1112^\circ\text{F}$ ) and held until a vacuum of  $10^{-3}$  torr or lower is established. This procedure assists the outgassing process and removes all chemically-combined water and residual volatiles associated with the system. The furnace is then back-filled to a pressure of 20.0 kPa (2.9 psi) with a gas containing 3 percent  $\text{H}_2$ , 25 percent He, and 72 percent  $\text{N}_2$ . After the nitrogen from this mixture is consumed in nitriding, the

make-up gas is pure nitrogen instead of a mixture. A constant partial pressure of N<sub>2</sub> is maintained for the remainder of the cycle.

The conversion process takes place in the temperature range of 1100°C (2012°F) to 1400°C (2552°F) with two principle nitriding reactions:



Successful nitriding is achieved by precise control over the highly exothermic nature of these reactions. The kinetics at a given temperature produce an initial rapid nitriding rate which slows until an essentially complete reaction asymptote is reached (Arrhenius curve). The accepted technique for exotherm management is to proceed incrementally, beginning at 1100°C through the nitriding temperature range. At each temperature increment, the nitriding rate is allowed to reach its asymptote level before the temperature is again increased. The progress of the nitriding reaction is monitored by metering the quantity of nitrogen that flows into the furnace. The gas is delivered by a "demand system" that introduces a metered volume of gas, and then monitors furnace gas pressure. When this pressure drops below a specified level, another increment of gas is injected. The atmospheric control system keeps a count of the number of increments, and the time interval between increments. When the nitrogen demand drops below a predetermined rate, then the temperature is increased. Continuing this process to the maximum nitriding temperature of 1400°C will result in full conversion of the silicon to silicon nitride. The time required at a given temperature for the reaction rate to reach the asymptote level is dependent upon many variables. Some of the most critical variables are Si metal purity, surface area and particle size, compact green density and cross-sectional thickness. If management of the exotherm is not precise, the kinetics will cascade and the heat generated by the reaction will cause melting of the

silicon. Once melted, the silicon coalesces and cannot be nitrided. The duration of a complete nitriding cycle is approximately ten days, including initial outgassing, and post-nitride cool-down.

## **2.5 Sintering**

Sintering is conducted in a pressureless (ambient pressure) furnace specially-constructed by Cercom. This furnace uses graphite heating elements and graphite felt insulation within a steel vacuum chamber. The maximum part size it can accommodate is 50 cm (20 in.) in diameter and 76 cm (30 in.) high. The part is placed in the sintering furnace inside low-density silicon nitride retorts. The retorts serve to create a localized atmosphere that maintains a gas-phase equilibrium that prevents loss of SiO from the parts and associated silicon nitride decomposition. This controlled environment also keeps carbon species away from the part, preventing silicon carbide formation. In the sintering of silicon nitride parts, the furnace is pumped down to a vacuum, to less than 1 torr and then back-filled with an inert gas. A photograph of the sintering furnace is shown in Figure 2.5.

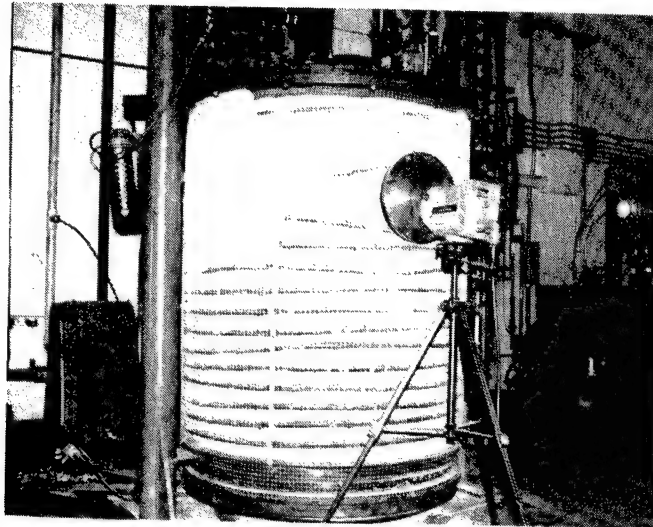


**Figure 2.5** Cercom's sintering furnace

## **2.6 Hot Isostatic Pressing (HIPing)**

The traditional Hot Isostatic Pressing or HIP processing of ceramic materials traditionally involves vacuum encapsulation of a part before subjecting it to high-pressure gas in a heated pressure vessel. The encapsulant or container is a temperature and pressure resistant material that serves as a pressure-transmitting membrane during processing. This process has been studied extensively and has been applied successfully to silicon nitride by a number of manufacturers. Theoretically dense isotropic bodies are produced with significant improvements in physical properties and overall material reliability (Weibull modulus  $> 12$ ). Furthermore, it has been shown recently using HIP techniques that silicon nitride can be densified to better than 95% of theoretical density using no sintering aids; a significant advance in  $\text{Si}_3\text{N}_4$  processing.

This traditional HIP process, although effective and quite versatile, is a high-cost process because of the expense involved with preparing and removing the container material. Additionally, the contact surface of processed components can show chemical variation to significant depths within the part due to reactions between the container and the part being HIPed. The outer layer of affected material must be removed by diamond grinding and, therefore, the process detracts considerably from the concept of "net shaping". Processing parts with sharp edges and corners represents a serious problem if the part must be encapsulated.

Cercom and others have developed an alternate HIP process technique known as "sinter-HIP", or sometimes referred to as "containerless HIPing" because of the positive economic gains that may be realized by eliminating the encapsulation process.

Sinter-HIP processing is generally accomplished by using two separate thermal treatments. The first includes pressureless sintering of an RBSN part to a closed porosity state. Closed porosity with a density greater than 90 percent of theoretical density is required so that the surface of the article can act as the pressure-transmitting membrane. The second treatment uses HIPing to remove all residual porosity from the sintered article to achieve theoretical density.

In theory, the sinter-HIP process should remove all residual porosity and produce a theoretically dense body. However, in practice, the application of this process to  $\text{Si}_3\text{N}_4$  is not straightforward and not yet well understood. Major open technical issues include: (a) influence of microstructural characteristics of the sintered material; (b) minimum density requirements of the sintered material; (c) solubility of Ar or  $\text{N}_2$  gas (used to supply pressure) into the silicon nitride intergranular phase.

Density increases have been observed only when the density of the sintered silicon nitride exceeds 93 percent of theoretical before HIPing. Data also show that the use of nitrogen, in contrast to argon, as the pressure medium leads to higher densities and strengths because decomposition of silicon nitride and certain intergranular phase compounds is suppressed. Literature on this issue is not clear but appears to support the Cercom observations that minimum density requirements will be material and microstructurally dependent.

The HIPing conducted in this program was done by two different toll HIPing services, Gorham, Inc. in Windham, Maine, and Asea Brown Boveri Autoclave (ABB) in Columbus, Ohio. The process parameters for HIPing were developed during the course of the program.

## 3.0

# EXPERIMENTAL RESULTS: MATERIALS AND PROCESS OPTIMIZATION

### 3.1 Selection and Characterization of Raw Materials

The first task of the program was to survey the available constituent powders and determine which were best suited for use as ingredients in a silicon nitride precursor powder blend. The selection criteria were powder purity, average particle size and size distribution, surface area, and cost. The powders being evaluated were silicon, yttrium oxide, aluminum oxide, aluminum nitride, and titanium oxide. Ceramic powder sources from all over the world were included in these evaluations. The methods listed in Table 3.1 were used to characterize the powders:



**Table 3.1 – Powder Characterization Methods**

Measured Characteristic	Method	Laboratory
Particle Size	Laser Scattering	Ricerca
Surface Area	BET	Ricerca
Chemical Composition	Inductively-Coupled Plasma Spectroscopy (ICP)	Dirats, Coors
Volatilization	Thermogravimetric Analysis (TGA)	Ricerca

Product data from all the known suppliers of each material were compared, and those which appeared to be most suitable were ordered. Samples from each shipment were sent to the analytical labs listed in Table 3.1 for objective comparisons. Particle size was usually the most important final selection criterion; the smallest particle size available almost always produces the best quality product. The final powder selections are as shown in Table 3.2.

**Table 3.2 – Powders Selected for Use in Program**

Material	Supplier	Grade
Silicon	Permascand	Sicomil
Aluminum Oxide	Ceralox	HPA-0.5 AF
Yttrium Oxide	Nippon Yttrium Corp. (NYC)	Ultrafine, 99.9% pure
Aluminum Nitride	Neomat	
Titanium Oxide	Fisher Scientific	T315-500 (Anatase)

The powder selections shown in Table 3.2 were not all actually downselected at the beginning of the program. Some of the final selections occurred later in the program based on ANOVA evaluations of Taguchi experimental matrices designed to study other process parameters, but in which multiple powder sources were used. In the case of yttria, the

availability of the Nippon Yttrium Corp. (NYC) product was unknown to us early in the program. The finest yttria found was a Molycorp 5600, which had an average particle size of 7 microns. A comminution process had to be developed to mill this powder to a smaller size so it could be blended effectively with the other constituents. The Neomat aluminum nitride, a material produced by a plasma process, was also not discovered until relatively late in the program. This material is, again, much finer than any other grades previously known to us.

## **3.2 Powder Blending**

### **3.2.1 Introduction**

The blending of constituent powders into a mixture that can be compacted and nitrided is a critical process in producing a material with homogeneous composition. Silicon, alumina, titania, and aluminum nitride powders must be so thoroughly intermingled that every single unit volume of powder has exactly the same proportions of constituents as every other unit volume. The diffusion distance over which compounds may be transported during sintering is too short to provide significant homogenization of the material, so any inhomogeneities that exist in the powder blend will be carried through to the finished product. Local deficiencies or agglomerations of one of the constituents can lead to inclusions and voids.

In addition to the possibility of incomplete mixing, the second danger in powder blending is that foreign material may be introduced into the mixture. The ceramic grinding media used in the jar-milling process will inevitably be abraded during the process, causing introduction of foreign material into the blend. This effect is controlled by careful selection of the grinding medium and by limiting the jar-milling time to the bare minimum required for homogenization.

The efficiency of the ball-milling (or jar-milling) process is dependent upon a number of technical details such as the viscosity of the powder/ liquid slurry, the filling fraction of media in the jar, and the filling fraction of powder in the jar. If these factors are not properly adjusted, then the milling time to achieve complete homogeneity will be too long, leading to excessive media attrition.

The final step in the blending process is drying and screening of the slurry. The Cercom process consists of pouring the milled slurry into pans and placing them in an oven to evaporate the liquid vehicle. When the drying is complete, the pans are removed from the oven and the caked powder is dry milled to break up the cake, and then sifted. The principal danger in the drying process is that some of the constituents will begin to settle to the bottom of the pan before enough liquid has evaporated to halt settling. The subsequent dry milling does not provide sufficient blending efficiency to reverse such separation, should it occur.

### **3.2.2 Yttria Comminution**

The first blending efforts were directed toward reducing the particle size of Molycorp 5600  $Y_2O_3$ . At the time, this was the finest yttria known to us, yet its average particle size of 7 microns made it too coarse to be properly blended with the silicon base powder. A comminution process was investigated consisting of the following steps: dispersing the powder into a slurry, ball-milling, filtering, drying, and screening.

The ratio of ball-milling media charge to material charge was varied to determine the optimum level for the Molycorp 5600  $Y_2O_3$ . For this experiment, three ratios were used: 40 v/o media / 20 v/o material; 40 v/o media / 40 v/o material; and 50 v/o media / 25 v/o material. After grinding, the powders were analyzed by SEM. Table 3.3 shows the effects of media/material ratios on particle size. The table lists the average particle

size as calculated by the intercept method for SEM, imaged at 5000X. The table also lists the number of particles  $\geq 2\mu\text{m}$  and  $\geq 5\mu\text{m}$  in diameter counted per SEM micrograph at the specified magnifications. As the media/material ratio was increased to 50% / 25%, the number of large particles and also the average particle size decreased. With this ratio, the particle size of the milled Molycorp 5600 yttria was finer than that of the 3 to 4  $\mu\text{m}$  silicon base powder into which it must be blended.

**Table 3.3 – Particle Size of 48-hour-Milled Molycorp 5600  $\text{Y}_2\text{O}_3$  as a Function of Media-to-Powder Ratio. (Columns 2 & 3 indicate the number of particles counted per SEM micrograph at the indicated magnifications.)**

% Media / % Material	1000X No. $\geq 2\mu\text{m}$	5000X No. $\geq 5\mu\text{m}$	Mean Size in $\mu\text{m}$
20/40	125	23	1.7
40/40	80	6	1.0
50/25	45	1	0.6

A filtering system was included in the yttria comminution process to remove any contaminants or large agglomerates that might act as defects in the final product. The filter system was set up using a peristaltic pump to push the slurries through a filter and into a drying container. With this system, we were able to filter using 70 and 100  $\mu\text{m}$  screens, but the 40  $\mu\text{m}$  screen clogged. It was imperative, however, that agglomerates greater than 40  $\mu\text{m}$  be removed to ensure homogeneity. To improve the filtering capability, the filter container was submerged in an ultrasonic bath. There was an immediate improvement, allowing filtration using a 40  $\mu\text{m}$  screen.

The filter cake, the residual material on the filter screen, was examined in the optical microscope. The cake had a high concentration of bright particles and agglomerates. These agglomerates were as large as 100  $\mu\text{m}$ . Examination by SEM/EDAX identified these particles and agglomerates as yttria.

### 3.2.3 Homogenization DOE No. 1

A Taguchi DOE was designed for investigating the blending process. The purpose of the DOE was to optimize homogeneity and deagglomeration of powder blends. Three factors were varied at two levels in the DOE. The two evaluated solvents were a grade of denatured alcohol designated CDA-19, and a 40/60 azeotropic mixture of the CDA-19 with MEK (methyl ethyl ketone) with an added dispersing agent. Two different grades of titania were used: Fisher anatase and ICD TOT-3 rutile. The two grades of yttria were comminuted Molycorp 5600 and Nippon Yttrium Corp. (NYC) 0.4 $\mu$ m yttria. Table 3.4 lists the factors and levels for the homogenization DOE. Table 3.5 lists the four sets of conditions dictated by the Taguchi DOE.

**Table 3.4 – Factors and Levels for the Homogenization DOE**

Factor	Level	
	1	2
1) Solvent/Dispersant	CDA-19	Azeotrope/Dispersant
2) Grade of TiO <sub>2</sub>	Rutile	Anatase
3) Grade of Y <sub>2</sub> O <sub>3</sub>	Comminuted Molycorp	0.4 $\mu$ m NYC

**Table 3.5 – Taguchi Array for the First Homogenization DOE**

Condition	Factor			White
	1	2	3	Area (%)
1	CDA-19	Comminuted Molycorp 5600	Rutile	4.4
2	CDA-19	NYC 0.4 $\mu$ m	Anatase	0.7
3	Azeo/Disper- sant	Comminuted Molycorp 5600	Anatase	3.5
4	Azeo/Disper- sant	NYC 0.4 $\mu$ m	Rutile	0.6

The powder composition was a 6/3/2 (%Y<sub>2</sub>O<sub>3</sub> /%Al<sub>2</sub>O<sub>3</sub> /%TiO<sub>2</sub>) composition milled in an 8.7 liter (2.3 gallon) steel neoprene-lined jar for 24 hours. The viscosity was held between 300 and 400 cp. After milling, the batches were oven-dried for 24 hours at 75°C, dry-milled in a 10 liter Nalgene jar with 25 cm (1 in.) Burundum rods for 30 minutes, and screened to minus 30 mesh. Samples were then isopressed at 103 MPa (15 ksi) in a cold isostatic press (CIP). The four samples were examined for homogeneity of Y<sub>2</sub>O<sub>3</sub> by back-scattered electron imaging (BSE). This technique shows atomic number contrast. Particles of high atomic number, such as Y<sub>2</sub>O<sub>3</sub>, larger than about 0.5  $\mu$ m appear as bright spots in the BSE image. The percentage of area of the image that was white is listed in Table 3.5. The bar graph, Figure 3.1, shows the average percentage of white area in the BSE images as a function of solvent, Y<sub>2</sub>O<sub>3</sub> grade, and TiO<sub>2</sub> grade. The analysis of variance (ANOVA) results are as follows: the Y<sub>2</sub>O<sub>3</sub> grade had a 95 percent contribution to the white percent; the factors of solvent, TiO<sub>2</sub> grade, and error had a pooled contribution of 5 percent.

The conclusion was that the only factor that significantly influenced the percent white area was the  $Y_2O_3$  grade. Earlier, SEM micrographs had shown that the comminuted Molycorp 5600 had a higher amount of particles larger than  $0.5\ \mu m$  than the NYC  $0.4\ \mu m$  grade. Likewise, it was observed in this study that isopressed rods with comminuted Molycorp 5600 had a higher amount of large  $Y_2O_3$  particles than isopressed rods with the NYC  $0.4\ \mu m$   $Y_2O_3$ .

The second analysis for the homogenization DOE was EDXS (energy-dispersive x-ray spectroscopic) mapping. EDXS maps of Ti and Al were made at 1000X. The Ti maps of the two samples with anatase appeared fairly uniform, indicating good homogeneity of the anatase. However, the Ti maps of the two samples with rutile showed many bright areas corresponding to areas of high Ti concentration. On the basis of these results, it was decided that only the Fisher anatase would be used for all future processing.

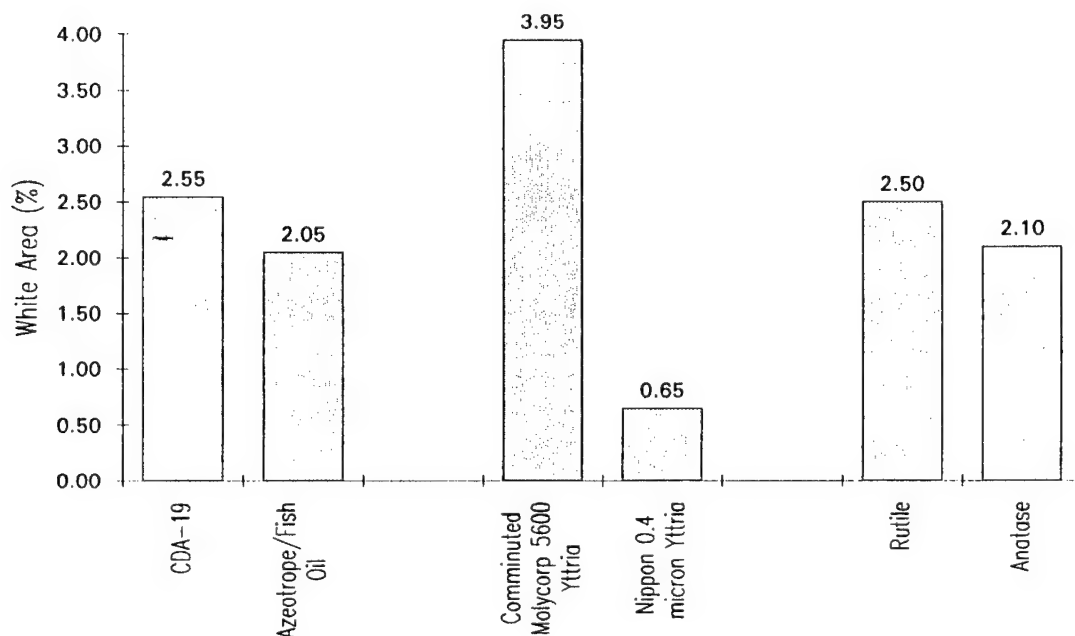


**Figure 3.1** Average percentage of white area in BSE images as a function of solvent,  $Y_2O_3$  grade, and titania grade.

The Al maps appeared fairly uniform for all four sets of conditions. Only about one or two bright areas were observed in each map at 1000X. This indicates that the homogeneity of the  $\text{Al}_2\text{O}_3$  was good for all four sets of conditions.

### 3.2.4 Homogenization DOE No. 2

A second Taguchi homogenization DOE was designed to determine the effects of filtering the slurry and also of using Molycorp 5600  $\text{Y}_2\text{O}_3$  from the improved comminution process. Table 3.6 lists the factors and levels for the second homogenization DOE. Table 3.7 lists the sets of conditions for the second homogenization DOE.

**Table 3.6 – Factors and Levels for the Second Homogenization DOE**

Factor	Level	
1) $\text{Y}_2\text{O}_3$	Molycorp 5600 (w/ improved comminution)	NYC 0.4 $\mu\text{m}$
2) Filter	40 $\mu\text{m}$	None
3) Solvent	CDA-19	Azeotrope / Dispersant

**Table 3.7 – Taguchi Array for the Second Homogenization DOE**

Condition	Factor		
	1	2	3
1	Molycorp 5600 Improved Comminution	40 $\mu\text{m}$	CDA-19
2	Molycorp 5600 Improved Comminution	None	Azeotrope / Dispersant
3	NYC 0.4 $\mu\text{m}$	40 $\mu\text{m}$	Azeotrope / Dispersant
4	NYC 0.4 $\mu\text{m}$	None	CDA-19



During milling of these materials, it was necessary to increase the solvent content by 30 percent to achieve the desired viscosity when the NYC 0.4  $\mu\text{m}$   $\text{Y}_2\text{O}_3$  was used. The need for additional solvent is the result of the high surface area of the powder. After filtering conditions 1 and 3, there were respectively 20.5 and 48.7 g of material that did not pass through the 40  $\mu\text{m}$  filter.

The experiment used a 6/3/2 composition milled in an 8.7 liter (2.3 gallon) steel Neoprene lined jar for 24 hours and a viscosity set between 300 and 400 cp. After milling, the batches were oven dried for 24 hours at 75°C(167°F), dry milled in a 10 liter (2.6 gallon) Nalgene jar with 2.54 cm (1 in.) Burundum rods for 30 minutes, and screened to minus 30 mesh. Samples were then isopressed at 103 MPa (15 kpsi) in a CIP. The four samples were examined for homogeneity of  $\text{Y}_2\text{O}_3$  by BSE. Particles of high atomic number, such as  $\text{Y}_2\text{O}_3$ , larger than about 0.5  $\mu\text{m}$ , appear as bright spots in the BSE image. The percentage of area of the image that was white is listed in the Table 3.8. The bar graph, Figure 3.2, shows the average percentage of white area in the BSE images as a function of  $\text{Y}_2\text{O}_3$  material, 40  $\mu\text{m}$  filter or no filter, and solvent.

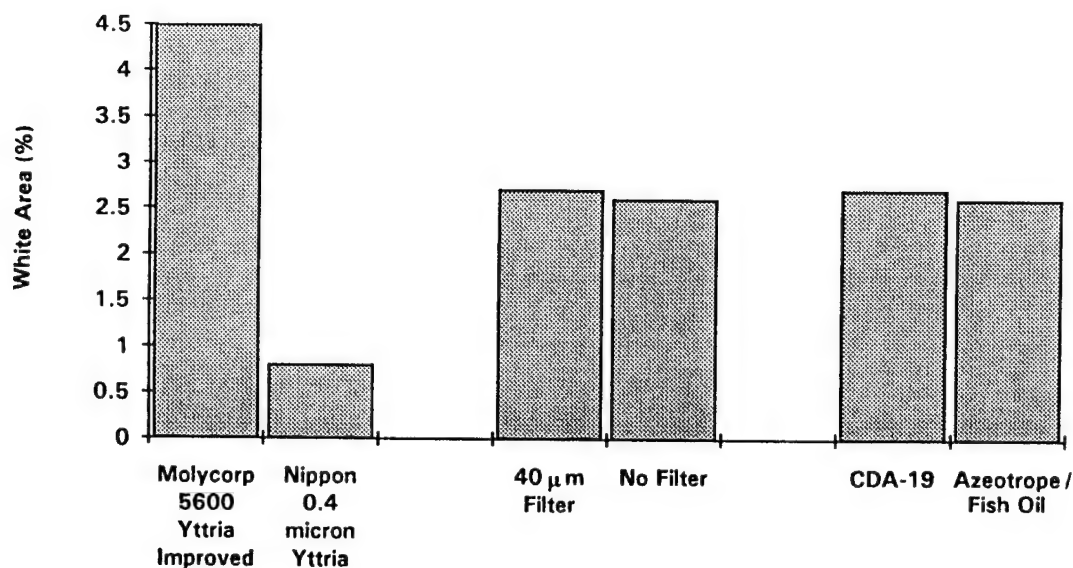


**Figure 3.2.** Average white area in BSE images as a function of  $Y_2O_3$  material, 40  $\mu$ m filter or no filter, and solvent for the 2nd Homogenization DOE.

The BSE imaging was also used to measure the concentration of  $Y_2O_3$  particles  $\geq 10 \mu$ m. In this method, 25 areas are scanned per sample at 200X magnification and the number of particles  $\geq 10 \mu$ m is counted. Then the surface concentration of particles is calculated.

The surface concentration of particles  $\geq 10 \mu$ m is listed in Table 3.8. The bar graph, Figure 3.3, shows the average surface concentration of  $Y_2O_3$  particles  $\geq 10 \mu$ m.

The large particles were examined at a magnification of 2000X. Samples with comminuted Molycorp 5600  $Y_2O_3$  had individually dispersed  $Y_2O_3$  particles or agglomerates of a few particles as large as 20  $\mu$ m. Samples with NYC 0.4  $\mu$ m  $Y_2O_3$  had agglomerates of submicron particles as large as 30  $\mu$ m.

**Table 3.8 – Taguchi Array for the 2nd Homogenization DOE. Also Listed Are the Results of the BSE Analyses in White Area and Surface Concentration of  $Y_2O_3$  Particles  $\geq 10 \mu m$ .**

Condition	Factor				
	1	2	3	White Area (%)	n (#/mm <sup>2</sup> )
1	Molycorp 5600 Improved Comminution	40 $\mu m$	CDA-19	4.6	3.3
2	Molycorp 5600 Improved Comminution	None	Azeotrope/dispersant	4.4	2.6
3	NYC 0.4 $\mu m$	40 $\mu m$	Azeotrope/dispersant	0.8	9.2
4	NYC 0.4 $\mu m$	None	CDA-19	0.8	10.8

The ANOVA results were as follows. The  $Y_2O_3$  material had a 97% contribution to the concentration of  $Y_2O_3$  particles  $\geq 10 \mu m$ . The factors of 40  $\mu m$  filter or no filter, solvent, and error had a pooled contribution of 3%.

The conclusion was that the only factor that significantly influenced the white area was the  $Y_2O_3$  grade. This is the same conclusion reported for the First Homogenization DOE, where the factors were  $Y_2O_3$  material, solvent, and  $TiO_2$  grade. The improved comminution process for Molycorp 5600  $Y_2O_3$  was used in the 2nd Homogenization DOE. However, the white area for samples with the more finely comminuted Molycorp 5600 did not decrease. In the First Homogenization DOE, the white area of samples with Molycorp 5600 was about 4%. This value remained unchanged with the more finely comminuted Molycorp 5600 of the 2nd Homogenization DOE. The surface concentration was about 3/mm<sup>2</sup> for samples with comminuted Molycorp 5600 and about 10/mm<sup>2</sup> for samples with NYC 0.4  $\mu m$   $Y_2O_3$ . The high

concentration of large  $\text{Y}_2\text{O}_3$  particles in samples with NYC 0.4  $\mu\text{m}$   $\text{Y}_2\text{O}_3$  was due to agglomeration.

Darnon and Drew have reported that the size of  $\text{Y}_2\text{O}_3$  agglomerates in  $\text{Si}_3\text{N}_4$  can be reduced by increasing mill time<sup>7</sup>. Because of its finer size, the NYC 0.4  $\mu\text{m}$  was down-selected as the  $\text{Y}_2\text{O}_3$  grade, and efforts were made to reduce the concentration of large agglomerates. The mill time was, therefore, investigated in the next DOE.

As for the issue of solvent selection, the ANOVA indicated no difference between the two systems tested. Independently of the DOE, however, it had been observed that the ethanol/MEK azeotropic mixture with added dispersant produced a slurry with lower viscosity than the CDA-19 (pure ethanol) alone. This was interpreted as an indication that the azeotropic mixture dispersed the powders better, and for this reason, the azeotrope was down-selected for use as the solvent.

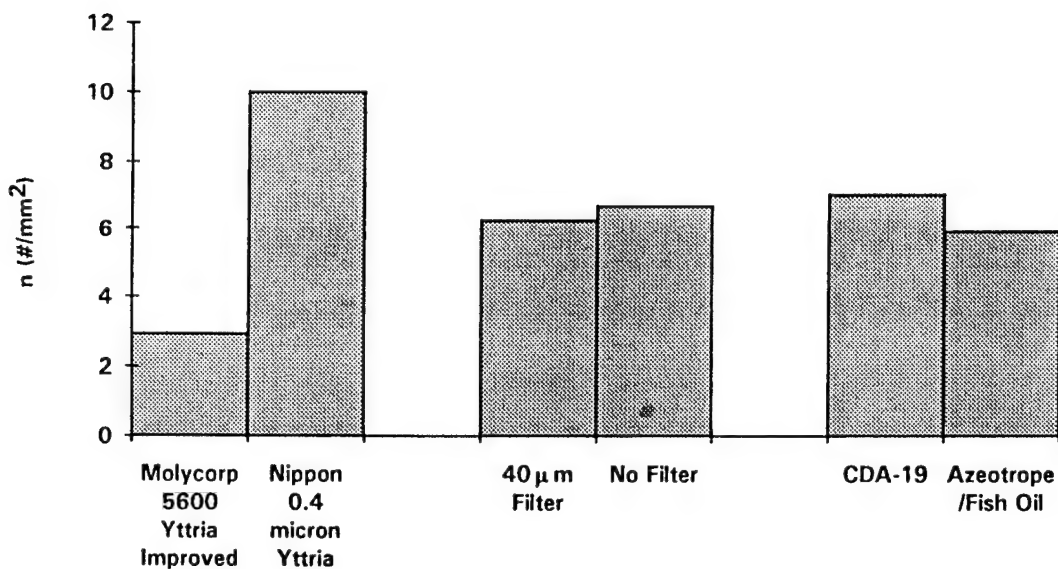


**Figure 3.3** Average surface concentration of  $Y_2O_3$  particles  $\geq 10 \mu m$  as a function of  $Y_2O_3$  material,  $40 \mu m$  filter or no filter, and solvent for the 2nd Homogenization DOE.

### 3.2.5 Ball-Milling Time

The final task in the effort to optimize homogenization parameters was to determine the length of ball-milling time necessary to homogenize the powder blend and break up the yttria agglomerates. Three 6/3/2 silicon nitride blends were milled in a 40/60 v/o azeotrope composition of denatured alcohol/methyl ethyl ketone (MEK) with 0.5 v/o dispersant. Times of 24, 48, and 72 hours were used for milling in a Neoprene-lined jar at a slurry viscosity between 300-400 centipoise. After milling, the slurries were pumped through a  $40 \mu m$  filter submerged in an ultrasonic bath. Once filtered the three batches were oven-dried for 24 hours at  $75^\circ C$ , dry milled and screened to minus 30 mesh. Samples were then cold isostatically pressed (CIP) at 103 MPa (15 ksi). Representative samples from each milling were examined for homogeneity of the NYC  $Y_2O_3$  by BSE using the QA technique that was developed.

The results of this study are tabulated in Table 3.9 and show that an increased milling time to 48 hours dramatically reduced the surface concentration of  $Y_2O_3$  agglomerates greater than 10  $\mu m$ . Additional milling times to 72 hours do not correspondingly reduce  $Y_2O_3$  agglomeration concentration. That is, milling times over 48 hours do not improve powder homogeneity. Therefore, the milling time for producing program-deliverable materials was selected to be 48 hours.

**Table 3.9 – Results of BSE Analysis of NYC  $Y_2O_3$  Agglomerates for Varying Milling Times on a 6/3 Silicon Metal Composition.**

Condition	Mill Time (Hrs.)	Surface Concentration of $\geq 10 \mu m$ $Y_2O_3$ #/mm <sup>2</sup>	Maximum measured Size of $Y_2O_3$ ( $\mu m$ )
1	24	10.0	14.2
2	48	0.2	10.7
3	72	0.2	10.7

### 3.3 Cold Isostatic Pressing

There were only two major issues to be addressed in this task, design and fabrication of a multiple-rod bag assembly, and selection of an optimum pressing pressure. Both rods and balls are the deliverable shapes in this program, and both shapes begin as the same diameter rods, which are ground later to final shape in a centerless grinder. The original rod shape is first produced when the blended powder is isostatically compressed within a rubber bag by external hydraulic pressure. For efficient manufacturing, it was necessary to design a rubber bag that could produce as many rods as possible in a single pressure cycle, given the size constraints of the Cercom cold isostatic press (isopress). The design used was a cow's udder type

configuration, having multiple closed-end rubber tubes descending from an upper filling bowl. A multiply-vented metal container fits around the outside of the tubes, keeping them straight during compression. A photograph of the isopress bag tooling assembly is shown in Figure 3.4.

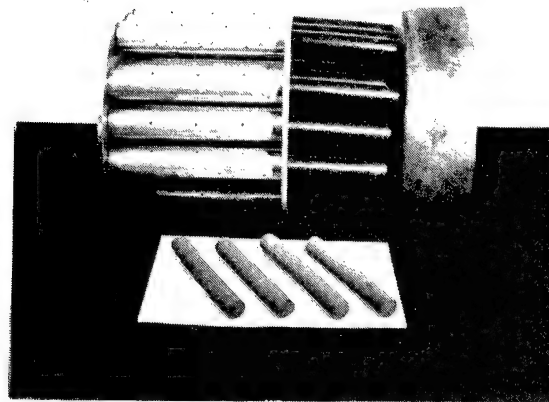


**Figure 3.4** *The multiple-rod isopress bag assembly.*

The second focus of the isopressing development task was to find the optimum pressure level for use with the newly-fabricated bag assembly. The pressure must produce a powder compact with a density of approximately  $1.5 \text{ g/cm}^3$ . If the green density were excessively low (i.e., high porosity), then detrimental shrinkage would occur during sintering. A target sintering shrinkage of 12 % is expected with SRBSN. Shrinkages larger than this might produce uncontrollable shape distortions. If the density of the green body is too high, then nitriding will not proceed to completion. A certain amount of porosity in the part is required to permit gaseous-state diffusion of nitrogen into the green body.

A series of isopressing experiments was conducted to determine the relationship between pressure and green density. The results of this effort are plotted in Figure 3.5. This figure shows that a pressure of 103 MPa (15 kpsi) leads to the target density of 1.5 g/cm<sup>3</sup>. The 103 MPa (15 kpsi) pressure was adopted as the standard isopressing pressure for this reason.

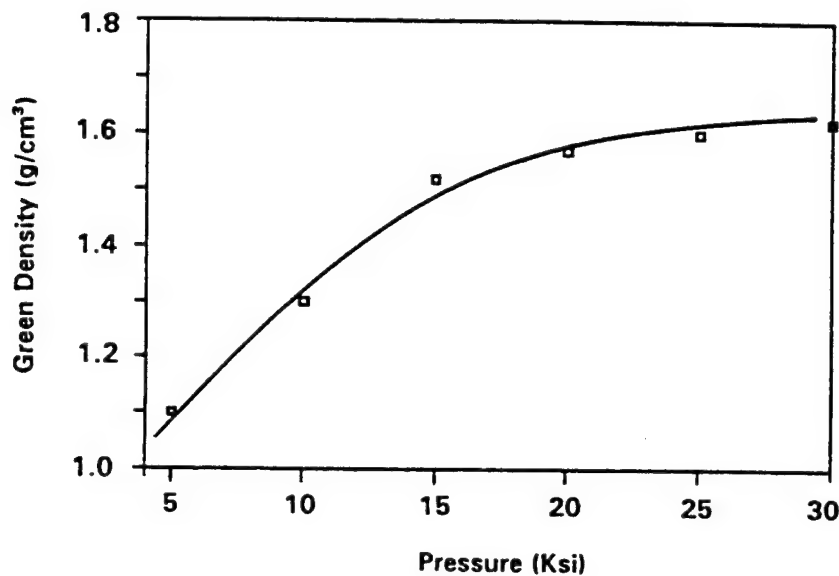


**Figure 3.5** *The measured relationship between isostatic pressing pressure and the resulting density of the silicon powder blend compact.*

### 3.4 Prenitriding

The objective of this task was to increase the strength of the isopressed rods so that they could be efficiently machined in a centerless grinder. The rods produced in the cold isostatic press are too weak to be ground. There are two thermal processes that can impart handling strength: prenitriding and argon sintering. Both processes can impart sufficient strength to the rods so they can be quickly and easily machined to size in a centerless grinder.



without chipping or breaking. A fully nitrided rod would be very difficult to grind in this manner because of its high strength and hardness.

Isopressed rods fabricated from four powder compositions were prenitrided using normal nitriding conditions, except that the nitriding times were limited to approximately 2, 4, and 6 hours. The prenitrided rods were evaluated by measuring the strength, density, open porosity and handleability in centerless grinding trials. The microstructures of the partially nitrided materials were characterized using optical and scanning electron microscopy.

Four 12.5 kg isopressed rod batches of different compositions were prenitrided/partially sintered. Each composition was separated into four equal parts and received four prenitride treatments, in accordance with the Machining-Yield DOE. This test matrix will be described in more detail in Section 3.5 – Green Machining. The total weight gain of each composition was recorded after prenitriding. The original DOE called for prenitriding at 1100°C (2012°F) for 4, 14, and 24 hours and sintering in inert gas at 1150°C (2100°F) for 3 hours. However, during the course of the experimentation, two of the prenitride/thermal bond levels required alteration from the original plan.

The weight gain was about 1.0 weight percent after 4 hr prenitriding for all four compositions. The weight gain was about 1.5 weight percent after 24 hr prenitriding for all four compositions. Because weight gain was so low after 24 hr prenitriding at 1100°C (2012°F), a new level of prenitriding was then substituted for the level originally planned to be 14 hr at 1100°C (2012°F). This new level was prenitriding at 1125°C (2060°F) for 20 hr, and 1150°C (2100°F) for 12 hr, for a total of 50 hr. This cycle yielded weight gains of about 2.5 weight percent for three compositions and about 8.4 percent for the 6/3/2 composition in the front-right quadrant of the furnace.

Partial sintering at 1150°C (2100°F) for 3 hours in argon yielded weight gains of about 1.8% for three compositions and 4.8% for the 6/3/2 composition in the front-right quadrant of the furnace. Table 3.10 lists the weight gains observed from the thermal treatments (in percent by weight).

**Table 3.10 – Weight Gain from Thermal Treatments (wt. %)**

Firing Schedule (hr/atmosphere)	Composition			
	6/3/2	8/2/2	8/1/2	5/2/3
3/ Ar	4.8	1.9	1.7	1.9
4/N <sub>2</sub>	1.0	1.0	1.0	1.0
24/N <sub>2</sub>	1.6	1.4	1.4	1.6
50/N <sub>2</sub>	8.4	2.8	2.7	2.4

The observed trends in weight gain are not all understood. Differences in weight gain were sometimes observed between lots at the same prenitride level. One possible cause for these differences is sensitivity of nitriding rate to sintering aid composition. Another possible cause is sensitivity of nitriding rate to temperature/location in furnace. An additional unexpected result was weight gain from partial sintering in inert gas. To help understand all these results, samples from prenitriding and partial sintering were chemically analyzed to determine nitrogen and oxygen contents.

The degree of nitriding for each composition/prenitriding cycle combination used in the subsequent Machining Yield DOE was quantified by induction coupled plasma spectrometry (ICP). These data provide an accurate relationship between measured weight gain and quantitative nitrogen pick-up. Oxygen content was also determined concurrently.

A nominal 5 gram disc was cut from each of 16 centerless ground rods. These samples were selected to represent combinations of four material

compositions and four prenitriding conditions. One of the conditions was an argon gas environment. The samples undergoing this cycle should not experience any weight gain by nitrogen/silicon reaction.

**Table 3.11 – Quantitative Oxygen and Nitrogen Analysis by ICP for Selected Centerless Ground Rods Used in Machining Yield DOE.**

Sample #	Composition	Thermal Bond Cycle	Measured Weight Gain (%)	Quantitative Nitrogen (%)	Quantitative Oxygen (%)
17	6/3/2	4	4.77	3.566	5.641
18	8/2/2	3	1.43	1.458	5.266
19	8/1/2	2	2.74	2.329	4.718
20	5/2/3	1	.97	.9831	4.355
21	8/2/2	4	1.94	1.853	4.985
22	6/3/2	3	1.57	1.503	5.136
23	5/2/3	2	2.44	2.228	4.964
24	8/1/2	1	1.00	1.004	4.212
25	8/1/2	3	1.36	1.487	4.524
26	5/2/3	4	1.89	1.894	4.782
27	6/3/2	1	.99	1.118	5.198
28	8/2/2	2	2.76	2.825	4.841
29	5/2/3	3	1.56	1.516	4.613
30	8/1/2	4	1.74	1.872	4.591
31	8/2/2	1	1.02	1.145	4.392
32	6/3/2	2	8.44	4.513	5.324

Each disc was powdered using a mortar and pestle and thereafter sealed in a sample vial. All samples were quantitatively analyzed for nitrogen and oxygen. These results are shown in Table 3.11.

Results show a very close correlation between the measured weight gains recorded for each of the four prenitriding/thermal bonding cycles and the quantitative chemical analysis. That is, the measured nitrogen weight gain was very comparable to the analyzed nitrogen content.

The analyzed nitrogen levels of the samples from the inert gas sintering (thermal bond cycle #4) indicate that nitrogen rather than inert gas was used as the process gas. This error invalidates the inert gas sintering portion of

the design matrix. The decision was made not to repeat this part of the experiment since the machining results on the prenitrided rods were very good.

Review of the oxygen analysis shows no correlation between the thermal bond cycle and quantitative oxygen content. The oxygen content appears to be entirely compositionally dependent as shown in Table 3.12. These data were used later to help determine compositions of intergranular phases that develop during nitriding.

Further work on prenitride cycle optimization was done in parallel with the green machining optimization and is, therefore, discussed in the next section.

**Table 3.12 – Oxygen Content as a Function of Composition for Rods Used in Machining Yield DOE.**

Composition	Avg. Oxygen (%)	Range in Oxygen (%)
6/3/2	5.325	5.136 to 5.641
8/2/2	4.871	4.392 to 5.266
8/1/2	4.511	4.212 to 4.718
5/2/3	4.678	4.392 to 4.964

### **3.5 Green Machining**

The objective of the green-machining development task was to learn how to machine prenitrided stock to size without failure. High-speed machining of the prenitrided stock was performed with a Glebar centerless grinder. This grinder could grind the rough rods to a uniform, fixed diameter, or grind spherical ball blanks from rough rod stock.

A DOE (design of experiments) was made for the prenitriding and machining tasks together using the Taguchi method. The Taguchi method

for DOE was chosen because these tasks contain a large number of factors. The Taguchi method keeps the number of tests at a manageable number while still determining the optimum conditions for processing, as well as the contribution of each of the factors. Also, the Taguchi method simplifies the DOE by providing standard arrays which dictate all tests, once the factors, number of levels, and value of each level are chosen.

Table 3.13 lists the factors and levels chosen for the DOE of the two processes, prenitriding and centerless grinding. There are 4 factors at 4 levels and 1 factor at 2 levels. The 4 compositions used are listed as a single factor, although it is actually 4 factors: wt. %  $Y_2O_3$ , wt. %  $Al_2O_3$ , wt. %  $TiO_2$ , and rutile/anatase. Thermal bonding is a factor for the prenitriding study (Section 3.4). The other 3 factors in the DOE are the green-machining factors. Since only 2 types of regulating wheels are available, this factor was limited to 2 levels. The other machining factors, RPM of regulating wheel and rate of grinding wheel feed, were each set at 4 levels. The quality characteristic for this DOE is the yield from machining.

**Table 3.13 – Factors Chosen for the DOE for Prenitriding and Green-Machining.**

Factor	No. of Levels	Levels			
		1	2	3	4
1) Wheel Type	2	Rubber	Alumina		
2) Wheel RPM	4	40	60	80	100
3) Feed Rate	4	0.1"/12s	0.1"/9s	0.1"/6s	0.1"/3s
4) Thermal Bonding	4	4 hr.	14 hr.	24 hr.	Sinter
5) Composition	4	6:3:2	8:2:2	8:1:2	5:2:3

The standard Taguchi array for this mixed level system is shown in Table 3.14. The Taguchi method dictates the 32 sets of conditions listed in the

array. The dictated levels of each factor are listed by number: 1 or 2 for wheel type; 1, 2, 3, or 4 for each of the other factors.

The silicon rods of each composition, pressed at 103 MPa (15 psi) and prenitrided, were centerless ground into straight rods and then centerless ground with a form wheel into balls under various conditions. During the machining, many rods broke into pieces. Also, as the individual balls began to separate, many of the elliptical blanks spun into the wheel and were shattered, chipped, or gouged. The simplest measure of machinability was machining yield, the survival rate of reasonably whole parts. All lots also had minor defects due to machining, but these were not measured quantitatively.

**Table 3.14 – Taguchi DOE Array for Prenitridding and Machining**

Set	Factor				
No.	1	2	3	4	5
1	1	1	1	1	1
2	1	1	2	2	2
3	1	1	3	3	3
4	1	1	4	4	4
5	1	2	1	1	2
6	1	2	2	2	1
7	1	2	3	3	4
8	1	2	4	4	3
9	1	3	1	2	3
10	1	3	2	1	4
11	1	3	3	4	1
12	1	3	4	3	2
13	1	4	1	2	4
14	1	4	2	1	3
15	1	4	3	4	2
16	1	4	4	3	1
17	2	1	1	4	1
18	2	1	2	3	2
19	2	1	3	2	3
20	2	1	4	1	4
21	2	2	1	4	2
22	2	2	2	3	1
23	2	2	3	2	4
24	2	2	4	1	3
25	2	3	1	3	3
26	2	3	2	4	4
27	2	3	3	1	1
28	2	3	4	2	2
29	2	4	1	3	4
30	2	4	2	4	3
31	2	4	3	1	2
32	2	4	4	2	1

Table 3.15 shows the sets of factors used in each of the 32 test conditions as well as the weight gain and yield which resulted from those conditions.

**Table 3.15 – Conditions for the Machining Yield  
Test Matrix and Corresponding Results**

Condition #	Factor					Results	
No.	1	2	3	4	5	Wt. Gain (%)	Yield (%)
1	1	1	1	1	1	.99	90.9
2	1	1	2	2	2	2.76	99.5
3	1	1	3	3	3	1.36	98.7
4	1	1	4	4	4	1.89	100
5	1	2	1	1	2	1.02	37.6
6	1	2	2	2	1	8.44	100
7	1	2	3	3	4	1.56	98.7
8	1	2	4	4	3	1.74	100
9	1	3	1	2	3	2.36	82.6
10	1	3	2	1	4	.97	78.2
11	1	3	3	4	1	4.77	96.7
12	1	3	4	3	2	1.43	65.3
13	1	4	1	2	4	2.44	82.0
14	1	4	2	1	3	1.00	34.8
15	1	4	3	4	2	1.94	92.2
16	1	4	4	3	1	1.57	86.2
17	2	1	1	4	1	4.77	14.8
18	2	1	2	3	2	1.43	0
19	2	1	3	2	3	2.74	.7
20	2	1	4	1	4	.97	0
21	2	2	1	4	2	1.94	0
22	2	2	2	3	1	1.57	0
23	2	2	3	2	4	2.44	1.7
24	2	2	4	1	3	1.00	0
25	2	3	1	3	3	1.36	0
26	2	3	2	4	4	1.89	0
27	2	3	3	1	1	.99	.7
28	2	3	4	2	2	2.56	3.6
29	2	4	1	3	4	1.56	1.3
30	2	4	2	4	3	1.34	3.5
31	2	4	3	1	2	1.02	3.5
32	2	4	4	2	1	8.44	36.6



From the results, the regulating wheel type was found to be the most important factor influencing machining yield. The data are tabulated below for each factor by averaging the yields for all tests of a given factor. The results are also broken down by regulating wheel type. Table 3.16 lists machining yield for the rubber and alumina regulating wheels. Table 3.17 lists machining yield as a function of regulating wheel type and regulating wheel speed. Table 3.18 lists machining yield as a function of regulating wheel type and regulating wheel feed rate. Table 3.19 lists the machining yield as a function of regulating wheel type and prenitriding cycle. Table 3.20 lists the machining yield as a function of regulating wheel type and composition.

**Table 3.16 – Machining Yield as a Function of Regulating Wheel Type**

Wheel Type	Yield (%)
Rubber	83.9
Alumina	4.2

**– Table 3.17 – Machining Yield as a Function of Regulating Wheel Type and Regulating Wheel Speed**

RPM	Average Yield (%)		
	Rubber	Alumina	Combined
40	97.3	3.9	50.6
60	84.1	0.5	42.3
80	80.7	1.8	41.2
100	73.8	11.2	42.5

**Table 3.18 – Machining Yield as a Function of Regulating Wheel Type and Regulating Wheel Feed Rate**

Feed Rate (in./min)	Average Yield (%)		
	Rubber	Alumina	Combined
0.50	73.3	4.0	38.7
0.67	78.1	1.8	40.0
1.00	96.6	1.7	49.2
2.00	87.9	9.15	48.5

**Table 3.19 – Machining Yield as a Function of Regulating Wheel Type and Prenitriding Cycle**

Prenitriding Cycle			Average Yield (%)		
Temperature	Time (Hr.)	Avg. Wt. Gain	Rubber	Alumina	Combined
2025	4	1.00%	60.4	1.1	30.7
2025	24	1.48%	87.2	0.3	43.8
2100	3	2.59%	97.2	4.6	50.9
2100	24	4.10%	91.0	21.4	56.2

**Table 3.20 – Machining Yield as a Function of Regulating Wheel Type and Composition**

Composition	Avg. Wt. Gain (%)	Average Yield (%)		
		Rubber	Alumina	Combined
6/3/2	3.94	88.8	1.3	45.0
8/1/2	1.79	73.7	1.8	37.7
8/2/2	1.71	79.0	1.1	40.0
5/2/3	1.72	89.7	0.8	45.3

The feed rate of the regulating wheel drives the part against the grinding wheel. The friction between the two wheels and the product maintains the rotation of the product. If the product is very soft (i.e., freely machined), and the speed is too slow, the product stops rotating for short periods of time,

causing a flat spot to form. When it catches and restarts its rotation, the flat place may cause pinching, resulting in a shattered part.

As expected, rods prenitrided with the larger weight gains had higher yields. If this trend continued, weight gains greater than those used in this study would lead to even better yields. However, rods with excessive weight gains take much longer to machine, and result in shorter grinding wheel life. For example, it was observed during the tests with 4.77 and 8.4 percent weight gain that the product could not be touched by hand because of the heat generated during grinding. Using rods with excessive weight gain might necessitate the use of a diamond wheel. Water cooling is not possible because it would be detrimental to the product. It is believed that on the basis of grinding other test materials at a 4 to 6 percent weight gain, that the ideal gain would be about 4.5 to 5 percent. A weight gain of 3.5 percent to 4.5 percent would also be satisfactory. With a lower weight gain, however, the feed rate would need to be faster than that used for the 5 percent material.

The data were next analyzed by ANOVA. Figure 3.6 shows average machining yield as a function of regulating wheel type, regulating wheel speed and feed rate, weight gain and composition. The percent contribution of each function is shown in Table 3.21. Regulating wheel type had a contribution close to 90%.

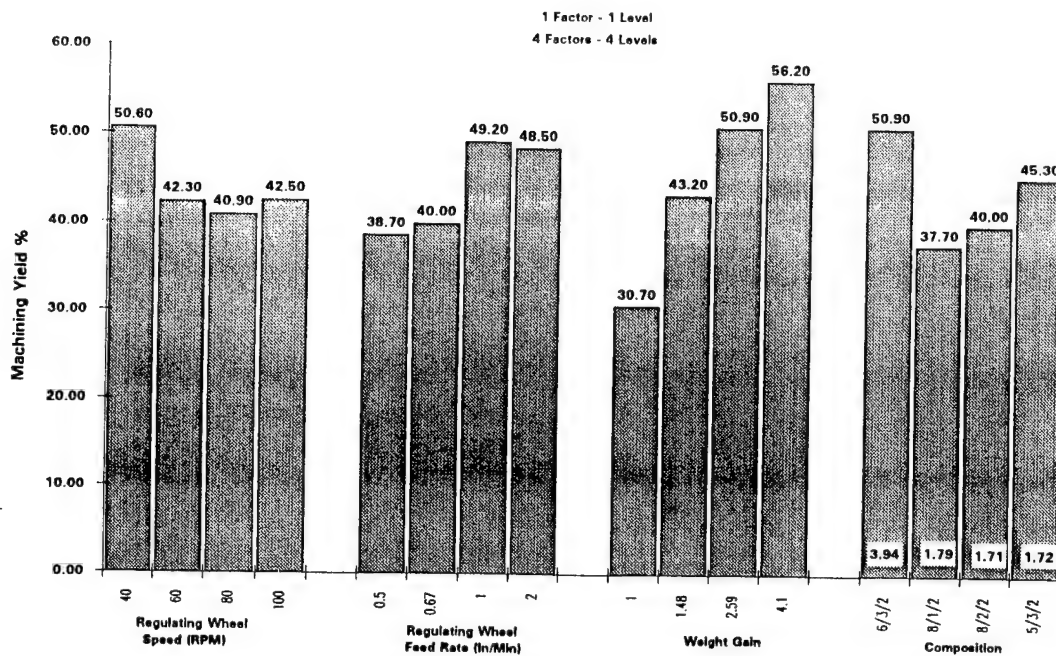


**Figure 3.6.** Average machining yield as a function of regulating wheel type, regulating wheel feed rate, weight gain, and composition.

**Table 3.21 – Percent Contribution of All Factors to Machining Yield.**

Factor	P (%)
Wheel Type	86.4
Wheel Speed	0.8
Feed Rate	1.4
Weight Gain	3.7
Composition	1.9
Error	5.8

The ANOVA considered only data from trials with the rubber regulating wheel type. Figure 3.7 shows average machining yield as a function of the remaining four factors of regulating wheel feed rate, weight gain, and composition. The optimum conditions, based solely on the ANOVA were wheel speed of 40 RPM, feed rate of 1.00 in./min., weight gain of 2.5%, and composition of 5/3/2. The percent contribution of each factor is shown in

Table 3.22. Weight gain was the most important factor with a contribution of close to 50%. Wheel speed, feed rate, and composition were all also important factors with contributions of close to 20%.

This ANOVA used only yield as the quality characteristic, and did not consider the issue of surface finish. Visual inspection of the parts showed that a wheel speed of 40 rpm produced a scalloped or faceted surface finish. A higher wheel speed of 60 rpm was, therefore, chosen for subsequent use in the program because it produced a smoother surface finish.

A summary of the results of the machining yield DOE is as follows: A rubber regulating wheel gives much better yield than an alumina regulating wheel. A regulating speed of 40 rpm produced the highest yields, but also produced a scalloped surface. Increasing the speed to 60 rpm reduced the yield but improved the surface finish. A feed rate of 1 to 2 inches per minute was better than 0.5 to 0.7 inches per minute in order to keep sufficient friction against the grinding wheel and maintain part rotation. There was also a direct relationship between yield and weight gain during prenitriding. The higher the weight gain, the higher the yield as well as heat generated during dry grinding. It was found that using a rubber regulating wheel at 60 rpm traveling at 1 to 2 inches per minute, dry grinding will produce satisfactory balls with prenitride weight gains of 3 to 6 percent. With lower weight gains, faster feed rates are needed and with higher weight gains, slower feeds are preferred.

**Table 3.22 – Percent Contribution of Factors to Machining Yield  
Considering Only Trials With the Rubber Regulating Wheel**

Factor	P (%)
Wheel Speed	17
Feed Rate	19
Weight Gain	48
Composition	15
Error	1

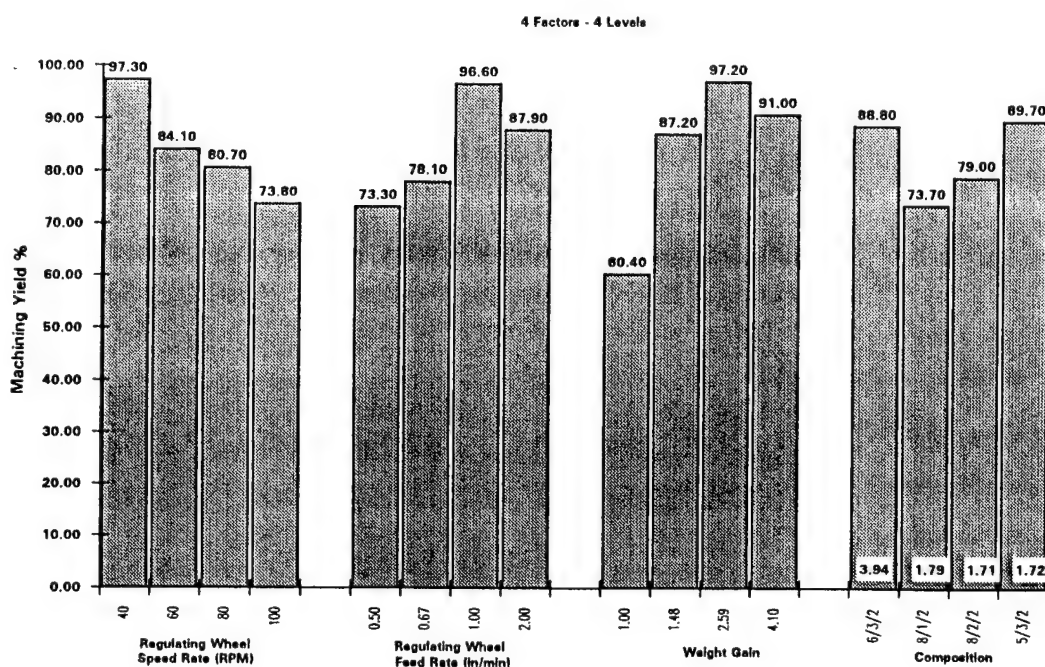


**Figure 3.7.** Average machining yield as a function of feed rate, weight gain, regulating wheel and composition. Only data from trials with the rubber regulating wheel were considered.

### 3.6 Nitriding

The goal of a properly optimized nitriding process is to convert all of the silicon in a part into silicon nitride. In theory, a silicon metal part would increase in weight by 66% in the process of being converted to silicon nitride. In practice, a weight gain of 60% can be realized in a pure silicon part,

because some of the nitriding occurs in the gas phase and forms silicon nitride that condenses away from the part. When SRBSN materials are nitrided, they contain additives such as yttria and alumina which do not take up nitrogen, so the weight gains for these materials are further reduced.

One potential difficulty in this process is the possible melting of silicon. The melting point of silicon is 1410°C (2570°F), while the upper end of the nitriding process range is 1400°C (2550°F). Since the nitriding reaction is extremely exothermic, it is very easy for the parts to overheat and experience melting of the silicon. When this occurs, the silicon coalesces into large, fully dense agglomerates that cannot be permeated by the nitrogen gas.

Iron is present in all silicon raw powder as a naturally-occurring trace impurity. It exists in the form of iron silicide. This iron has the beneficial effect of serving as a nitriding catalyst which accelerates the nitriding rate. If the iron content is excessive, or locally concentrated, however, the resulting large iron silicide particles can act as processing flaws and affect the final mechanical properties and reliability. Therefore, inspection of the nitrided parts is required to ensure that the silicide is small and well-dispersed.

A variety of methods was used to assess the success of the nitriding cycles used in this program. The first test is always a weight gain measurement. If the weight gain is less than predicted (including the gains that occurred during prenitriding), then either the nitriding did not go to completion, or there was excessive silicon sublimation. If the weight gain is near or equal to the calculated value, then it can generally be considered to be successful. The exact theoretical weight gain is determined by the composition. The  $\text{TiO}_2$  additive will pick up some additional nitrogen weight to form the  $\text{TiN}$ . Other additives keep the same weight and do not contribute to the weight gain. For this research program, evaluations were performed to provide a deeper understanding of the relationships in the nitriding process

between the input variables of powder blend composition and process conditions, and the response variables of microstructure and phase compositions.

Direct visual inspection of the nitrided parts was often sufficient to determine whether melting of silicon had occurred. This can sometimes be recognized from specular spots on the surface of the parts. Because a silicon melt will not wet silicon nitride, if the nitriding process overheats, the resulting silicon melt will coalesce and flow to the surface of the parts. Silicon metal is more reflective than silicon nitride, so it has a more silver appearance than the nitrided material.

Optical microscopy was also employed to examine some of the nitrided materials. Selected samples were sectioned, mounted and polished for metallography. This approach sought to identify pores and specular regions within the material. No reflective silicon or iron silicide inclusions larger than 10  $\mu\text{m}$  were ever found.

Chemical analyses were performed on nitrided materials to track the chemical reactions which occur during nitriding. Both nitrogen and oxygen contents were measured by a Leco inert gas fusion (IGF) spectrometer and a Leco combustion spectrometer, respectively. An inductively-coupled plasma emission (ICP) spectrometer was used to measure the silicon content, and this value was used to normalize the other data, so that nitrogen and oxygen content were always expressed as N/Si and O/Si. The exact N/Si ratio of a nitrided material depended on the composition of the additives. For example, if  $\text{TiO}_2$  is present, it converts to TiN during nitriding, raising the N/Si ratio.

The oxygen-to-silicon ratio was also tracked as a means of assessing oxygen management. The control of oxygen content is very important to the amount of densification occurring during the subsequent sintering process. The correct oxygen content is also requisite to the formation of appropriate



intergranular crystal phases in the final product. Some of the total oxygen in the material comes from oxidation of the silicon powder before nitriding to form a silica layer that envelopes the particles. The amount of oxygen introduced by this route is variable, and requires careful process control. Another possible route for extraneous oxide introduction is from leakage of the outer seals on the nitriding furnace, or from incomplete purging and outgassing practices. The deliberate oxygen added to the material in the form of yttria and alumina may need to be reduced by the substitution of some aluminum nitride for aluminum oxide. Conversely, additional oxygen may be introduced by adding titania instead of titanium nitride. This flexibility in oxygen management allows for the engineering of not only the sinterability of the material but also allows for certain material properties influenced by the intergranular phases.

Titanium nitride was a desired constituent in the product material, but instead of adding it directly to the powder blend, titania was added to increase the oxygen content. The aluminum oxide/nitride and the titanium oxide/nitride ratios in the starting powders both provide flexibility to the control of oxygen in the final product. Table 3.23 shows chemical analyses of six different materials compositions after both prenitriding and nitriding. These data provide useful insight into how compositions change during nitriding.

**Table 3.23 – Chemical Analysis of Six Compositions Following Prenitriding and Nitriding**

Prenitride						
Compo- sition	6/3/2	8/2/2	8/1/2	5/2/3	4/7/1	4/4/1/3
Y w/o	5.12	7.38	6.56	4.82	2.58	3.35
Al w/o	2.44	1.80	1.00	1.71	4.93	5.93
Ti w/o	1.69	1.82	1.75	2.59	0.93	0.98
Fe w/o	0.26	0.30	0.30	0.31	0.30	0.32
Si w/o	79.93	79.38	81.78	82.17	79.56	79.68
O w/o	5.76	5.65	5.03	5.37	6.52	4.84
N w/o	4.71	3.61	3.56	3.03	5.12	4.84
Full Nitride						
Compo- sition	6/3/2	8/2/2	8/1/2	5/2/3	4/7/1	4/4/1/3
Y w/o	2.44	3.96	3.09	2.38	2.11	1.62
Al w/o	1.65	1.17	0.68	1.14	3.82	4.05
Ti w/o	1.23	1.17	1.15	1.72	0.62	0.65
Fe w/o	0.20	0.20	0.20	0.20	0.21	0.21
Si w/o	53.48	53.07	54.78	54.52	54.74	54.29
O w/o	4.01	3.96	3.68	3.74	4.90	4.15
N w/o	36.99	36.47	36.41	36.29	33.54	34.99

The use of titania as a precursor for titanium nitride was a novel innovation introduced during this project. The addition of titania not only offers the use of a less expensive raw material but also provides flexibility in nitrogen and oxygen management. As the titania is converted to titanium nitride during the nitriding process, oxygen is transferred into the mixed oxide/oxy-nitride additive phases. This shifts the oxidation states of the cations in the oxy-nitride compounds away from the high-nitrogen content compositions and closer toward purely oxide compositions (e.g.  $\text{SiY}_2\text{O}_5$ ,  $\text{Si}_2\text{Y}_2\text{O}_7$ ). A typical high-oxygen oxy-nitride phase observed in program materials was  $\text{Y}_{10}\text{Si}_6\text{N}_2\text{O}_{24}$ . The low-nitrogen compositions have a higher solubility for alpha silicon nitride, so they accelerate the sintering kinetics and the transformation from  $\alpha$  to  $\beta$   $\text{Si}_3\text{N}_4$  during sintering. Beta silicon nitride is

formed from alpha by a dissolution-precipitation mechanism. The alpha phase is soluble in the oxide/oxy-nitride liquid, but precipitates out to form the beta phase. During sintering, a highly oxidized melt promotes faster sintering kinetics because it has lower viscosity, and promotes increased conversion of alpha to beta (compared to a liquid phase with less oxygen and more nitrogen). The beta phase forms acicular grains which increase the toughness of the product material, so a low- $\alpha$  or an all- $\beta$  microstructure is highly desirable.

It was observed during this program that the higher the aluminum and oxygen contents in the system, the higher the amount of  $\beta$ - $\text{Si}_3\text{N}_4$  that formed, as shown in Figures 3.8 and 3.9. Figure 3.8 shows a particularly striking relationship between aluminum content and fraction of  $\alpha$  phase. It demonstrates that as the Al/Si ratio varies from 0.015 to 0.07, the  $\alpha/\beta$  ratio goes from 1 to 0, and this relationship exhibits very little scatter about an empirically-fitted, exponential decay function. Interestingly, neither of the high aluminum content 4/7/1 or 4/4/1/3 compositions contained any  $\alpha$ - $\text{Si}_3\text{N}_4$  at all after nitriding. It is conventionally believed that the  $\alpha$  to  $\beta$  conversion is essential to densification during the subsequent sintering process. Both of these compositions, however, sintered to full density even though they contained no alpha phase at the outset of sintering. This is a significant finding, therefore, on the mechanism of sintering. This observation contradicts almost all published references to requirements for  $\text{Si}_3\text{N}_4$  densification.

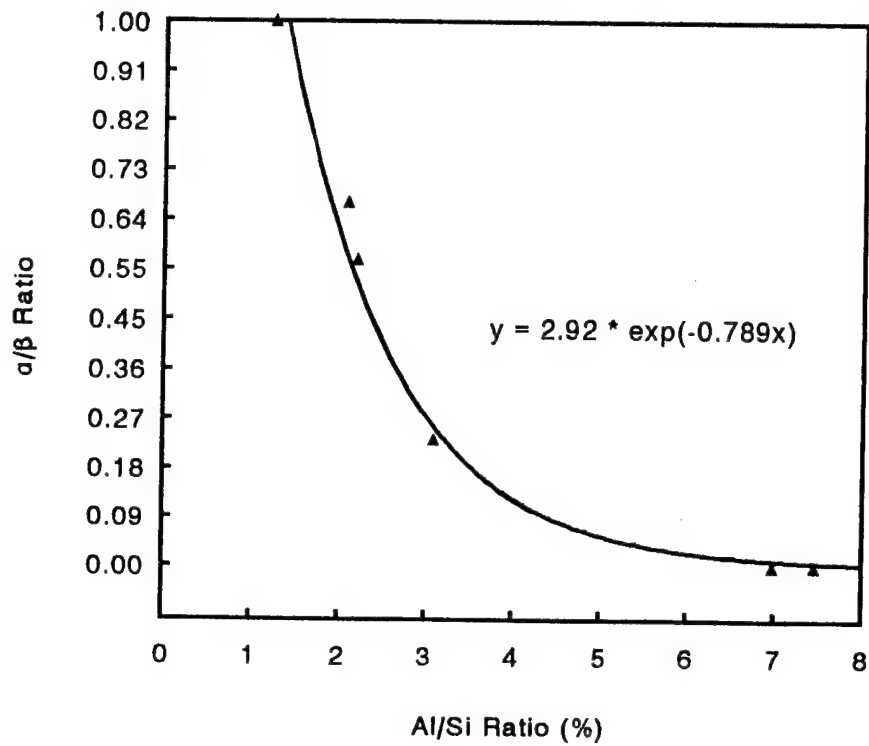


**Figure 3.8** The  $\alpha / \beta$  Phase Ratio vs. Aluminum Content in  $Si_3N_4$  after full nitriding treatment

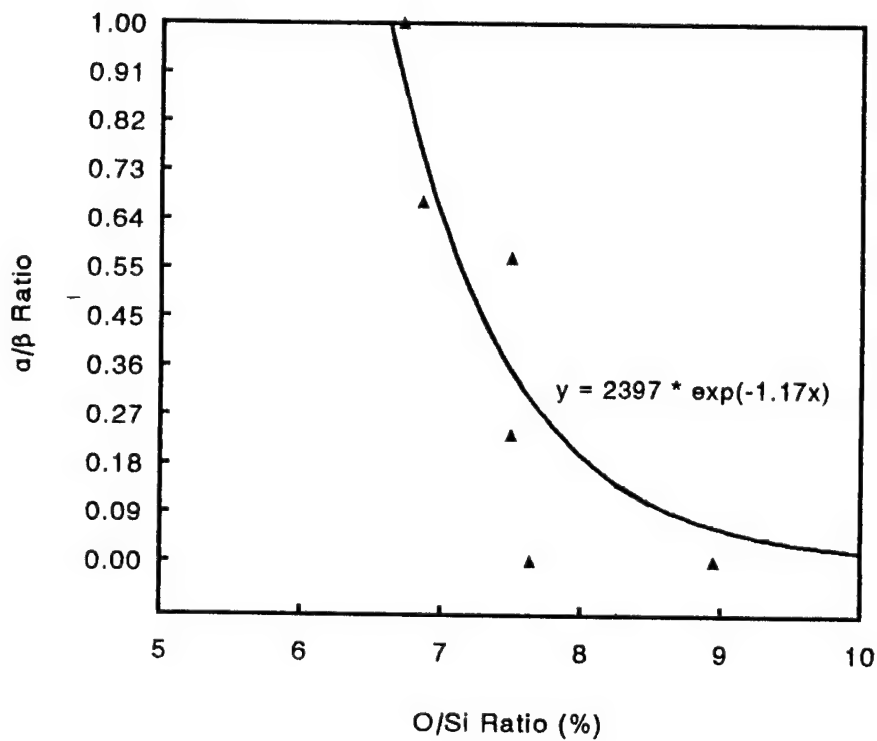


**Figure 3.9** The  $\alpha / \beta$  Phase Ratio vs. Oxygen Content in  $Si_3N_4$  after full nitriding treatment

Samples of the nitrided material were used for x-ray diffraction analysis in a powder diffractometer. An x-ray diffraction spectrum from one of these samples is shown in Figure 3.10. An analysis of this spectrum found no titanium oxide, only titanium nitride, demonstrating that the predicted thermodynamics were correct. Similar analyses determined that if a glassy phase were present at all, it existed as only a small fraction of the intergranular oxide phases; it was not detectable in the analysis.

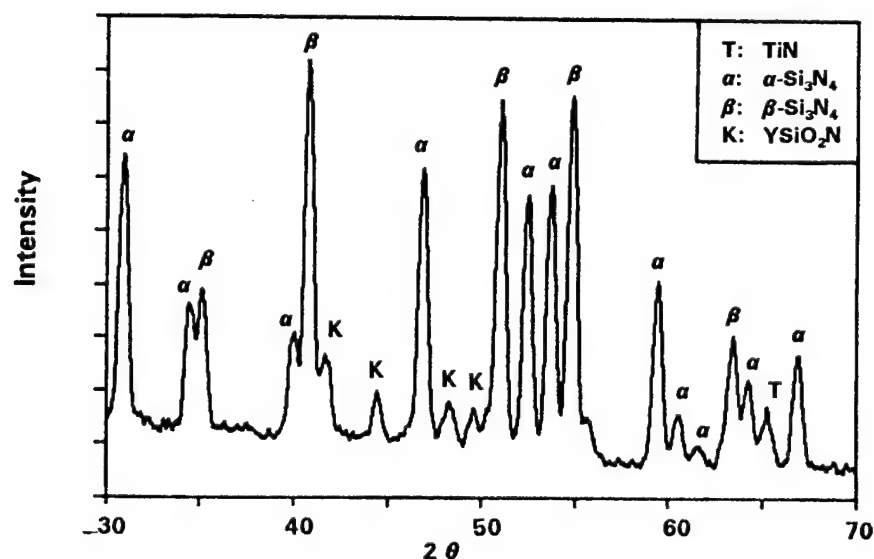


**Figure 3.10** X-ray angular intensity spectrum from program material after nitriding.

Further x-ray diffraction analyses of the nitrided material showed that the oxide system is converted to a complex oxynitride during nitriding. The phases that were identified in each composition are listed in Table 3.24. The most frequently observed oxynitride was  $Y_{10}Si_6N_2O_{24}$ . The presence of oxynitride phases is known to improve the sintering kinetics of silicon nitride,

compared to oxide-only sintering aids, because they have a lower melting point.

**Table 3.24 — Intergranular Phase Identification**

	Phases Found
6/3/2	TiN, $Y_{10}Si_6N_2O_{24}$ , $Y_2SiO_5$
8/2/2	TiN, $Y_{10}Si_6N_2O_{24}$
8/1/2	TiN, $Y_{10}Si_6N_2O_{24}$
5/2/3	TiN, $Y_{10}Si_6N_2O_{24}$ , $Y_2SiO_5$
4/7/1	Amorphous, TiN
4/4/1/3	Amorphous, TiN

### 3.7 Sintering

The goal for this task was to develop an optimized sintering cycle for the program materials. An optimized sintering cycle is defined as one where the temperature-time profile and the furnace atmosphere result in a sintered density level sufficient for containerless HIPing, and which results in good material properties such as density, hardness and fracture toughness, and homogeneous microstructure. It was our strategy to conduct sintering on a pressureless basis (ambient).

To address these issues the sintering task was initiated by: (a) processing available samples through Cercom's standard silicon nitride sintering cycle and (b) engineering a DOE using the Taguchi method.

### **3.7.1 Baseline Data Development**

Before optimization work on the sintering cycle began, a series of baseline runs was carried out using a standard process cycle used for Cercom PSG-H silicon nitride. This cycle consists of an 1800°C hold for 10 hours in an inert gas atmosphere followed by a HIP cycle at 1825°C and 34 MPa (5000 psi) for 1 hour. This cycle was used on program material to generate "first impressions" and to develop initial baseline data. It was not possible to fully evaluate the success of particular sintering cycles without HIPing the material afterwards to achieve full density. Therefore, all of the sintering studies used the standard HIP cycle for Cercom PSG-H to densify the materials so they could be characterized. The properties of the materials produced in these test cycles are shown in Table 3.25.

Four nitrided rods of a 6/3/2 composition were selected for study. These rods were produced from powder mixtures prepared during one of the powder blending efforts. The processing varied for each powder as did the  $Y_2O_3$  and  $TiO_2$  raw material grades.

All rods were placed in a  $Si_3N_4$  crucible and set into the furnace. The furnace chamber was back-filled with inert gas and thermally cycled using the standard time/temperature profile. After sintering, all rods were HIPed to achieve maximum density.

Multiple specimens from each rod were prepared by slicing, mounting and polishing. All specimens were optically analyzed and tested for hardness and toughness by indentation.

The results for each rod were very similar, indicating that powder processing and raw material selection had little influence. The hardness and toughness values were approximately 6% below those associated with Cercom's PSG-H silicon nitride. Therefore, optimization of the thermal

processing cycle was found to be necessary to improve these material properties.

Optical examination of polished specimens revealed a two-toned cross-section. A dark-colored concentric casing or band had developed on the periphery of each rod. The banded region was somewhat porous, as shown in Figure 3.11, with pore volume decreasing from the surface to the center of the rod.

This observation, coupled with the measured weight losses during sintering, indicates that the sintering temperature was too high or the cycle time was too long for this particular composition. The measured weight loss for the rods was 2.7 percent on average. In contrast, this same cycle produces only a nominal weight loss of about 0.4 percent for standard Cercom  $\text{Si}_3\text{N}_4$  grades.

**Table 3.25 – Physical and Mechanical Properties of Sinter-HIPed  $\text{Si}_3\text{N}_4$  Using Cercom Standard Cycle**

Condition	Powder Process			Composition	Sintered Density g/cc	HIPed Density g/cc	Hardness Kg/mm <sup>2</sup>	Toughness MPa√m
	Solvent	Y <sub>2</sub> O <sub>3</sub>	TiO <sub>2</sub>					
1	CDA-19 —	Comminuted Molycorp	Rutile	6/3/2	3.272	3.279	1384	5.42
2	CDA-19	Nippon	Anatase	6/3/2	3.264	3.275	1391	5.34
3	Azeotrope w/dispersant	Comminuted Molycorp	Anatase	6/3/2	3.268	3.280	1377	5.48
4	Azeotrope w/dispersant	Nippon	Rutile	6/3/2	3.267	3.278	1372	5.36



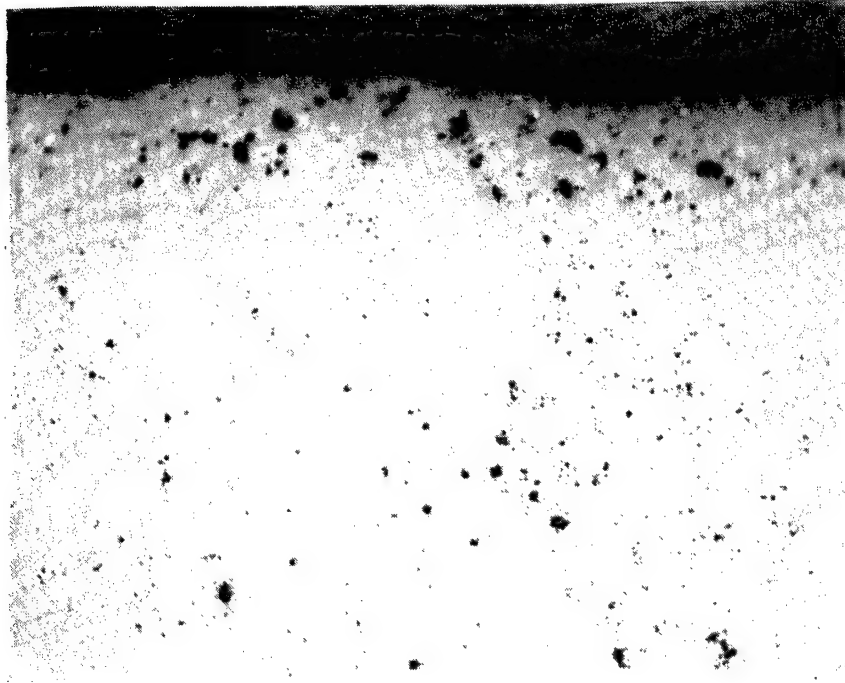


**Figure 3.11.** Optical micrograph (bright field illumination) of 6/3/2 HIPed  $\text{Si}_3\text{N}_4$  at 200X.

### **3.7.2 Sintering Taguchi Matrix**

A DOE was laid out for this task, using the Taguchi method, with the objective of determining an optimum combination of time, temperature, and atmosphere for sintering. Table 3.26 lists the factors and levels chosen for the design matrix. Three factors were picked at two corresponding levels each. Factor 1 is the sintering soak temperature at two levels, 1750°C (3182°F) and 1800°C (3272°F) respectively. Factor 2 is time at temperature. The levels include 2 and 6 hours. Factor 3 is atmosphere, with inert gas and nitrogen defining the levels.

Four material compositions ( 6/3/2, 8/2/2, 8/1/2, 5/2/3 ) in the form of prenitrided balls were included in the DOE. The balls were fabricated during the earlier green-machining study. Cercom's standard monolithic silicon nitride (6/3) was also included for comparison as well as two new

experimental compositions defined as 4/7/1 and 4/4/1/3. The last composition gives the weight percents for  $Y_2O_3$ /  $Al_2O_3$ /  $TiO_2$ /  $AlN$ . Aluminum nitride was used in the latter composition to decrease the oxygen content of the intergranular phase. That is, a portion of the  $Al_2O_3$  addition was replaced in favor of  $AlN$ . This composition was later to become the final selection to be used in the program-deliverable materials.

The standard Taguchi array for this mixed level system is shown in Table 3.27. The Taguchi method dictates the 4 sets of conditions listed in the array and are designated numerically 1 through 4.

**Table 3.26 – Factors and Levels for the Sintering DOE.**

Factor/Level	1	2
Temperature, °C	1700	1750
Time, Hours	2	6
Atmosphere	N <sub>2</sub>	Inert Gas

**Table 3.27 – Taguchi Array for the Sintering DOE.**

Condition	Temperature, °C	Time, hrs.	Atmosphere
1	1700	2	N <sub>2</sub>
2	1700	6	Inert Gas
3	1750	2	Inert Gas
4	1750	6	N <sub>2</sub>

Table 3.28 tabulates the density and weight loss for all of the compositions sintered per the Table 3.27 array.

**Table 3.28 – Results of the Sintering DOE**

Composition	Sintering Conditions			Sintering	
	Temp (°C)	Time (Hr)	Atmosphere	Wt Loss %	Density g/cc
6/3/2	1700	2	N <sub>2</sub>	1.24	3.185 (96.8%)
6/3/2	1700	6	Inert Gas	1.94	3.248 (98.7%)
6/3/2	1750	2	Inert Gas	1.43	3.206 (97.4%)
6/3/2	1750	6	N <sub>2</sub>	2.30	3.284 (99.8%)
8/2/2	1700	2	N <sub>2</sub>	0.51	3.165 (95.5%)
8/2/2	1700	6	Inert Gas	1.01	3.273 (98.8%)
8/2/2	1750	2	Inert Gas	0.39	3.194 (96.4%)
8/2/2	1750	6	N <sub>2</sub>	1.51	3.297 (99.5%)
8/1/2	1700	2	N <sub>2</sub>	0.41	3.118 (94.2%)
8/1/2	1700	6	Inert Gas	1.41	3.205 (96.8%)
8/1/2	1750	2	Inert Gas	0.84	3.096 (93.5%)
8/1/2	1750	6	N <sub>2</sub>	2.03	3.283 (99.2%)
5/2/3	1700	2	N <sub>2</sub>	0.40	2.951 (89.9%)
5/2/3	1700	6	Inert Gas	1.57	3.160 (96.2%)
5/2/3	1750	2	Inert Gas	1.32	3.061 (93.2%)
5/2/3	1750	6	N <sub>2</sub>	1.74	3.256 (99.1%)
6/3	1700	2	N <sub>2</sub>	0.22	3.104 (94.9%)
6/3	1700	6	Inert Gas	0.32	3.222 (98.5%)
6/3	1750	2	Inert Gas	0.17	3.160 (96.6%)
6/3	1750	6	N <sub>2</sub>	0.27	3.259 (99.7%)
4/7/1	1700	2	N <sub>2</sub>	0.63	3.168 (97.8%)
4/7/1	1700	6	Inert Gas	0.95	3.198 (98.7%)
4/7/1	1750	2	Inert Gas	0.60	3.171 (97.9%)
4/7/1	1750	6	N <sub>2</sub>	1.17	3.230 (99.7%)
4/4/1/3	1700	2	N <sub>2</sub>	0.10	3.191 (98.2%)
4/4/1/3	1700	6	Inert Gas	0.66	3.224 (99.2%)
4/4/1/3	1750	2	Inert Gas	0.09	3.199 (98.4%)
4/4/1/3	1750	6	N <sub>2</sub>	0.34	3.244 (99.8%)

Based on the results from this DOE, it was concluded that 1700°C was the better sintering temperature because it resulted in less weight loss with little or no sacrifice to density. No significant difference was seen between the two sintering gases, so inert gas was selected, because it prolongs the

life of the sintering furnace. The optimum sintering time was not selected at this point. Instead, work proceeded on HIPing studies, and material was analyzed after HIPing to determine optimum combinations of sintering and HIPing conditions.

### 3.8 Hot Isostatic Pressing

Hot isostatic pressing (HIPing) of silicon-based ceramics is a thermal processing technology for improving the mechanical and thermo-mechanical properties of materials and for increasing product reliability. HIP processing, as shown in Figure 3.12, can be used either as a post-sintering treatment (sinter-HIP) or used concurrently with sintering. Both processes have the ability to produce fully isotropic bodies at theoretical density--an important advance in the development of structural ceramics.

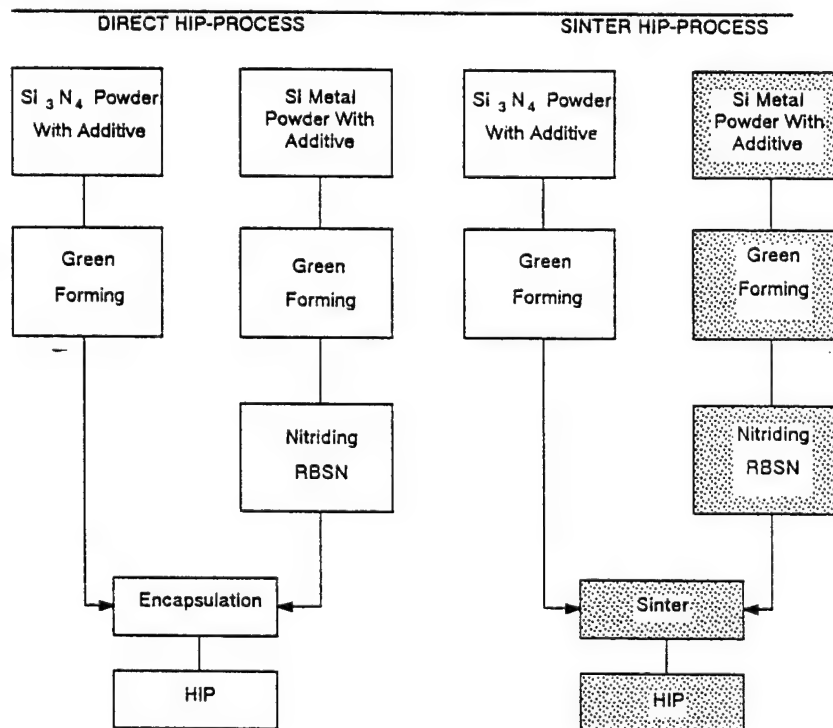


**Figure 3.12.** Flow diagram of possible hot isostatic pressing (HIPing) procedures. Cercom's process of choice is the sinter-HIP technique using RBSN processing (shaded route).

Encapsulation HIP is a densification process which involves vacuum-encapsulating a green-formed article and applying a high gas pressure concurrently with temperature. The encapsulant or container is a temperature and pressure resistant material and serves as a pressure-transmitting membrane during processing. Theoretically dense isotropic bodies are produced with significant improvements in physical properties and overall material reliability (Weibull modulus,  $m$ ,  $> 12$ ).

However, the encapsulation HIP process, although effective and quite versatile, is a high-cost process because of the expense involved with preparing and removing the container material. Additionally, the contact surface of processed components can show chemical variation to significant depths within the part due to reaction between the container and the part being HIPed. The outer layer of affected material must be removed by diamond grinding and, therefore, the process detracts considerably from the concept of "net shaping".

Cercom investigated the alternate HIP process technique known as "sinter-HIP" or sometimes referred to as "containerless HIPing" because of the cost savings and improved quality that may be realized by eliminating the encapsulation process.

Sinter-HIP processing is accomplished using two different, thermal treatments. The first includes pressureless sintering an SRBSN preform to a closed porosity state. All open porosity must be eliminated, and a density greater than 90 percent of theoretical is required so that the surface of the article can act as the pressure transmitting membrane. The second treatment uses HIPing to remove all residual porosity from the sintered article to achieve theoretical density.

In theory, the sinter-HIP process should remove all residual porosity and produce a theoretically dense body. However, in practice, the application of

this process to  $\text{Si}_3\text{N}_4$  is not straightforward. Major open technical issues include; (a) the influence of microstructural characteristics of the sintered material; (b) the minimum density requirements of the sintered material; and (c) the solubility of Ar or  $\text{N}_2$  (used to supply pressure) in the silicon nitride intergranular phase.

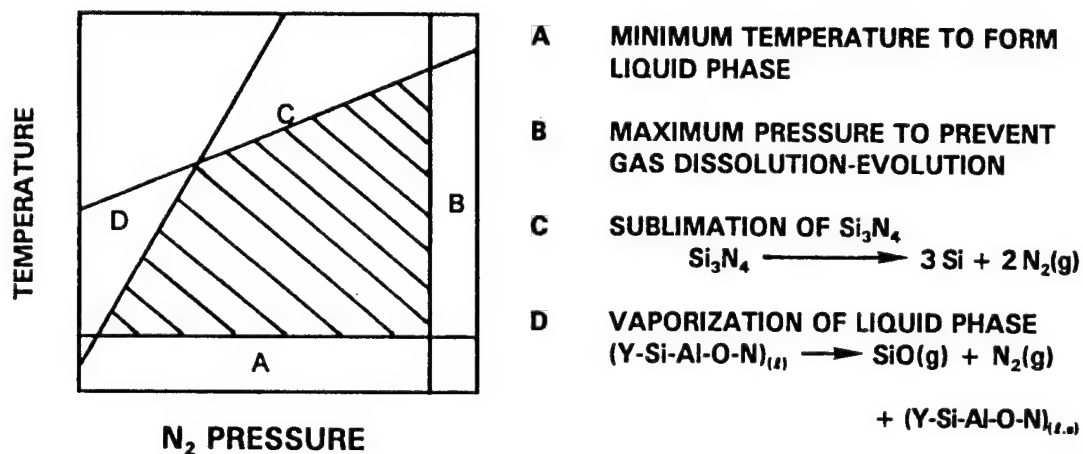


**Figure 3.13** A map of temperature-pressure space in the HIPing process.

*Microstructural Effects:* The major microstructural feature that determines processability is the degree of acicularity of the  $\beta\text{-Si}_3\text{N}_4$  grains resulting from the initial sintering step. The interlocked  $\beta$  grain network produces a "bridging" effect that prevents the elimination of pores trapped within the tight network. Cercom has found that the effect of microstructural bridging can be significantly reduced by maintaining some  $\alpha$  phase in the sintered body. During HIPing, the  $\alpha$  grains contribute to the formation of localized liquids that allow the network to rearrange under high pressure and thereby facilitate pore removal.

*Sintered Density Requirements:* Density increases have been observed only when the density of the sintered silicon nitride exceeds some threshold value. Data also show that the use of nitrogen as the pressurizing gas, in contrast to argon, leads to higher densities and strengths because decomposition of silicon nitride and certain intergranular phase compounds is suppressed. The literature is not clear on this issue, but appears to support the observations that minimum density requirements will be dependent upon composition and microstructure.

*Dissolved Gases:* Equilibrium partial pressures of nitrogen in the intergranular phase are determined by the activity of silicon and by the external gas pressure. The material is exposed directly to the gas environment during processing and, therefore, the solubility of  $N_2$  and/or Ar in  $Si_3N_4$  will increase as temperature and pressure increase. The dissolved gas can supersaturate the intergranular phase and remain trapped if furnace cooling and decompression are faster than the rate of gas diffusion, resulting in the formation of new voids or pores -- in effect reversing the densification process. The effects of supersaturation are evidenced by surface blistering and spalling and occur upon reheating the cooled body.

One of the goals of HIP process optimization is to determine the ranges of temperature and pressure that are appropriate to a particular material. If the temperature is too low, the sintering aids will not liquefy, and densification will not occur. If the temperature is too high, however, there will be decomposition of the silicon nitride. If the pressure is too low, the liquid phase components of the material will vaporize excessively, whereas, too high a pressure will lead to gas dissolution within the part, causing gas evolution and blistering after pressure release. A map of temperature and pressure for HIPing is presented in Figure 3.13.

The HIP process development conducted in this program was divided into three stages. In the first stage, a baseline HIP cycle was run using parameters developed during previous Cercom work, and using the materials produced in the sintering DOE described in Section 3.7.2. Extensive microstructural, chemical, and crystallographic analyses were conducted on materials both before and after this HIP cycle. The subsequent two stages to the HIP development were a first and second HIP DOE, designed to determine the relationships between material compositions, HIP process cycles, and resulting material properties.

### ***3.8.1 Preliminary HIP cycle development***

All of the specimens produced during the first DOE for sintering (Section 3.7.2) were HIP processed at 1825°C (3317°F) in a N<sub>2</sub>/Ar environment at 34 MPa (5,000 psi). Decompression was not controlled and the pressure vessel was allowed to cool at its intrinsic decay rate. The resultant densities are shown in Figure 3.14 and in Table 3.29. No significant weight changes were observed. It should also be noted that determining the theoretical density of each silicon nitride composition is an empirical procedure. The compositions of the intergranular phases are not precisely known and, therefore, calculated theoretical densities are not possible. Table 3.30 gives the empirically-derived theoretical density for each material composition. These values were used in all calculations where "percent of theoretical" or "relative density" presentations were required. Further examination of the data indicated that a minimum sintered density is required for HIPing to be effective. The "threshold density" varies, as expected, among the compositions as shown in Figure 3.14.



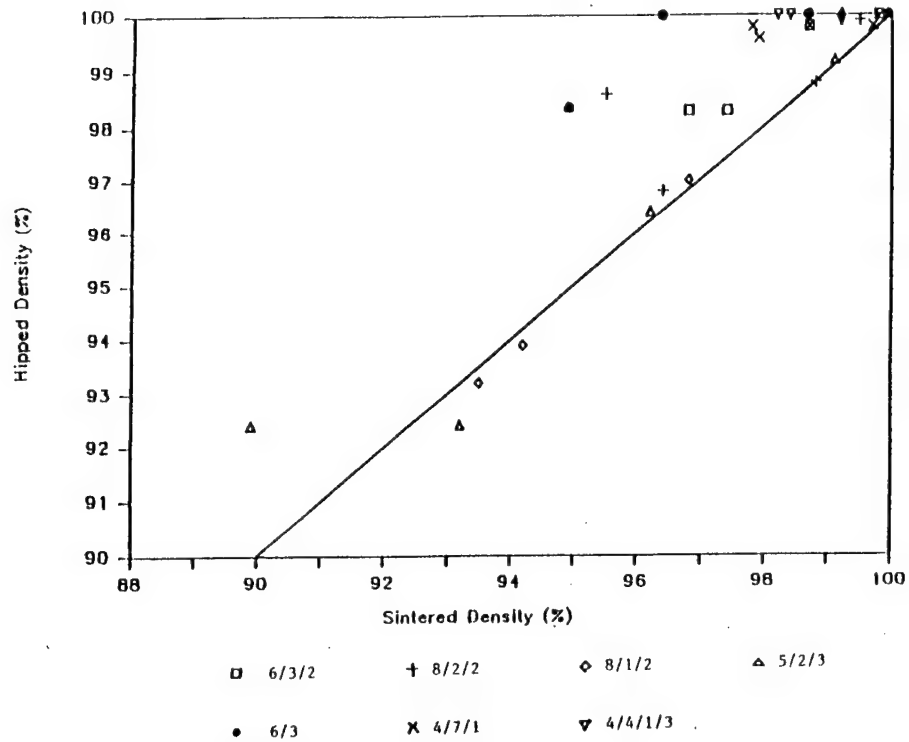


**Figure 3.14.** Relative densities after HIPing as a function of those before HIPing in  $\text{Si}_3\text{N}_4$  containing various amounts of  $\text{Al}_2\text{O}_3$ ,  $\text{Y}_2\text{O}_3$ ,  $\text{TiO}_2$  and  $\text{AlN}$  additives. HIPing conditions are  $1825^\circ\text{C}$  and 5000 psi.

**Table 3.29 – Theoretical Densities of Program Materials Derived Empirically**

Composition	Density $\text{g/cm}^3$
6/3/2	3.290
8/2/2	3.313
8/1/2	3.310
5/2/3	3.284
6/3	3.270
4/7/1	3.240
4/4/1/3	3.250

**Table 3.30 – Densities Resulting from First HIP Cycle**

Composition	Density After Sintering	Density After HIPing
	g/cc (% of theo.)	g/cc(% of theo.)
6/3/2	3.185 (96.8%)	3.233 (98.3%)
6/3/2	3.248 (98.7%)	3.284 (99.8%)
6/3/2	3.206 (97.4%)	3.233 (98.3%)
6/3/2	3.284 (99.8%)	3.289 (100%)
8/2/2	3.165 (95.5%)	3.265 (98.6%)
8/2/2	3.273 (98.8%)	3.273 (98.8%)
8/2/2	3.194 (96.4%)	3.206 (96.8%)
8/2/2	3.297 (99.5%)	3.310 (99.9%)
8/1/2	3.118 (94.2%)	3.107 (93.9%)
8/1/2	3.205 (96.8%)	3.211 (97.0%)
8/1/2	3.096 (93.5%)	3.084 (93.2%)
8/1/2	3.283 (99.2%)	3.309 (100%)
5/2/3	2.951 (89.9%)	3.035 (92.4%)
5/2/3	3.160 (96.2%)	3.165 (96.4%)
5/2/3	3.061 (93.2%)	3.036 (92.4%)
5/2/3	3.256 (99.1%)	3.258 (99.2%)
6/3	3.104 (94.9%)	3.213 (98.3%)
6/3	3.222 (98.5%)	3.263 (99.8%)
6/3	3.160 (96.6%)	3.272 (100%)
6/3	3.259 (99.7%)	3.270 (100%)
4/7/1	3.168 (97.8%)	3.233 (99.8%)
4/7/1	3.198 (98.7%)	3.233 (99.8%)
4/7/1	3.171 (97.9%)	3.227 (99.6%)
4/7/1	3.230 (99.7%)	3.235 (99.8%)
4/4/1/3	3.191 (98.2%)	3.249 (100%)
4/4/1/3	3.224 (99.2%)	3.247 (99.9%)
4/4/1/3	3.199 (98.4%)	3.248 (100%)
4/4/1/3	3.244 (99.8%)	3.248 (100%)

### 3.8.1.1 *Microstructure and Properties Characterization*

Figures 3.15 and 3.16 are typical photomicrographs of the HIP-treated 6/3/2 material at 1000 and 5000X, respectively. Backscatter electron (BSE) imaging techniques were used to produce these images. BSE imaging enhances the contrast between various phases and shows microstructural detail. These figures show that the  $\text{Si}_3\text{N}_4$  microstructure contains both acicular and equiaxed grain morphologies. The intergranular phase or secondary phase appears white in the photomicrographs because compositionally this phase contains relatively high atomic number (Z) atoms; e.g., yttrium. Clearly the photomicrographs show that the  $\text{Si}_3\text{N}_4$  grains are surrounded by the intergranular phase on a continuous basis and are uniformly dispersed.

In addition to the intergranular phase this composition also contains the TiN phase. The TiN forms during thermal processing of the material and its precursor is the  $\text{TiO}_2$  (anatase) addition to the powder mix. That is, the TiN forms from the  $\text{TiO}_2$  through a reconstructive process during the nitridation process of the silicon. The TiN would therefore, reside between silicon nitride grains as in a particulate composite material. Unfortunately, Ti also has a relatively high atomic number and is an efficient reflector in the BSE mode. Therefore, TiN appears white on the photomicrograph making it indistinguishable from the intergranular oxide-oxynitride phase. To illustrate, Figures 3.17 and 3.18 are the EDX spectra collected from two reflective (white) regions in the microstructure shown in Figure 3.16. Figure 3.17 shows that the white region designated as Area 1 is the yttrium based intergranular material and Area 2 is the TiN grain(s) as shown in Figure 3.18.

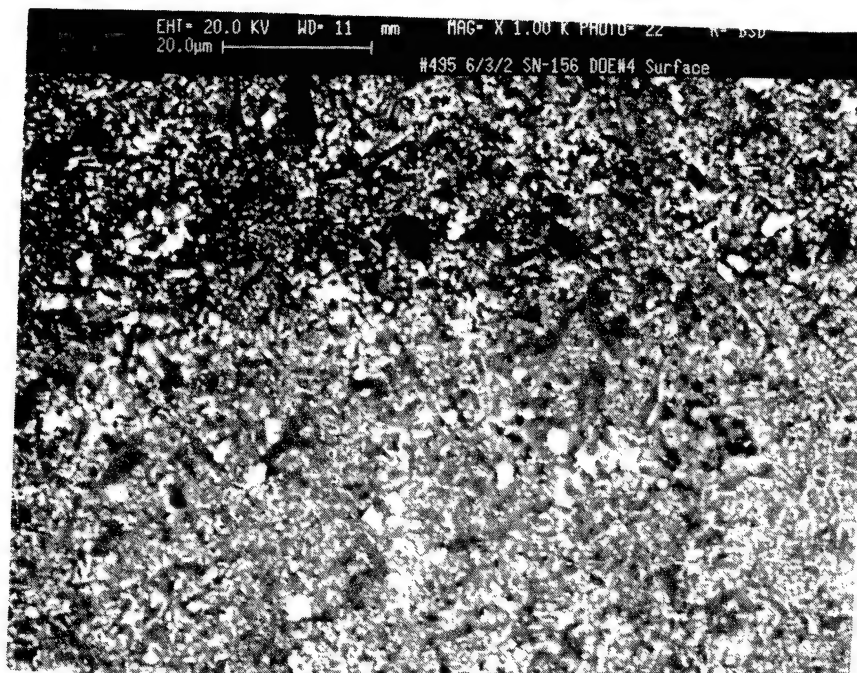


**Figure 3.15.** BSE micrograph of sintered 6/3/2 at 1000X.

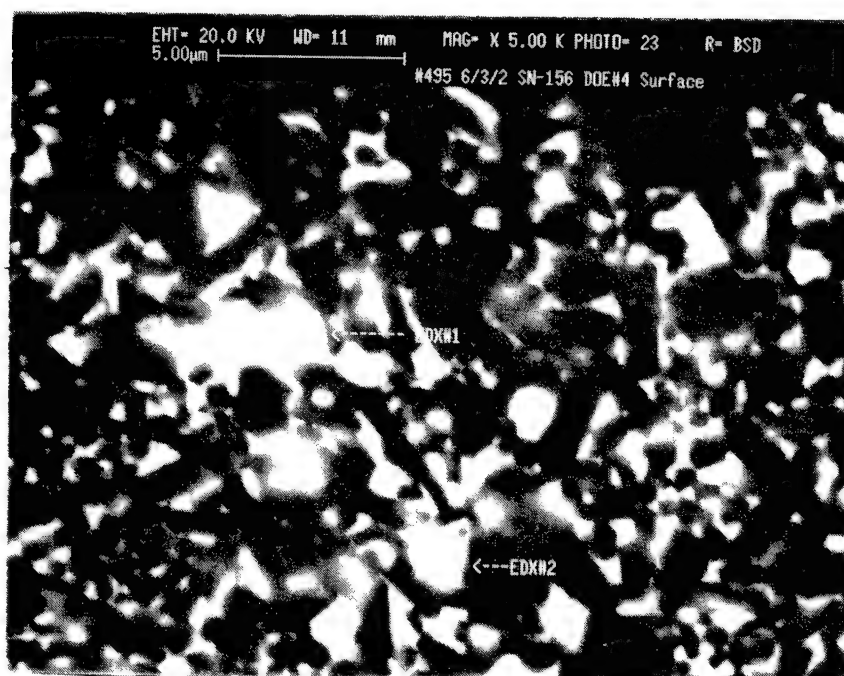


**Figure 3.16** BSE micrograph of sintered 6/3/2 at 5000X.

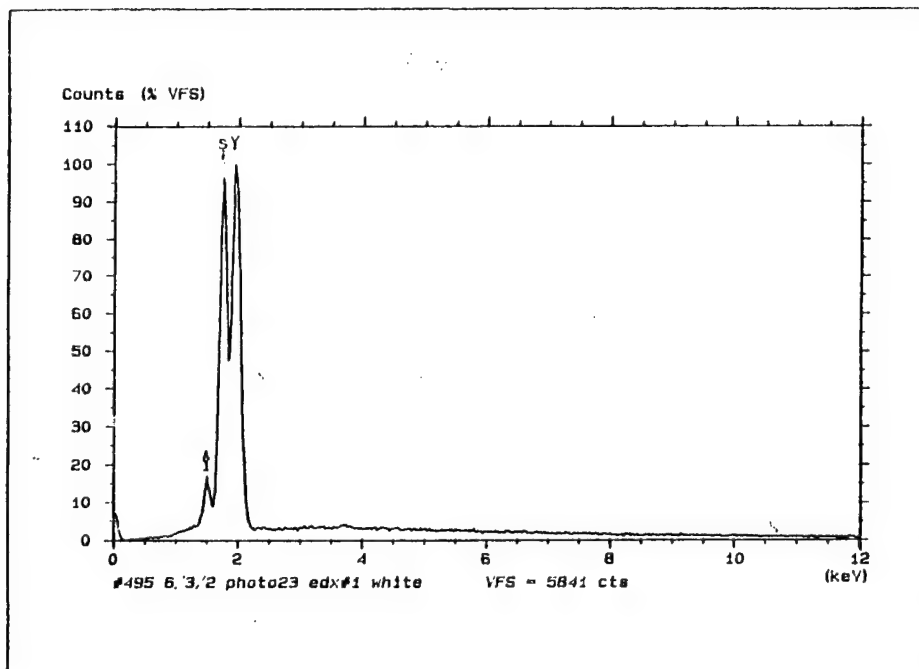


**Figure 3.17.** EDX spectrum from Area #1 in Figure 3.16.

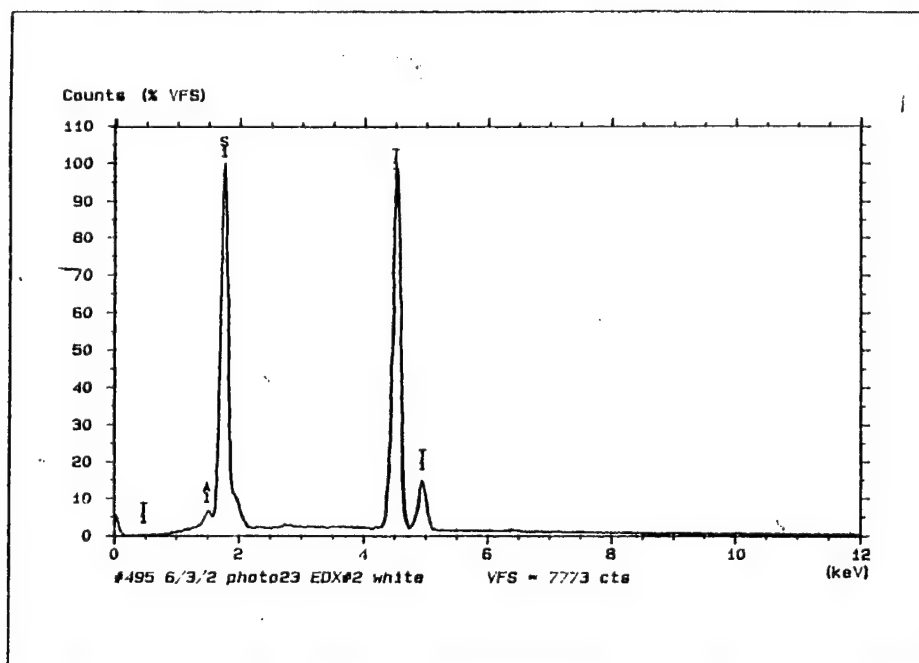


**Figure 3.18.** EDX spectrum from Area #2 in Figure 3.16.

### 3.8.1.2 *Two-toned cross sections*

Optical examination of the specimens resulting from the sintering study (Section 3.7.1) revealed a two-toned cross-section. That is, a dark colored concentric casing or band had developed on the outside regions of each specimen. The dark-banded region was somewhat porous with the pore volume decreasing when traversing the specimen from the surface towards the center.

To elucidate cause and effect, the microstructure of both the dark and light regions were analyzed using BSE imaging. Figures 3.19 and 3.20 represent typical microstructures found in these two regions. Figure 3.19 shows that the dark-banded region contains a larger, more concentrated reflective intergranular phase. Conversely, Figure 3.20 shows a finer, more uniformly distributed reflective phase associated with the lighter colored material. To quantify these observations, an EDX analysis was performed to measure Ti and Al concentration/distribution. This technique is identical to that developed during the powder blending/homogenization studies for determining  $\text{Al}_2\text{O}_3$  and  $\text{TiO}_2$  distribution in blended powder lots. The details of this analysis method are given in Appendix A. Five EDX scans at 1000X were performed in both the dark and light regions. The results are given in Table 3.31 as average Al/Si and Ti/Si ratios. These data show that there is no significant difference in cation ratios between the two color zones. That is, the overall chemistry or the volume percent of the intergranular phase in the two regions is essentially the same.

Therefore, the effect of color banding is caused by the segregation of the intergranular phase. The kinetics for segregation appear to be temperature-related in that the samples evaluated from the sintering DOE (Section 3.7.2) are the higher temperature processed materials.

**Table 3.31 – EDX Analysis for the Two-Toned Cross-Section**

	Dark Region (Surface)	Light Region (Center)
Al/Si	0.0384	0.0359
Ti/Si	0.0193	0.0199

### 3.8.1.3 *Influence of $\text{TiO}_2$ on $\beta\text{-Si}_3\text{N}_4$ Grain Morphology*

Photomicrograph results appear to show that the addition of  $\text{TiO}_2$  promotes the formation of elongated  $\beta\text{-Si}_3\text{N}_4$  grains, i.e., in-situ grain growth. Measured grain lengths range between 15 to 20 micrometers, with corresponding aspect ratios between 10:1 and 40:1. In contrast, typical monolithic silicon nitrides do not show this degree of acicular grain development. Therefore, an analysis was completed to determine if the observed  $\beta$ -grain enhancement was related to sintering or HIPing.

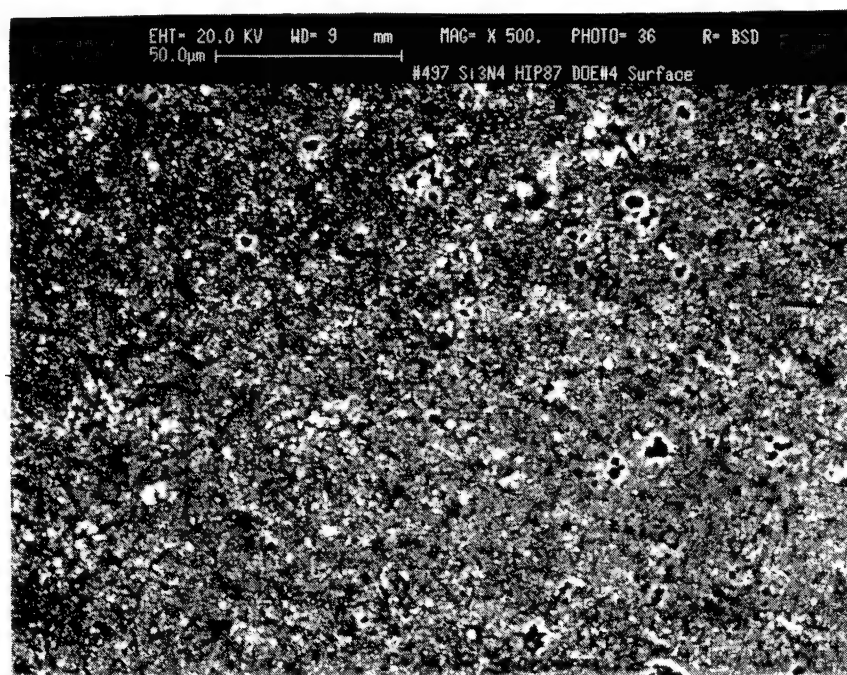


**Figure 3.19.** BSE micrograph of HIPed 6/3/2 in dark region.

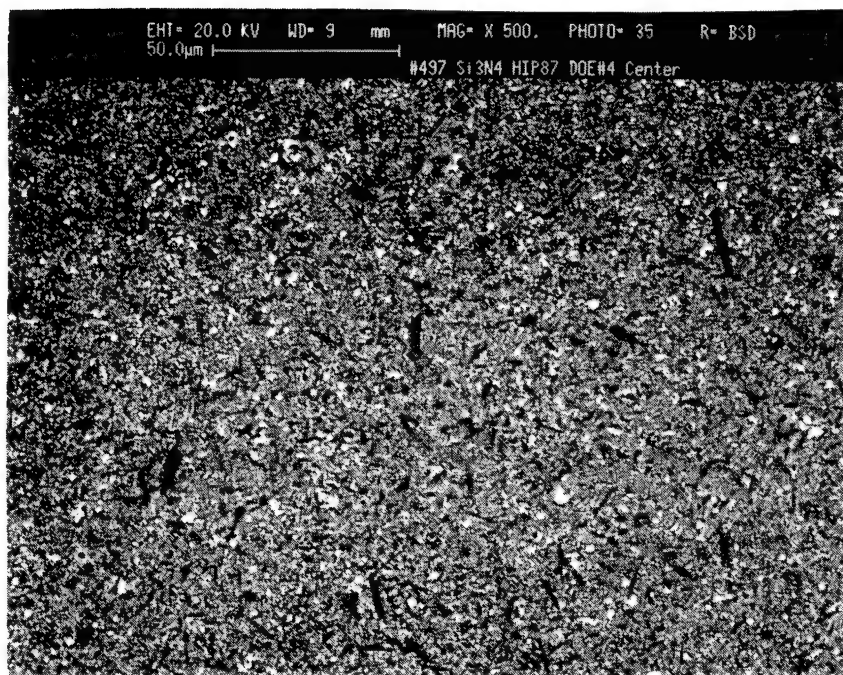


**Figure 3.20.** BSE micrograph of HIPed 6/3/2 in light region.

Figures 3.21 and 3.22 represent the microstructures of the 6/3/2 material after sintering and HIPing, respectively. BSE imaging was again used to enhance the detail in each microstructure. As shown, both microstructures show approximately the same degree of acicularity. Therefore, it can be concluded that grain growth enhancement is directly related to the sintering process and not the HIP treatment.

Figures 3.23 through 3.28 are BSE images of representative microstructures for compositions 6/3/2, 8/2/2, 8/1/2, 5/2/3, 6/3 and 4/4/1/3, respectively. Recall that the third number in the x/y/z notation represents the titania content. Among these figures, 3.27 is the only one representing a composition that did not contain titania. On a comparative basis, the first four compositions listed, represented by Figures 3.23 through 3.26, appear to exhibit the largest fraction of elongated  $\beta$ -grains. That is, the development or the propensity for grain growth is greater in the first four material compositions, which contained the largest amounts of titania.



The related mechanisms for these observations are not known at this time, but they appear to be strongly related to the chemical make-up of the secondary phase. Chemical analysis and x-ray diffraction were performed on all these materials in order to better understand the related kinetics for grain growth. The results of these analyses are given in Section 3.8.1.5, following a short discussion of the mechanical properties of the materials.

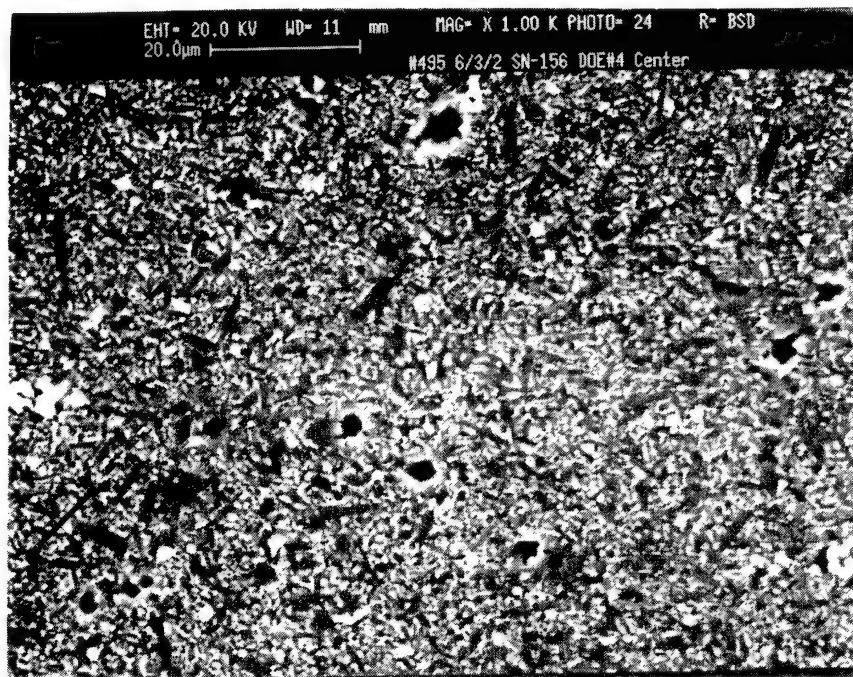


**Figure 3.21.** BSE micrograph of 6/3/2 before HIP.

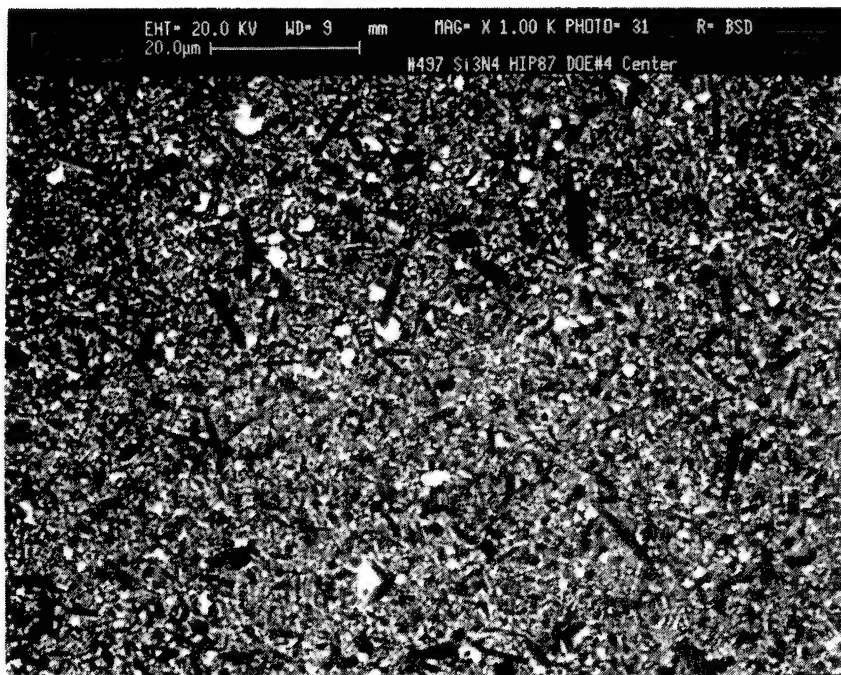


**Figure 3.22.** BSE micrograph of 6/3/2 after HIP.

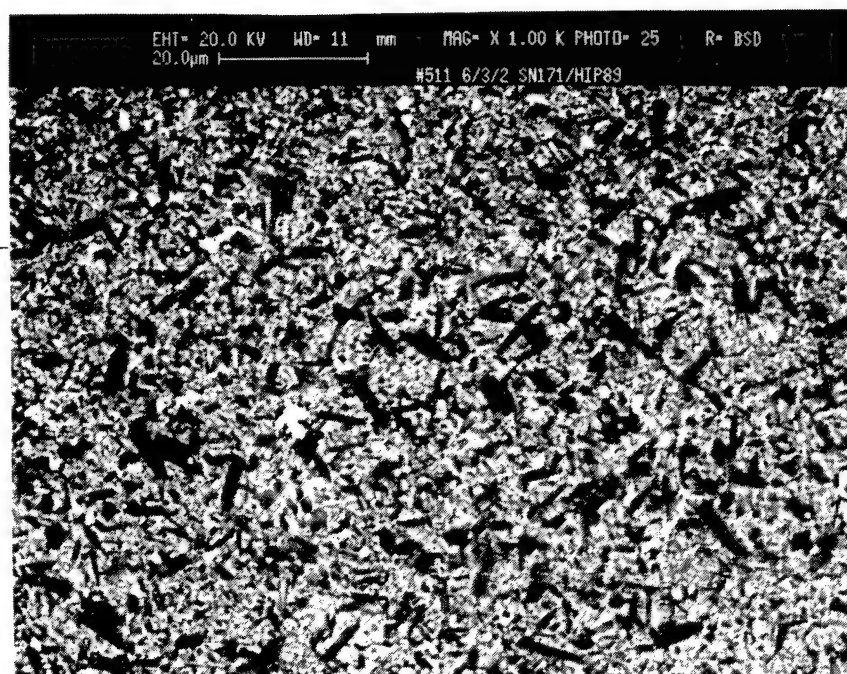


**Figure 3.23.** BSE micrograph of HIPed 6/3/2.

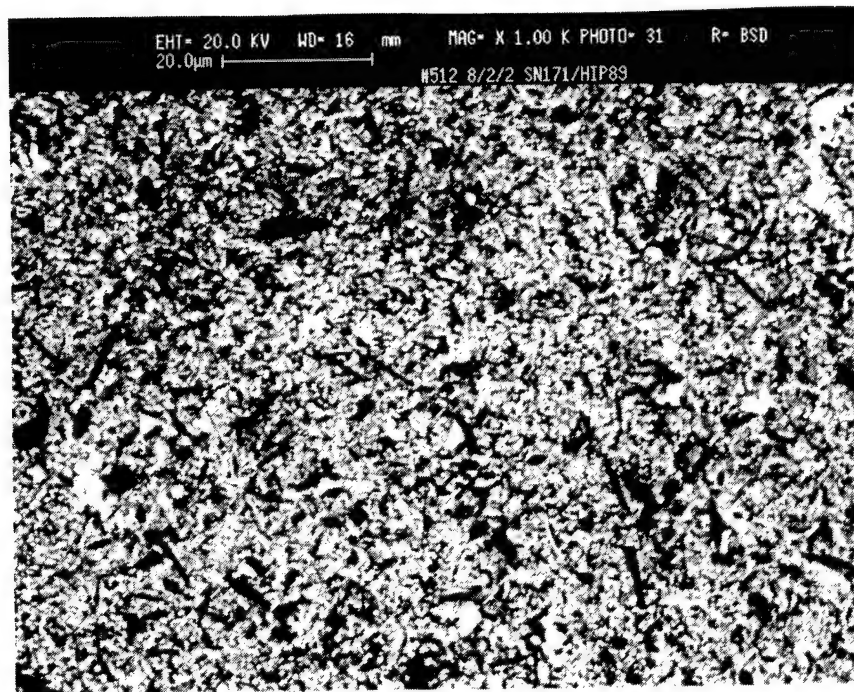


**Figure 3.24.** BSE micrograph of HIPed 8/2/2.

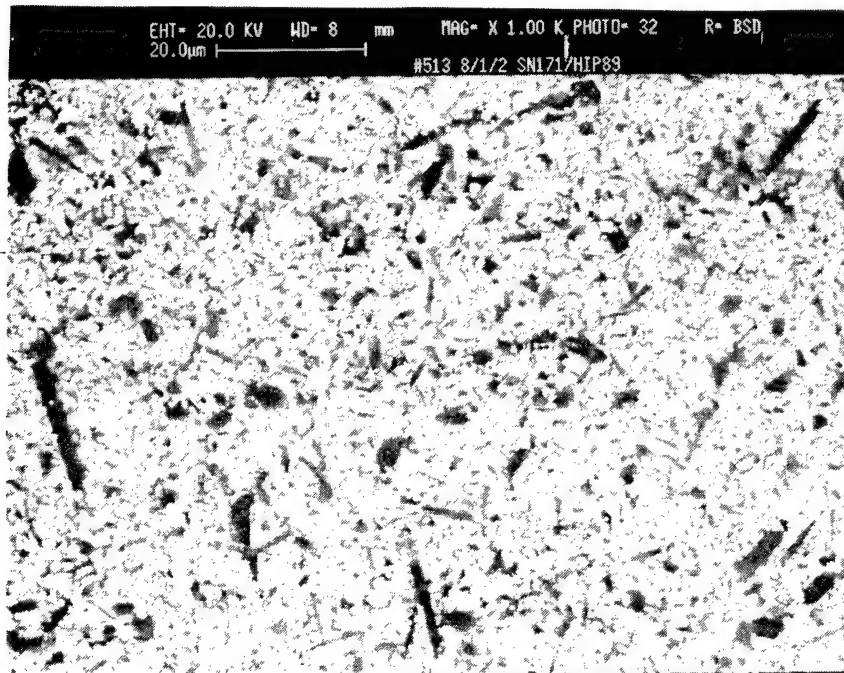


**Figure 3.25.** BSE micrograph of HIPed 8/1/2.

**Table 3.32 – Physical and Mechanical Properties for Sinter-DOE After HIPing**

Composition	HIPed Density g/cc	Percent of Theoretical	Knoop Hardness kg/mm <sup>2</sup>	Fracture Toughness MPa√m
6/3/2	3.289	100	1309	5.20
8/2/2	3.310	99.9	1356	5.39
8/1/2	3.309	100	1408	5.35
5/2/3	3.258	99.2	1292	5.64
6/3	3.270	100	1480	5.45
4/7/1	3.235	99.8	1405	5.03
4/4/1/3	3.248	100	1453	5.21

### **3.8.1.5 Phase Identification and Chemical Analysis**

As shown in the BSE images of the sintered materials, the intergranular phase, or sometimes referred to as the secondary phase, surrounds all silicon nitride grains uniformly. XRD was used to determine the type of intergranular phase, as detailed in Table 3.33. These results show that the Al<sub>2</sub>O<sub>3</sub> content determines the nature of the intergranular phase, e.g., amorphous or crystalline. The materials with Al<sub>2</sub>O<sub>3</sub> contents greater than 2.5 weight percent, such as 6/3/2, 6/3, 4/7/1 and 4/4/1/3, form amorphous intergranular phases. Whereas, the materials with lower Al<sub>2</sub>O<sub>3</sub> contents develop crystalline intergranular phase(s). For example, both the 8/2/2 and 8/1/2 materials formed the Y<sub>10</sub>Si<sub>6</sub>N<sub>2</sub>O<sub>24</sub> oxynitride as the intergranular phase and the 5/2/3 material yielded a mixed oxynitride/oxide secondary phase.

All chemical analysis results are also tabulated in Table 3.33. Generally, the overall chemistries of the processed materials are directly determined by the initial material composition, as expected. These results confirm compositional control during processing.

Table 3.33 – X-ray Diffraction and Chemical Analysis Results for First Set of HIPed Materials

Composition	Ceramic 2nd Phase(s)	Lattice Parameter		Chemical Analysis								K <sub>IC</sub> MPa√m	HIPed Density	
		a (Å)	c (Å)	Fe w/o	Y w/o	Al w/o	Ti w/o	O w/o	Si w/o	N w/o	H <sub>KV</sub> Kg/mm <sup>2</sup>		g/cc	%
6/3/2	Glass	7.609	2.915	0.17	4.65	1.54	1.15	3.46	52.84	36.12	1309	5.20	3.289	100
8/2/2	Y <sub>10</sub> Si <sub>4</sub> N <sub>2</sub> O <sub>24</sub>	7.592	2.905	0.21	5.88	1.12	1.18	3.51	53.62	34.45	1356	5.39	3.310	99.9
8/1/2	Y <sub>10</sub> Si <sub>4</sub> N <sub>2</sub> O <sub>24</sub>	7.589	2.907	0.60	6.11	0.77	1.19	3.33	52.51	35.41	1408	5.35	3.309	100
5/2/3	Y <sub>10</sub> Si <sub>4</sub> N <sub>2</sub> O <sub>24</sub> + Y <sub>2</sub> SiO <sub>6</sub>	7.585	2.906	0.58	6.08	0.77	1.18	3.39	52.08	35.86	1292	5.64	3.258	99.2
4/7/1	Glass	7.592	2.908	0.20	2.83	3.33	0.56	4.17	52.73	36.15	1405	5.03	3.235	99.8
4/4/1/3	Glass	7.591	2.909	0.36	2.99	3.67	0.59	3.56	52.85	35.95	1453	5.21	3.248	100
6/3	Glass	7.596	2.906	0.30	4.21	1.61	0.06	3.00	54.37	36.40	1480	5.45	3.270	100

The silicon nitride phase in all instances was of the  $\beta$  phase; that is, no  $\alpha$ - $\text{Si}_3\text{N}_4$  was detected. Additionally, all lattice parameters were calculated to determine  $\text{Al}_2\text{O}_3$  solubility (solid solution). Results indicate that solid solution did not occur and therefore Sialon was not formed. These observations were true for all materials, even those containing relatively high  $\text{Al}_2\text{O}_3$  contents.

### **3.8.2 First DOE for HIPing**

After these preliminary trials of the HIP process, a first HIP DOE was engineered to explore the effects of starting density, temperature, and pressure on the properties and microstructures of the HIP-processed materials. This DOE is shown in Table 3.34. The experimental design included four sintering runs and two HIPing runs. Sintering was conducted at  $1700^\circ\text{C}$  in inert gas at various time increments to produce samples of different densities. Thereafter, two HIPing treatments were tried, and the results were analyzed.

One HIP treatment included a pressure of 10,000 psi and a cycle temperature of  $1775^\circ\text{C}$ , whereas, the other treatment consisted of a temperature at  $1850^\circ\text{C}$  and pressure at 5000 psi. This DOE also provided input for establishing HIP process parameters and providing a technique to systematically move each composition toward its optimum processing conditions.

**Table 3.34 – DOE HIP**

Conditions	Sinter Time @ 1700°C (Hrs)	HIP Temperature (°C)	HIP Pressure psi
1	2	1850	5000
2	6	1850	5000
3	10	1850	5000
4	14	1850	5000
5	2	1775	10,000
6	6	1775	10,000
7	10	1775	10,000
8	14	1775	10,000

#### **3.8.2.1 Sintering Kinetics**

The resulting sintered densities as a function of sintering time are presented in Figure 3.29. These data show that the sintering kinetics or efficiency are strongly influenced, as expected, by composition. For example, materials with relatively low  $\text{Al}_2\text{O}_3$  content, such as 8/1/2 and 5/2/3 exhibit slower sintering rates. In general, densification of  $\text{Si}_3\text{N}_4$  depends upon the quantity and viscosity of the liquid phase during sintering. Smaller amounts of additives and/or  $\text{Al}_2\text{O}_3$  result in slower sintering kinetics.

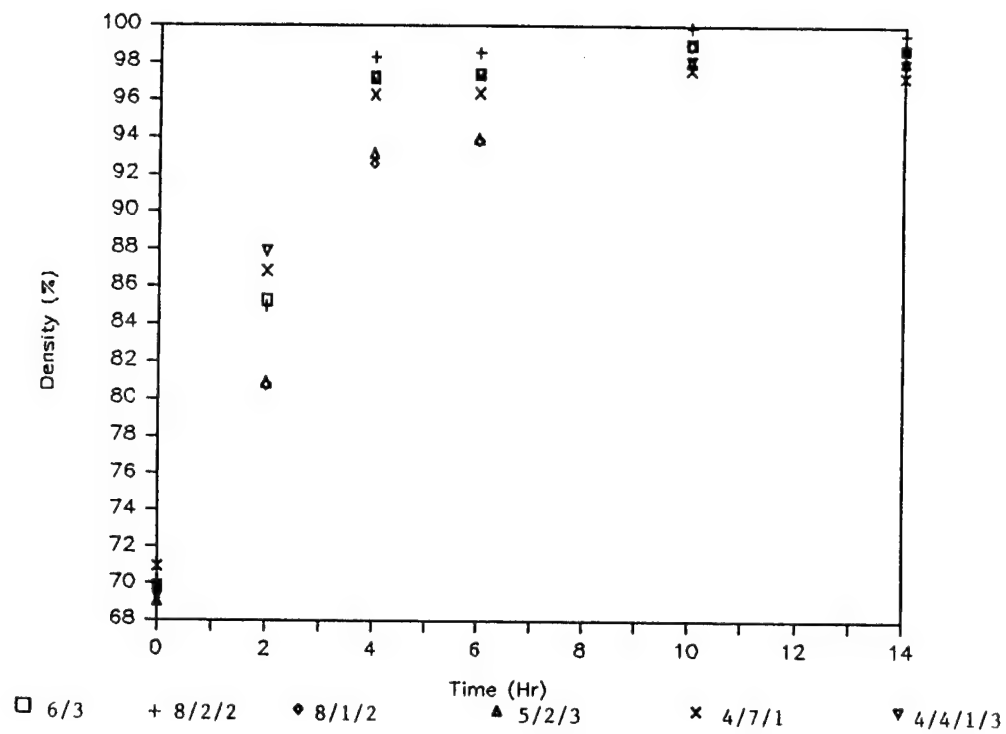


**Figure 3.29** Sintered density vs. sintering time at 1700°C in inert gas for various program compositions.



### 3.8.2.2 HIPed Density

Figures 3.30 and 3.31 show the densities after HIPing at 1850 and 1775°C, respectively, as a function of sintering density for the samples as identified. Only the results obtained with sintered sample densities exceeding 90 percent of theoretical density (TD) are included in Figures 3.30 and 3.31. The straight line in both figures represents a "no change" in density due to HIP treatment. That is, points below this line would indicate a density decrease due to HIPing. In each instance the HIP treatment increased the density of all materials. Only a few of the materials, however, yielded densities higher than 99.8 percent of TD. Furthermore, the threshold sintering density could not be discerned from these results.

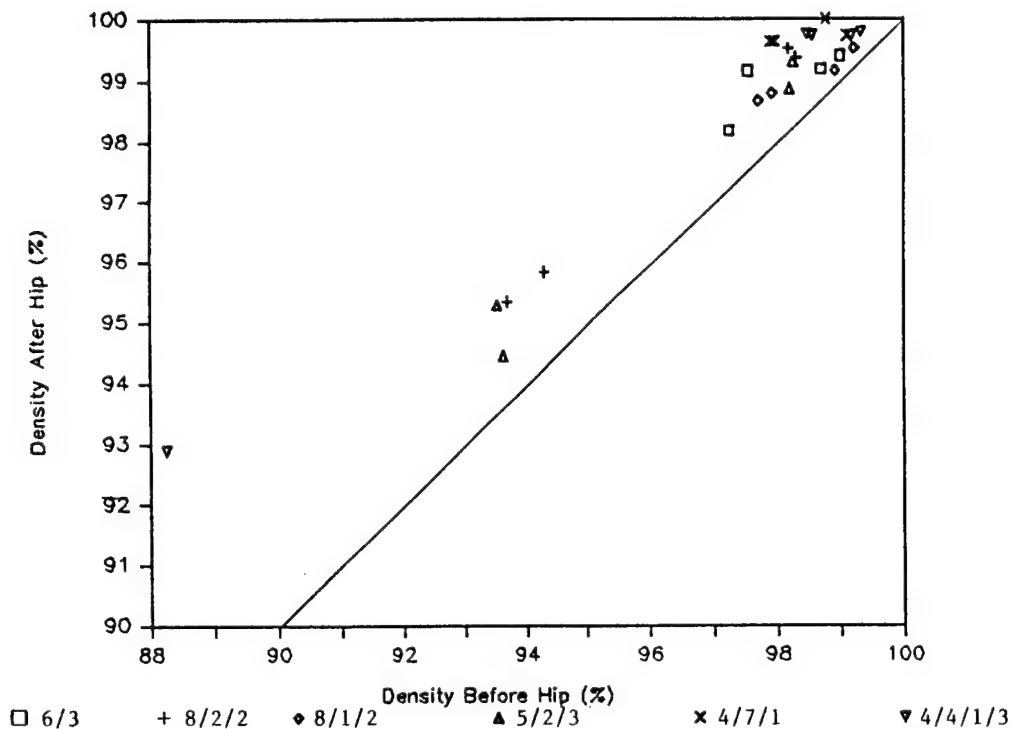


**Figure 3.30.** Relative densities of varying  $\text{Si}_3\text{N}_4$  compositions after HIPing at 1850°C as a function of those before HIPing.

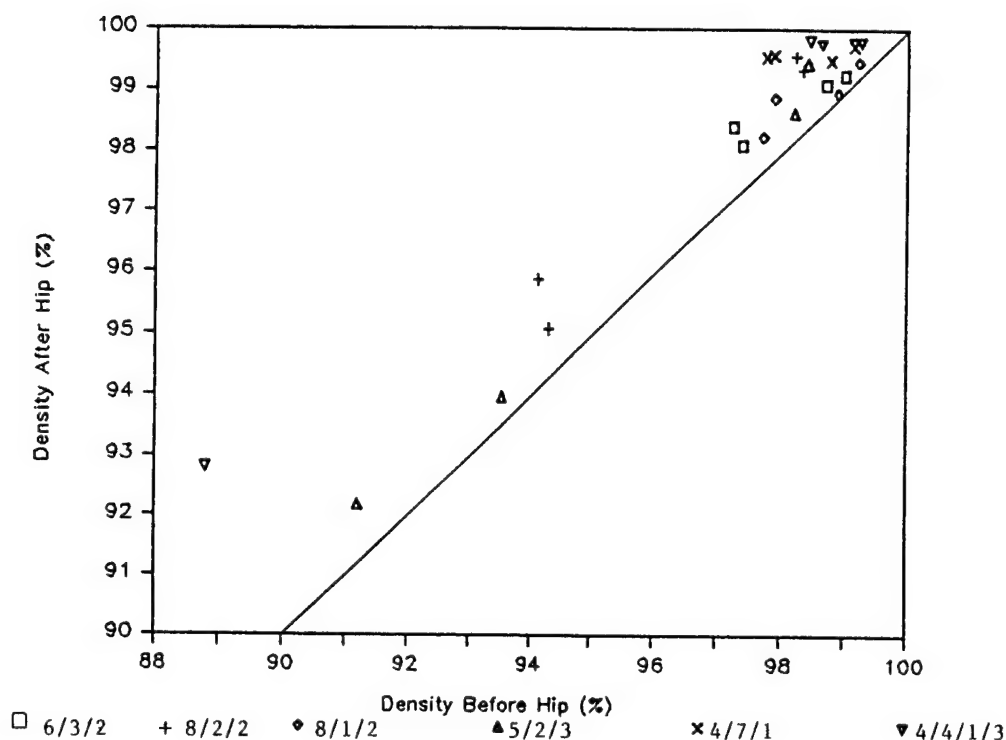


**Figure 3.31.** Relative densities of varying  $\text{Si}_3\text{N}_4$  compositions after HIPing at  $1750^\circ\text{C}$  as a function of those before HIPing.

### 3.8.2.3 Microstructures

During these HIP runs, an unusual white fibrous residue formed on the surface of all specimens. The fibrous deposits from several samples were removed and studied by chemical analysis. Spectroscopy results, as given in Table 3.35, show that the fibrous material is a silicon based compound. Diffraction results (Figure 3.32) show that the fibers are crystalline and are made up of both  $\alpha$ - and  $\beta$ - $\text{Si}_3\text{N}_4$ . The  $\alpha$ : $\beta$  ratio for the fibers was estimated to be approximately 2:3 and orientation along (110) planes was preferred. Small amounts of crystalline  $\text{SiO}_2$  (cristobalite) were also detected as shown in Figure 3.32.

The mechanism for the observed fiber formation is not completely known; however, condensation of volatile species associated with the HIP furnace is suspected.

**Table 3.35 – Quantitative Analysis of the Fibrous Residues in HIPing**

Element	Wt %
Si	42.24
Y	0.02
Al	1.31
Ti	0.01
Fe	0.07
Cr	0.02
Ni	0.01
Na	0.06
K	< 0.01
W	< 0.01

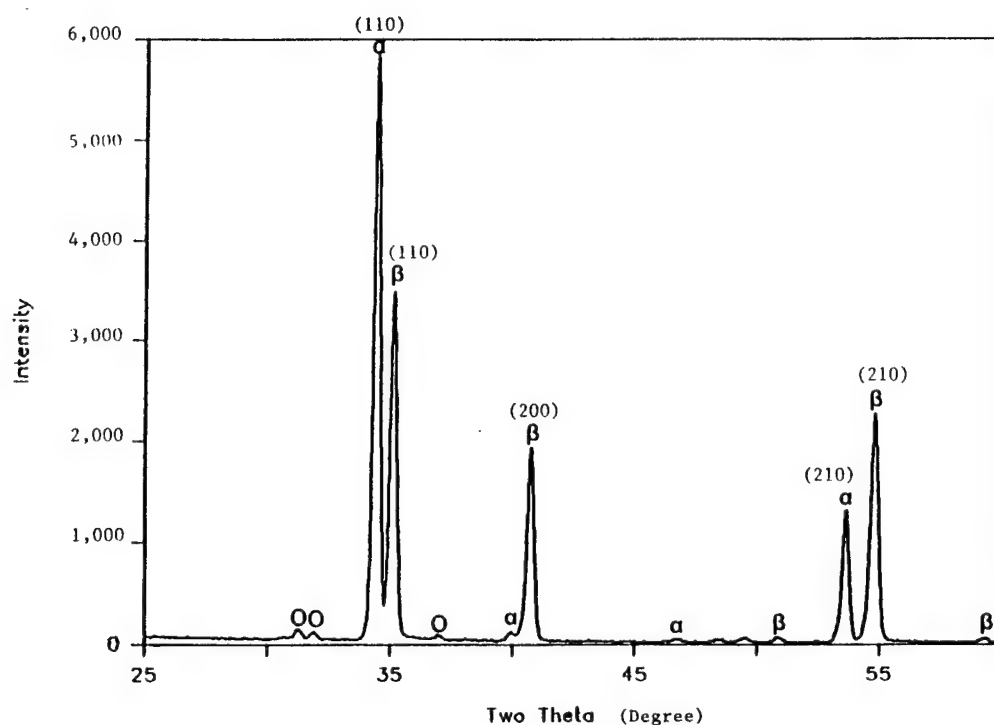


**Figure 3.32** XRD on the fibrous residues in HIPing using Cr  $K\alpha$ -2 radiation.  $\alpha$ :  $\alpha$ - $Si_3N_4$ ;  $\beta$ :  $\beta$ - $Si_3N_4$ ; O:  $SiO_2$

All HIP DOE No. 1 specimens were prepared for optical microscopy by cross-sectioning, mounting and polishing. The examination showed microporosity present in all samples except the 4/4/1/3 composition. The microporosity in some samples was mainly confined to the outer regions of the specimen. In other samples, the microporosity appeared uniform

throughout and yet in still other samples, the porosity clustered to form visible marbling patterns. The type and volume percent of the residual porosity appeared to be primarily determined by material compositions and not by the HIP run. To demonstrate, the microstructures of selected compositions were examined by SEM using BSE imaging. Figures 3.33 and 3.34 are micrographs of the same compositions HIPed under the two different DOE conditions. As noted, the amount of microporosity is the same for both materials.

#### **3.8.2.4     *Hardness and Fracture Toughness***

The hardness and fracture toughness for all samples was also measured and the data are presented in Table 3.36. Analysis of the data shows that the HIP run conditions, specifically the processing temperature, did not influence the toughness. The hardness appears to be slightly greater with lower HIPing temperature. Again, composition strongly influences the properties as well as the sintering efficiency (as measured by residual porosity). For example, the 4/4/1/3 materials appear, on a relative basis, the hardest, whereas the high-oxygen-containing materials such as 4/7/1 have the lowest fracture toughness.

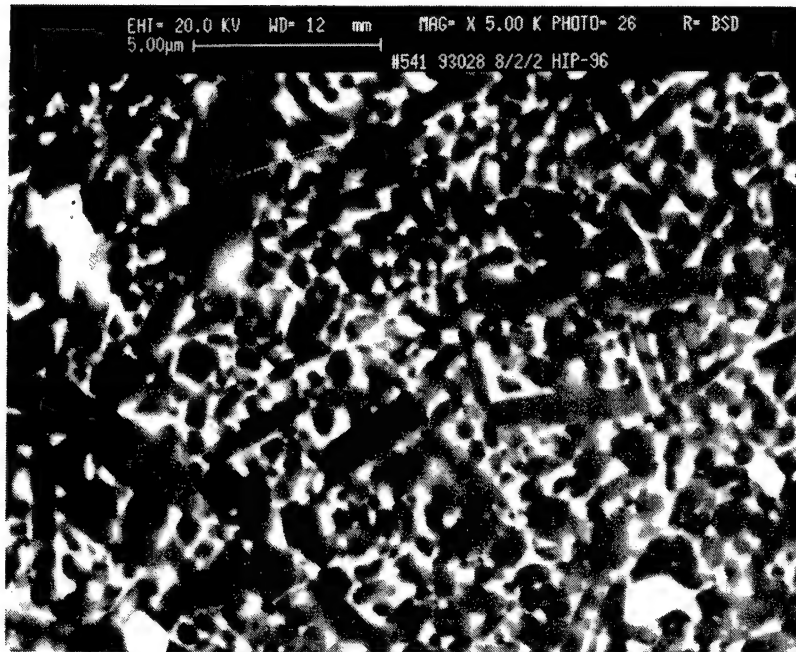


**Figure 3.33** SEM/BSE micrograph of 8/2/2  $\text{Si}_3\text{N}_4$  HIPed at 1850°C.

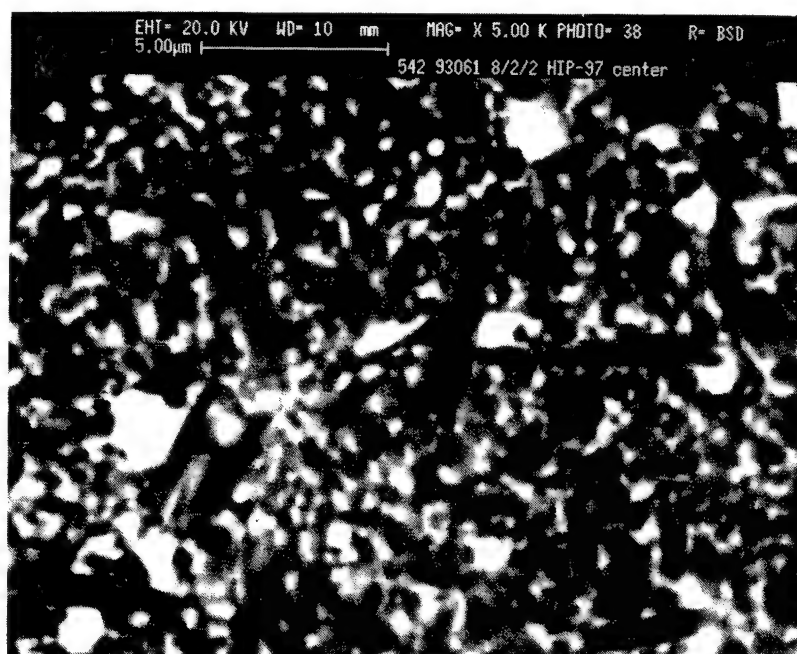


**Figure 3.34** SEM/BSE micrograph of 8/2/2  $\text{Si}_3\text{N}_4$  HIPed at 1775°C.

**Table 3.36 – Density, Hardness and Toughness of HIPed  $\text{Si}_3\text{N}_4$  from Two Different HIP Runs.**

	1850°C 5,000 psi			1775°C 5,000 psi		
Composition	Density g/cm <sup>3</sup>	Hardness kg/mm <sup>2</sup>	Toughness MPa√m	Density g/cm <sup>3</sup>	Hardness kg/mm <sup>2</sup>	Toughness MPa√m
6/3/2	3.270 (99.4%)	1351	5.12	3.265 (99.2%)	1407	5.03
8/2/2	3.268 (98.6%)	1417	5.31	3.269 (98.7%)	1396	5.21
3/1/2	3.297 (99.6%)	1328	5.03	3.295 (99.5%)	1337	5.07
5/2/3	3.287 (99.4%)	1342	5.00	3.291 (99.5%)	1408	5.06
4/7/1	3.231 (99.7%)	1322	4.67	3.231 (99.7%)	1401	4.93
4/4/1/3	3.243 (99.8%)	1425	5.26	3.243 (99.8%)	1471	5.20
6/3	3.255 (99.5%)	1406	5.52	3.250 (99.4%)	1420	5.42
Class II Minimum Requirement		1480	5.0		1480	5.0

### **3.8.3 Evaluation of Furnace Environment**

As described in the previous section, silicon nitride whiskers formed on the sample surface in both HIP runs at 1775°C (3227°F) and 1850°C (3362°F) for the first HIP DOE. This kind of surface whisker formation had not been observed before. Another HIP run (A) was conducted using Cercom's standard PSG-H cycle at an intermediate temperature of 1825°C (3317°F). The surface fiber formation was once again evidenced. This fiber formation is atypical, and was suspected to be related to a contaminated hot zone and/or insulating materials in the HIP.

To verify this hypothesis, an identical cycle (Run B) was conducted in another HIP furnace. The HIP contractor was changed from Gorham Advanced Materials to ABB Autoclave Systems. HIP run B at ABB produced specimens with a clean surface, without any surface fiber formation. The second ABB HIP run (C), using the same cycle, was conducted to verify this observation. Results confirmed that fiber formation is related to the HIP furnace environment. The specimens from these three HIP runs (A, B, and C) were characterized to further evaluate the cause and effect of the furnace environments to microstructure, hardness, and toughness.

#### **3.8.3.1 Microstructural Evaluation**

Samples from all three HIP runs were cross-sectioned, mounted and polished for microstructural evaluation. Optically, almost all samples contained evidence of near-surface porosity. Under low magnification this feature appears as whitish streamers radiating outward from the core of the sample. The degree or extent of near surface porosity appears to be strongly related to material composition. Table 3.37 attempts to quantify the near-surface porosity by tabulating the depth and approximate affected area for each composition. Measured density and calculated percent of theoretical density are also given in Table 3.37. As shown, only the 4/4/1/3 composition produces a microstructure without near-surface porosity.

A complete microstructural analysis was conducted optically (bright field) on all polished samples at 100X to 200X. The visible microstructural features in this magnification range are inclusions, porosity and intergranular phases (for this discussion porosity will be considered a phase.) These features are systematically addressed using specified routines and, thereafter, assigned ratings.



**Table 3.37 – Near-Surface Microporosity for HIPed Si<sub>3</sub>N<sub>4</sub> (0.50 inch Diameter Balls) with Constant Conditions of 1825°C (3317°F) and 34 MPa (5,000 psi), but Varying Compositions and Equipment (Gorham, ABB).**

Composition	HIP Cycle	HIPed g/cm <sup>3</sup>	Density	Maximum Depth of microporosity	Approximated area of microporosity
6/3/2	A	3.264	(99.2%)	0.10"	40%
8/2/2	A	3.286	(99.2%)	0.25"	80%
8/1/2	A	3.279	(99.1%)	0.15"	50%
5/2/3	A	3.251	(99.0%)	0.25"	90%
6/3/2	B	3.273	(99.5%)	0.20"	50%
8/2/2	B	3.300	(99.6%)	0.15"	40%
8/1/2	B	3.306	(99.9%)	0.10"	30%
5/2/3	B	3.275	(99.7%)	0.08"	10%
4/7/1	B	3.232	(99.8%)	0	40%
4/4/1/3	B	3.246	(99.9%)	0	0%
6/3	B	3.270	(100.0%)	–	0%
6/3/2	C	3.254	(98.9%)	0.10"	30%
8/2/2	C	3.279	(99.0%)	0.08"	20%
8/1/2	C	3.261	(98.5%)	0.05"	20%
5/2/3	C	3.241	(98.7%)	0.10"	10%
4/7/1	C	3.202	(98.8%)	0.15"	40%
4/4/1/3	C	3.225	(99.2%)	0	0%
6/3	C	3.228	(98.7%)	0	0%

A = Gorham

B & C = ABB

### 3.8.3.2 Characterization of Microstructure

A classification system for characterizing microstructures was adopted from information provided by a major bearing manufacturer. This classification system is described in Appendix B. The system was applied to all HIPed samples from runs A, B and C. The assessment was performed only on the portion of the samples that did not contain near-surface porosity. Near-surface porosity was considered a distinctly separate feature related to processing and not representative of the intrinsic microstructure. The results of the microstructural assessment are given in Table 3.38. The data show

that all materials are essentially pore-free. The ceramic second phase content varied among the compositions and had the strongest influence on Class determination. Figure 3.35 is a Class I microstructure typical of the 4/4/1/3 composition. Figures 3.36 and 3.37 are two variations of Class II microstructures. As shown, the major difference is the overall metallic-phase content and is directly related to initial  $\text{TiO}_2$  additions.

**Table 3.38 – Microstructure Assessment of HIPed  $\text{Si}_3\text{N}_4$ ,  
(away from near-surface porosity zone).**

Composition	HIP cycle	Porosity	Metallic Phase	Ceramic Phase	Class
6/3/2	A	A02	A06	A08	II
8/2/2	A	A02	A04	A08	II
8/1/2	A	A02	A04	A08	II
5/2/3	A	A02	A06	A08	II
6/3/2	B	A02	A04	A08	II
8/2/2	B	A02	A04	A08	II
8/1/2	B	A02	A06	A08	II
5/2/3	B	A02	A06	A08	II
4/7/1	B	A02	A04	A08	II
4/4/1/3	B	A02	A04	A04	I
6/3	B	A02	A04	A04	I
6/3/2	C	A02	A06	A08	II
8/2/2	C	A02	A04	A08	II
8/1/2	C	A02	A04	A08	II
5/2/3	C	A02	A08	A08	II
4/7/1	C	A02	A04	A08	II
4/4/1/3	C	A02	A04	A04	I
6/3	C	A02	A04	A06	I
Class I		A02	A06	A06	
Class II		A04	A08	A08	
Class III		A04	A08	A08	

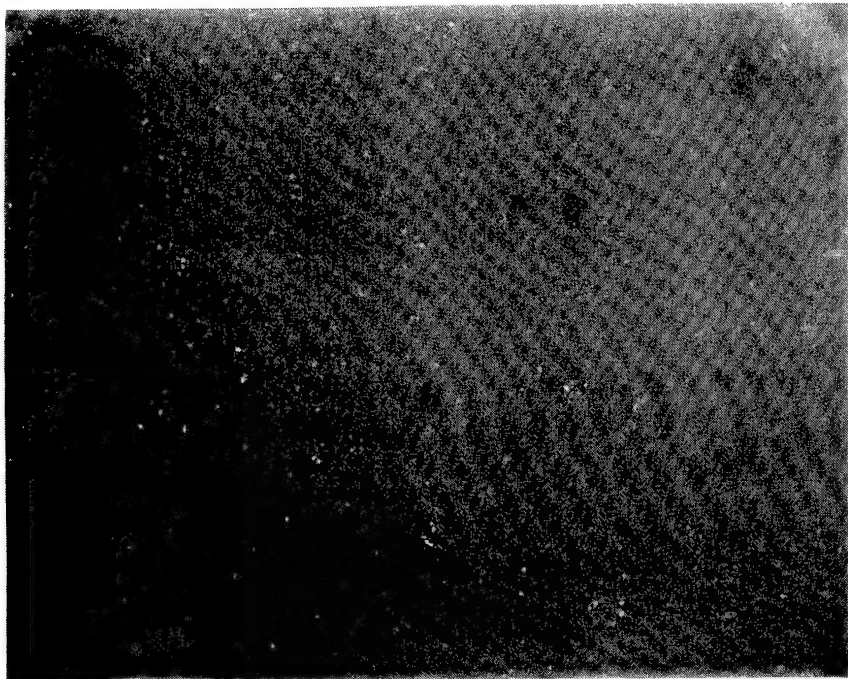


**Figure 3.35.** *Micrograph of 4/4/1/3 from HIP Run C at 200X showing Class I microstructure.*

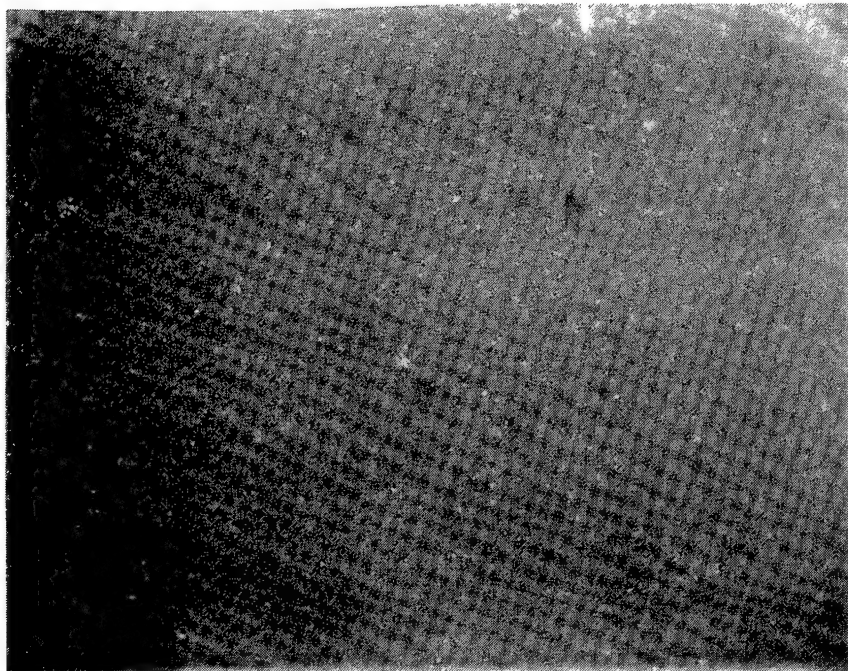


**Figure 3.36.** *Micrograph of 8/1/2 from HIP Run C at 200X showing Class II microstructure with low metallic phase content.*

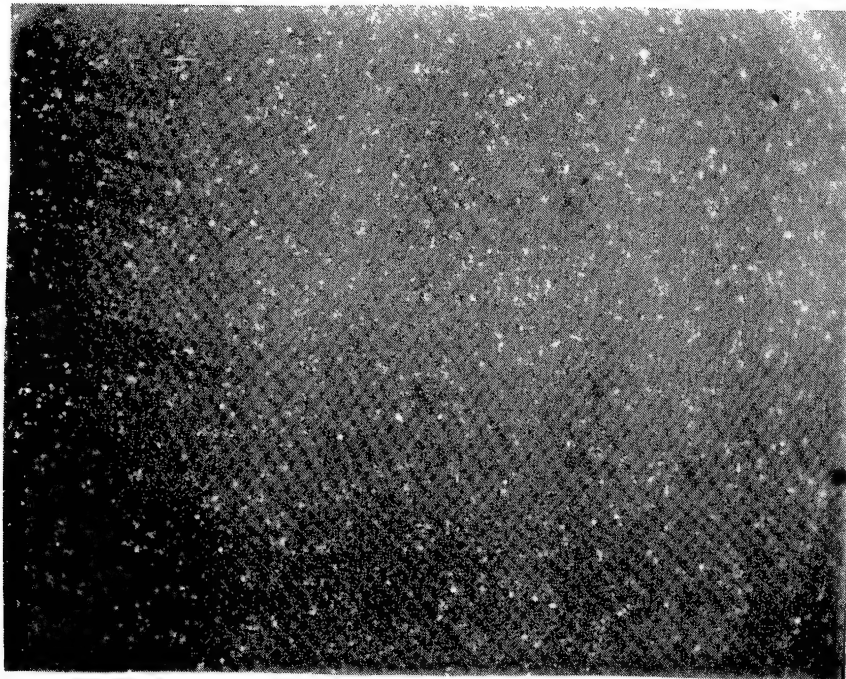


**Figure 3.37.** *Micrograph of 5/2/3 from HIP Run C at 200X showing Class II microstructure with high metallic-phase content.*

#### **3.8.3.3     *Hardness and Toughness***

The hardness and toughness for each material is tabulated in Table 3.39. Results again suggest a strong compositional influence and only the 4/4/1/3 material earns a Class II rating (Figure 3.38 graphically illustrates these results).-

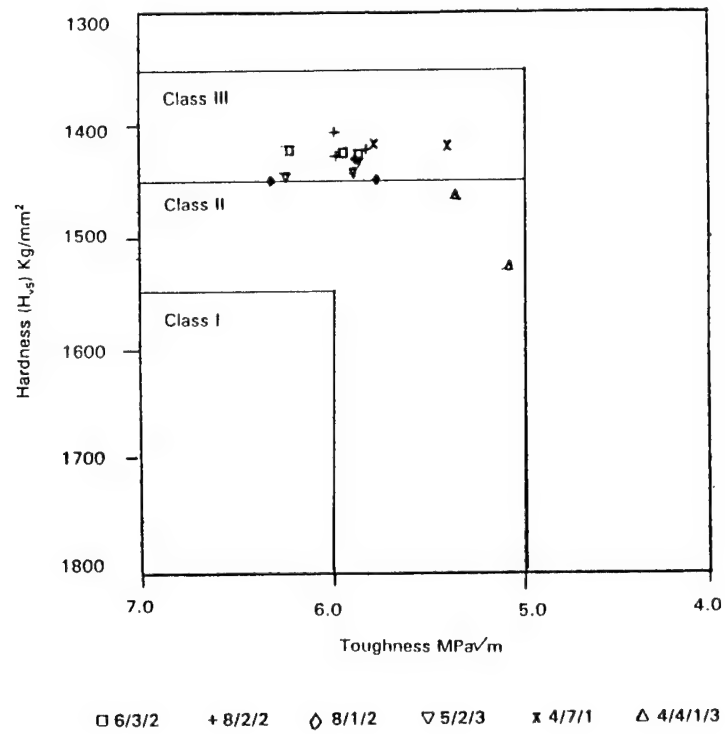


**Figure 3.38.** Microhardness and fracture toughness requirement.

**Table 3.39 – Hardness and Toughness of HIPed Si<sub>3</sub>N<sub>4</sub>.**

Composition	HIP cycle *	H <sub>V5</sub> Kg/mm <sup>2</sup>	K <sub>IC</sub> MPa√m	Class
6/3/2	A	1426	5.85	III
8/2/2	A	1427	5.97	III
8/1/2	A	1448	5.76	III
5/2/3	A	1432	5.85	III
6/3/2	B	1424	5.93	III
8/2/2	B	1405	5.98	III
8/1/2	B	1449	6.31	III
5/2/3	B	1442	5.88	III
4/7/1	B	1418	5.38	III
4/4/1/3	B	1460	5.34	II
6/3	B	1461	6.34	II
6/3/2	C	1422	6.21	III
8/2/2	C	1421	5.81	III
8/1/2	C	1430	5.87	III
5/2/3	C	1446	6.23	III
4/7/1	C	1416	5.77	III
4/4/1/3	C	1526	5.06	II
6/3	C	1426	6.26	II
Class I		1550	6.0	
Class II		1450	5.0	
Class III		1350	5.0	

\* 'A' cycle conducted at Gorham, Cycle B & C at ABB

#### 3.8.3.4 Chemical and Crystallographic Analysis

For the purpose of studying the chemical changes that occur during processing, six material compositions were processed through pre- and full nitriding, sintering, and HIPing. The chemistry and phase distributions of the materials were extensively characterized using atomic emission spectroscopy and x-ray diffraction. The analyses were performed on materials having completed various steps in the process sequence. Table 3.40 lists the results of the chemical analysis of each composition through prenitriding, full nitriding, sintering and HIPing. The concentration of the nitriding catalyst, Fe, remained constant throughout the process. All other cations, such as Y, Al

and Ti, also maintained a consistent concentration. Similarly, the oxygen content of the blanks did not vary during processing, as shown in Figure 3.39.

**Table 3.40 - Chemical Analysis of Materials Following Each Processing Step**

Full Nitride						
Compo- sition	6/3/2	8/2/2	8/1/2	5/2/3	4/7/1	4/4/1/3
Y w/o	2.44	3.96	3.09	2.38	2.11	1.62
Al w/o	1.65	1.17	0.68	1.14	3.82	4.05
Ti w/o	1.23	1.17	1.15	1.72	0.62	0.65
Fe w/o	0.20	0.20	0.20	0.20	0.21	0.21
Si w/o	53.48	53.07	54.78	54.52	54.74	54.29
O w/o	4.01	3.96	3.68	3.74	4.90	4.15
N w/o	36.99	36.47	36.41	36.29	33.54	34.99
Sinter						
Compo- sition	6/3/2	8/2/2	8/1/2	5/2/3	4/7/1	4/4/1/3
Y w/o	2.34	1.30	2.60	2.23	0.83	1.26
Al w/o	1.69	1.27	0.73	1.20	3.95	4.05
Ti w/o	1.27	1.29	1.20	1.79	0.66	0.64
Fe w/o	0.32	0.26	0.24	0.22	0.23	0.21
Si w/o	52.82	55.63	54.42	54.72	55.84	55.67
O w/o	4.28	4.14	3.88	3.64	4.64	3.86
N w/o	37.27	36.07	36.91	37.17	33.82	34.29
						6.93
						61.60
HIP						
Compo- sition	6/3/2	8/2/2	8/1/2	5/2/3	4/7/1	4/4/1/3
Y w/o	1.20	1.14	0.99	1.21	1.05	1.36
Al w/o	1.10	1.05	0.65	1.12	3.48	3.80
Ti w/o	0.85	1.07	1.20	1.81	0.57	0.61
Fe w/o	0.22	0.22	0.22	0.23	0.20	0.22
Si w/o	57.58	57.51	58.75	57.36	55.71	55.90
O w/o	4.73	4.35	4.09	3.66	5.28	3.98
N w/o	33.23	34.57	34.08	34.54	33.70	34.11

Results indicate that there was a nitrogen loss in HIPing for the 6/3/2, 8/2/2, 8/1/2 and 5/2/3 compositions. This effect is plotted in Figure 3.40. The theoretical N/Si ratio for  $\text{Si}_3\text{N}_4$  is 66.5%. The overall N/Si ratio is determined by the nitrogen content in the intergranular phase. The nitrogen loss may be attributed to either the  $\text{Si}_3\text{N}_4$  decomposition or to nitrogen's diffusing out through the intergranular phase. Nevertheless, there was no significant

weight loss in the parts. Silicon metal was not observed on either the parts or in the graphite crucible. Extensive near-surface microporosity was observed in these four compositions. The 4/4/1/3 composition did not show nitrogen loss nor near-surface microporosity. The preliminary assumption was that the nitrogen loss was the result of nitrogen outgassing through the intergranular phase.

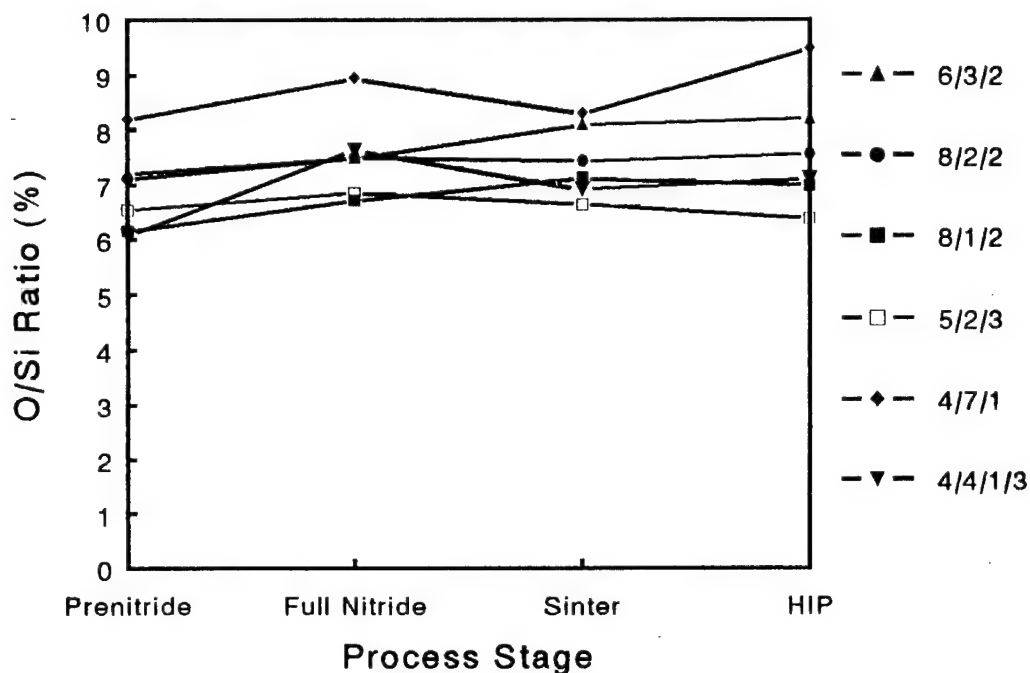


**Figure 3.39** - The O/Si ratio in  $\text{Si}_3\text{N}_4$  after each processing step

The intergranular phase was characterized using x-ray diffraction. The type of yttrium silicate intergranular phase was seen to change during processing. Also, there was an unknown phase, which was labeled as "?" in Table 3.41. It is thought to be a compound in the  $\text{Si}_3\text{N}_4\text{-Al}_2\text{O}_3\text{-SiO}_2\text{-AlN}$  phase diagram.

It was observed that there was a large amount of  $\beta\text{-Si}_3\text{N}_4$  formed after full nitride, as seen in Table 3.42. The formation of the  $\beta\text{-Si}_3\text{N}_4$  was always related to the presence of a liquid phase. It was also noticed that the higher



the aluminum and oxygen contents in the system, the higher the amounts of  $\beta$ - $\text{Si}_3\text{N}_4$  that were formed, as shown in Figures 3.40 and 3.41. Figure 3.40 shows a particularly striking relationship between aluminum content and fraction of  $\alpha$  phase. It demonstrates that as the Al/Si ratio varies from 1.5% to 7%, the  $\alpha/\beta$  ratio goes from 100% to 0%, and this relationship exhibits very little scatter about an empirically-fitted, exponential decay function. Neither 4/7/1 nor the 4/1/3 compositions contained  $\alpha$ - $\text{Si}_3\text{N}_4$  after nitride. The  $\alpha$ - $\beta$  transformation and solution-precipitation mechanism should not be available in the subsequent sintering process. However, results showed that both 4/7/1 and 4/4/1/3 can be densified to full density through pressureless sintering and HIPing.

**Table 3.41 — Intergranular Phase Identification**

	HIP 1825°C 5000 psi	Sinter 1700°C	Full-Nitride
6/3/2	Amorphous, TiN	Amorphous, TiN	TiN, $\text{Y}_{10}\text{Si}_6\text{N}_2\text{O}_{24}$ , $\text{Y}_2\text{SiO}_5$
8/2/2	Amorphous, TiN	TiN, $\text{Y}_{10}\text{Si}_6\text{N}_2\text{O}_{24}$ , $\text{Y}_2\text{SiO}_5$	TiN, $\text{Y}_{10}\text{Si}_6\text{N}_2\text{O}_{24}$
8/1/2	TiN, $\text{Y}_2\text{Si}_3\text{O}_3\text{N}_4$ ?	TiN, $\text{Y}_2\text{SiO}_5$ , $\text{Y}_{10}\text{Si}_6\text{N}_2\text{O}_{24}$	TiN, $\text{Y}_{10}\text{Si}_6\text{N}_2\text{O}_{24}$
5/2/3	TiN ?	Amorphous, TiN	TiN, $\text{Y}_{10}\text{Si}_6\text{N}_2\text{O}_{24}$ , $\text{Y}_2\text{SiO}_5$
4/7/1	Amorphous, (TiN)	Amorphous, (TiN)	Amorphous, (TiN )
4/4/1/3	Amorphous, (TiN)	(TiN) ?	(TiN) ?

### 3.8.4 Second DOE for HIP Optimization

The first HIP DOE did not show any influence of HIP time, temperature, or pressure on resulting material characteristics. All variations were attributable only to differences in the compositions of the materials. A second Taguchi array of experiments was, therefore, designed and carried out to determine the effects of the HIP parameters. Wider variations in temperature and holding time were used in this second DOE. Four HIP runs were conducted at different temperatures, pressures and holding times. The Taguchi array is outlined in Table 3.43.

**Table 3.43 - Second DOE for HIP Parameters**

#	Temperature °C	Pressure psi	Time min.	Gas
1	1875	5000	75	Ar/N <sub>2</sub>
2	1875	10,000	30	Ar/N <sub>2</sub>
3	1750	10,000	30	Ar/N <sub>2</sub>
4	1750	1500	75	Ar/N <sub>2</sub>

The resulting HIPed densities are presented in Table 3.44. The data show that there was no density variation attributable to these four different HIPing conditions. However, two different types of microporosity, near-surface and volume microporosity, were observed. The near surface microporosity appeared as white streamers, radiating inward to the core of the sample. The volume microporosity was limited to the interior of the sample, and was aligned in a vein-like pattern. The streamer and vein-like patterns can be identified using naked eyes and optical microscopy can only exhibit microporosity within these areas, as shown in Figures 3.43 and 3.44. Table 3.45 summarizes the presence of microporosity. Basically, the amount of microporosity was determined not only by the composition but also by the HIPing conditions.

**Table 3.44 - HIPed Density from Taguchi Experimental Array**

	1875°C 5000 psi 75 min.	1875°C 10,000 psi 30 min.	1750°C 5000 psi 30 min.	1750°C 10,000 psi 75 min.
6/3/2	3.281 (99.73%)	3.292 (100.6%)	3.288 (99.94%)	3.278 (99.64%)
8/2/2	3.309 (99.88%)	3.307 (99.82%)	3.305 (99.76%)	3.306 (99.79%)
8/1/2	3.307 (99.91%)	3.313 (100.09%)	3.302 (99.76%)	3.308 (99.39%)
5/2/3	3.279 (99.85%)	3.280 (99.88%)	3.278 (99.82%)	3.278 (99.82%)
4/7/1	3.235 (99.84%)	3.220 (99.38%)	3.233 (99.78%)	3.227 (99.60%)
4/4/1/3	3.245 (99.84%)	3.249 (99.97%)	3.245 (99.84%)	3.248 (99.94%)
8/2	3.287 (99.76%)	3.291 (99.88%)	3.290 (99.85%)	3.291 (99.885)
6/3	3.267 (99.91%)	3.269 (99.99%)	3.264 (99.82%)	3.270 (100%)

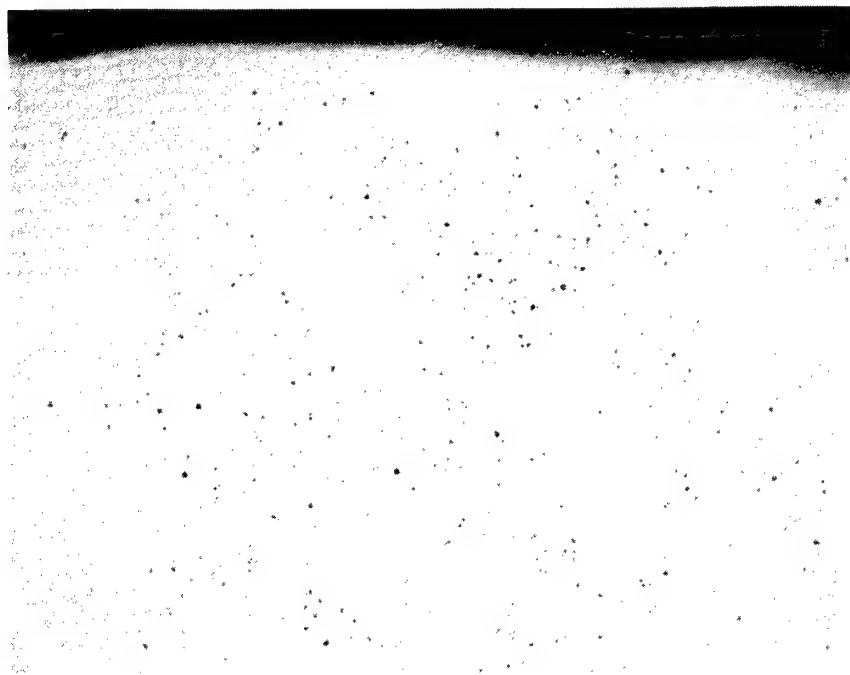


**Figure 3.43** *An optical micrograph of the porosity within one of the white streaks near the surface of the silicon nitride part.*

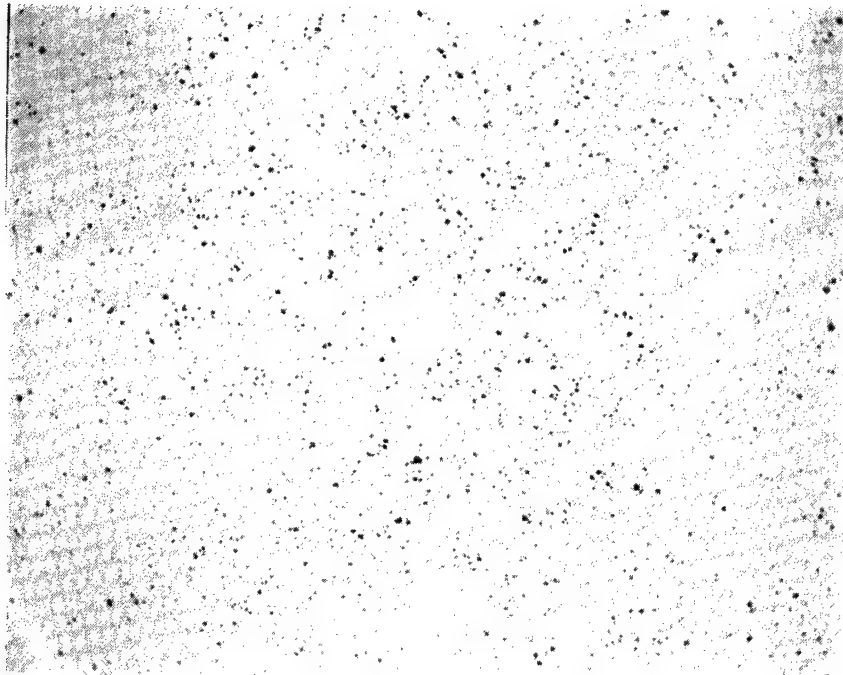


**Figure 3.44** *An optical micrograph of the volume porosity typical within the vein-like areas in certain of the silicon nitride materials.*

**Table 3.45 – Microporosity in HIPed  $\text{Si}_3\text{N}_4$  from Experiment Array**

	1875°C 5,000 psi 75 min.	1875°C 10,000 psi 30 min.	1750°C 5000 psi 30 min.	1750°C 10,000 psi 75 min.
6/3/2	No	No	No	No
8/2/2	No	S	No	No
8/1/2	No	S	No	No
5/2/3	No	V	No	No
4/7/1	No	V	V	V
4/4/1/3	No	No	No	No
8/2	No	No	No	No
6/3	No	No	No	No

S = Near-Surface Porosity

V = Volume Porosity

No = No microporosity

The hardness and toughness are listed in Tables 3.46 and 3.47. Results again suggested a strong compositional influence. Only the 4/4/1/3 material

earned a Class II rating. Every composition had its own optimum condition. The ANOVA was based on the average hardness and toughness to obtain the optimum conditions for the collective of all the compositions. The average response for hardness and toughness on different conditions was shown in Figure 3.45 and 3.46, respectively. The contributions of temperature, pressure and time on both hardness and toughness are listed in Table 3.48. Basically, the best HIPing condition was using high temperature (1875°C) and low pressure (5,000 psi). The soak time at the maximum temperature did not affect either hardness or toughness.

**Table 3.46 - Vickers Hardness of HIPed  $\text{Si}_3\text{N}_4$   
from 2nd HIP Taguchi Array (units in  $\text{kg/mm}^2$ )**

	1875°C 5000 psi 75 min.	1875°C 10,000 psi 30 min.	1750°C 5000 psi 30 min.	1750°C 10,000 psi 75 min.
6/3/2	1425	1403	1414	1400
8/2/2	1384	1391	1411	1400
8/1/2	1433	1414	1416	1411
5/2/3	1402	1419	1422	1408
4/7/1	1419	1366	1395	1344
4/4/1/3	1487	1494	1451	1453
8/2	1427	1414	1401	1408
6/3	1490	1474	1451	1440

**Table 3.47 – Toughness of HIPed Si<sub>3</sub>N<sub>4</sub> from 2nd Taguchi Array  
(units in MPa·m<sup>1/2</sup>)**

	1875°C 5000 psi 75 min.	1875°C 10,000 psi 30 min.	1750°C 5000 psi 30 min.	1750°C 10,000 psi 75 min.
6/3/2	6.44	6.49	6.02	6.11
8/2/2	6.04	5.79	5.98	5.51
8/1/2	6.44	6.13	6.24	5.94
5/2/3	6.61	5.90	5.88	5.78
4/7/1	6.20	5.77	5.85	5.82
4/4/1/3	5.84	5.98	5.17	5.46
8/2	5.66	6.21	5.87	6.00
6/3	6.57	6.47	6.35	6.13

**Table 3.48 – ANOVA Results: Percent Contribution on Hardness and Toughness**

	Percent Contribution on Hardness	Percent Contribution on Toughness
Temperature	57%	87%
Pressure	43%	12%
Time	0%	1%

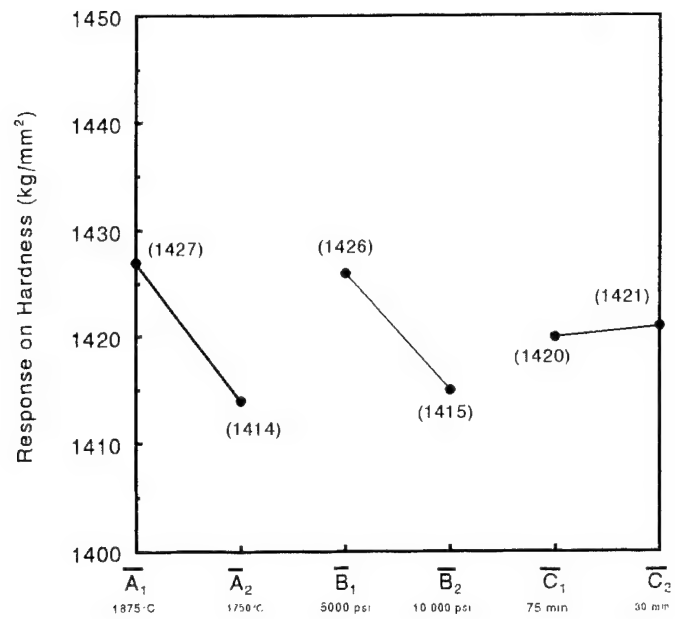


**Figure 3.45-** Average response of hardness to HIP parameters.

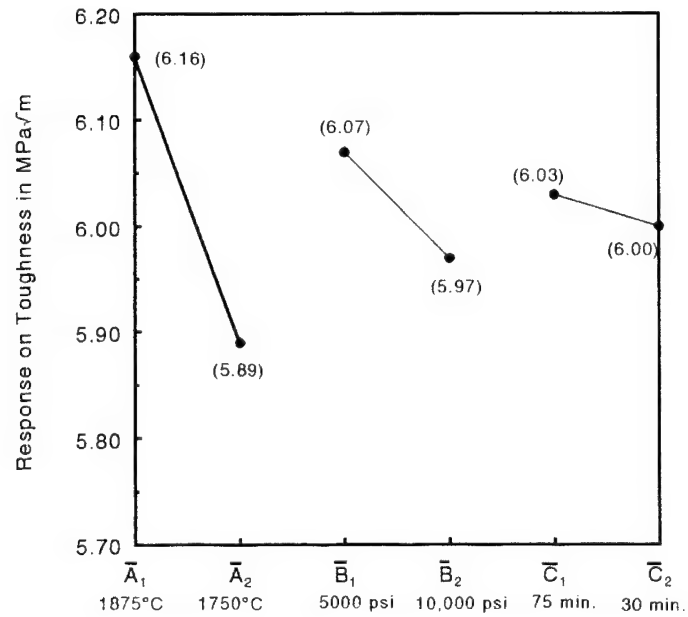


**Figure 3.46** Average response of toughness to HIP parameters.

### **3.8.5 Summary of HIP Optimization Studies**

The results of all the HIPing DOEs were compiled and reviewed. The optimum HIPing cycle was determined to consist of high temperature (1875°C), low pressure (5,000 psi), and short soak time (30 minutes). Nitrogen is detrimental to the graphite furnace; therefore, the nitrogen partial pressure should be kept low to reduce the work in the furnace maintenance. However, the nitrogen partial pressure should be high enough for preventing microporosity.

Results indicate that, as expected, the hardness and toughness are strongly influenced by the composition. The data also show that only the 4/4/1/3 material has consistent Class II characteristics. Therefore, the 4/4/1/3 was down-selected for the program deliverables.



## CHARACTERIZATION OF DELIVERABLE MATERIALS

Using the downselected 4/4/1/3 composition and fabrication process just discussed in Chapter 3.0, a quantity of ball blanks and rolling contact fatigue (RCF) specimen blanks was fabricated as deliverable samples for the program. Additional material was also produced for testing. The program contract required the delivery of 50 ball blanks, 50 RCF blanks, and an unspecified quantity of rejected ball and RCF blanks for comparison. Material produced from the deliverable batch was subjected to mechanical properties testing. Some of the deliverable samples were also inspected by microfocus x-ray computed tomography.

### 4.1 Mechanical Properties

The flexural strength specimens were subjected to a four-point bend test as specified in MIL-1942 using the type B configuration. Twenty-six specimens were tested. The results of the four lowest strength specimens were discarded after machining flaws were found on their surface during SEM examination. The results from the remaining 22 specimens are summarized in Table 4.1, along with hardness and toughness data. The Weibull modulus represents the scatter in the strength values. A Weibull plot of the strength data is presented in Figure 4.1. This plot shows the probability of failure as a function of applied stress. The slope of this line is

the Weibull modulus. A high Weibull modulus indicates that all of specimens broke within a narrow range of applied stresses. High modulus material is more consistent and predictable. Both hardness and fracture toughness of the material were determined using a Vickers microindenter.

**Table 4.1 – Results of Flexural Strength Testing on Deliverable Material**

Average Flexural Strength	135 kpsi (930 MPa)
Characteristic Flexural Strength	146 kpsi (1010 MPa)
Weibull Modulus	14.7
Fracture Toughness	5.60 MPa√m
Vickers Hardness	1485 kg/mm <sup>2</sup>

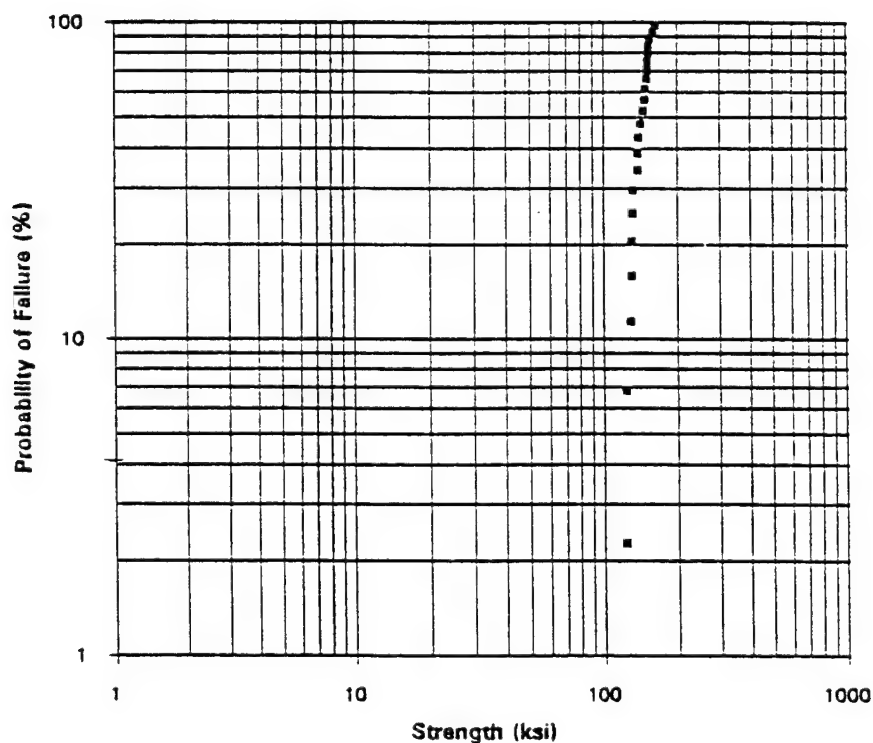


**Figure 4.1** Weibull plot of flexural strength test results on deliverable material.

## 4.2 Microstructure

The finished parts had a uniform, unblemished appearance. The near-surface microporosity evidenced earlier in the program was not observed in these final parts. The microstructure was examined using both optical and electron microscopes. Figure 4.2 is an optical micrograph of a polished, unetched section of the material at a magnification of 200X. The microstructural assessments are summarized in Table 4.2. The assessment procedures are detailed in Appendix B. Figure 4.3 is the SEM micrograph of a polished section. The elongated  $\beta$ -Si<sub>3</sub>N<sub>4</sub> grains were present. Measured grain length ranged between 5 and 15  $\mu$ m. The hardness and toughness were also measured. Basically, the deliverables exhibited Class I microstructure. However, the material only had a Class II rating in terms of hardness and fracture toughness.

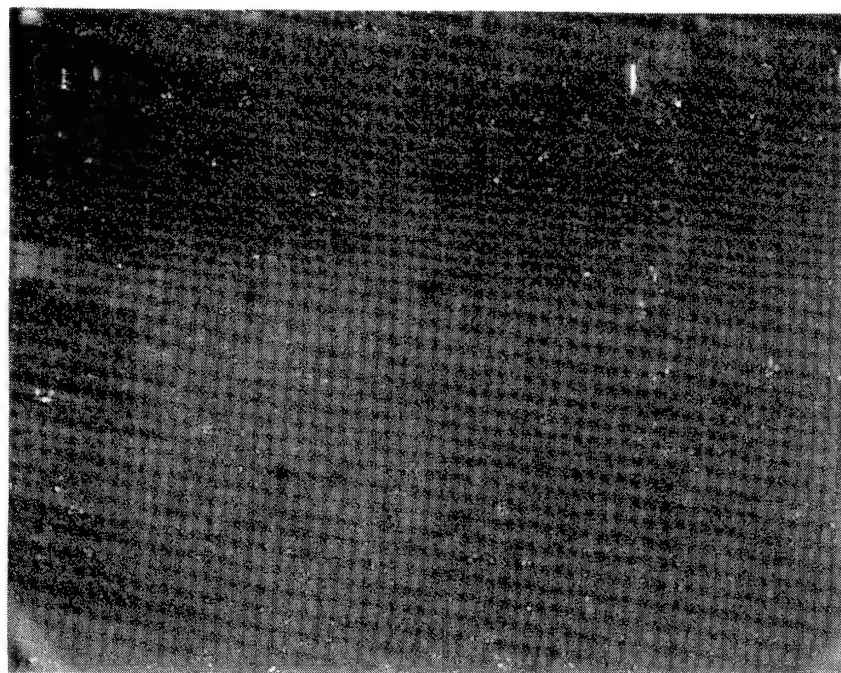


**Figure 4.2** *Optical micrograph of a polished section from a sintered and HIPed silicon nitride ball. Magnified 200 X.*

**Table 4.2 - Microstructure Assessment; Hardness and Toughness of Deliverable 4/4/1/3 HIPed  $\text{Si}_3\text{N}_4$**

Criterion	Parameter	Result	Rating
Microstructure	porosity	PA02	Class I
	metallic phases	MA04	
	ceramic phases	CA04	
Performance	Hardness, $\text{kg/mm}^2$	1484	Class II
	Toughness, $\text{MPa}\sqrt{\text{m}}$	5.60	Class II

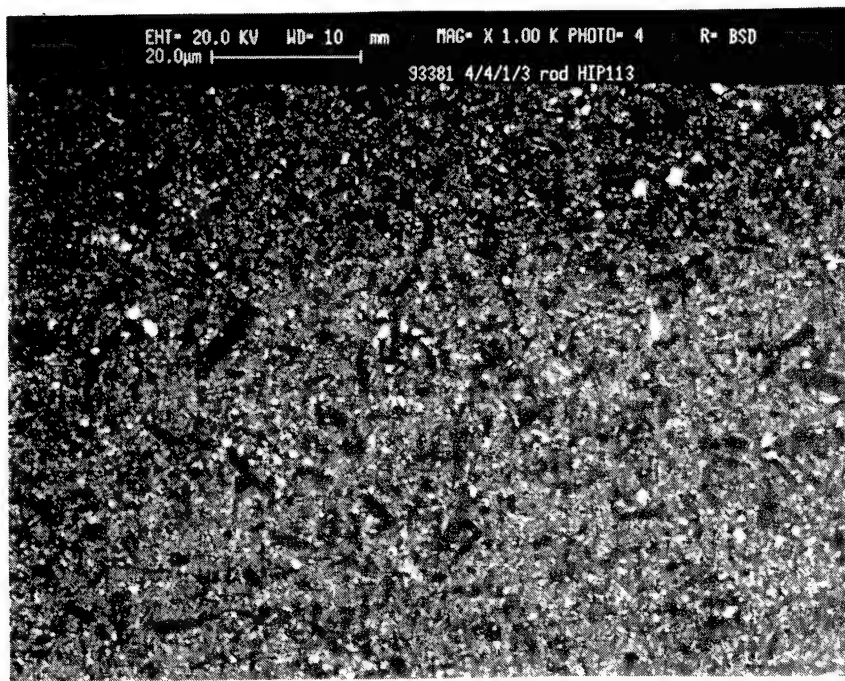


**Figure 4.3** SEM micrograph using Back-scattered electron imaging of a polished cross section of a sintered and HIPed silicon nitride ball.

### 4.3 Dimensional Variation

Table 4.3 is the dimensional tolerance specified by a major bearing manufacturer to assure the spherical form. The following terms are defined to conform to the specification.

*Blank Diameter (Dbm)* - Arithmetic mean of the smallest and largest diameters on a single ball blank.

*Blank Diameter Variation (VDb)* - The difference between the largest and smallest diameters measured on a single blank.

*Lot Mean Blank Diameter (Dbwm)* - Arithmetic mean of all individual blank diameter (Dbm) values in the sample.

*Mean Blank Diameter Variation (VDbm)* - Arithmetic mean of all individual blank diameter variation (VDb) values in the sample.

*Lot Diameter Variation (VDbwl)* - Difference between largest and smallest individual blank diameter (Dbm) values in the sample.

Twenty-five of the ball blanks were inspected. The variations in blank diameter and in lot diameter are listed in Table 4.4. Results showed that the high-speed green machining process can manufacture acceptable ball blanks within the specified tolerance ranges and with a low rejection rate (no parts were rejected in this batch of 25).

**Table 4.3 - Dimensional Requirements for As-Fired Ball Blanks**

Final Ball Size	Diameter Variation	
	Blank Mean VDbm	Lot Mean VDbwl
2-12 mm	< 0.25 mm	< 0.30 mm
12-30 mm	< 0.30 mm	< 0.40 mm
30-50 mm	< 0.40 mm	< 0.50 mm

**Table 4.4 - Dimensional Inspection of Deliverable Ball Blanks**

	Ball Blank	Requirement
Lot Mean Blank Diameter Dbwm	15.14 mm	
Mean Blank Diameter Variation VDbm	0.08 mm	< 0.30 mm
Lot Diameter Variation VDbwl	0.29 mm	< 0.40 mm

#### 4.4 X-Ray Inspection

Cercom contracted with BIR, Inc. of Lincolnshire, Illinois, to conduct a nondestructive evaluation study of the materials produced in this program using a technique called "high-resolution computed x-ray tomography". Both deliverable materials and those at various stages through the fabrication process were examined. There were two goals of this work. First, it was sought to evaluate the usefulness of high-resolution computed tomography as a quality control method in silicon nitride bearing element production. Secondly, it was desired to evaluate the materials produced in the program to see what types of flaws might tend to occur in them and to determine the frequency of occurrence.

The material in the following three subsections is excerpted from reports from BIR to Cercom that document their x-ray studies of the program materials.

#### **4.4.1 The Micro CT Technique**

Computed tomography (CT) is a cross sectional x-ray imaging technique with the capability of detecting density differences smaller than 0.1%, voids as small as 50  $\mu\text{m}$  and cracks smaller than 1  $\mu\text{m}$ . Since the x-ray absorption properties of a material depend on both density and atomic number, CT can also be used to measure effective atomic number by scanning at two energy levels. Dual Energy Micro CT (DE $\mu$ CT) has been used to characterize flaws in ceramic materials. CT inspection can characterize material properties, reject defective parts as early as possible in the processing, and insure defect-free final products. Two separate CT systems have been used to inspect four different ceramic formulations at four stages of processing.

Two CT system configurations were optimized for ceramic inspection. The first system is designed to scan multiple samples in a survey mode. The second system is designed to scan a single sample at the highest possible resolution for characterization of problems found in the survey mode. The performance of these two systems is shown in the Contrast Dose Detail (CDD) chart of Figure 4.4. CDD graphs demonstrate the actual resolution that the system achieves when x-ray noise, electronic noise, geometry, and human visual perception are taken into account. The CDD curves are produced from accurate simulations of these phenomena and have been correlated with measured results from the actual systems. Contrast percentage is plotted versus flaw diameter for detectability. Features to the right of a curve are visible, while features to the left are not. In this example, the performance of the two systems crosses over at flaw sizes of 0.16 mm. The survey system has better density discrimination for flaws larger than 0.16 mm while the high resolution system has better resolving power for flaws smaller than 0.16 mm. Density differences of 0.5% can be measured in 1 mm<sup>2</sup> areas.

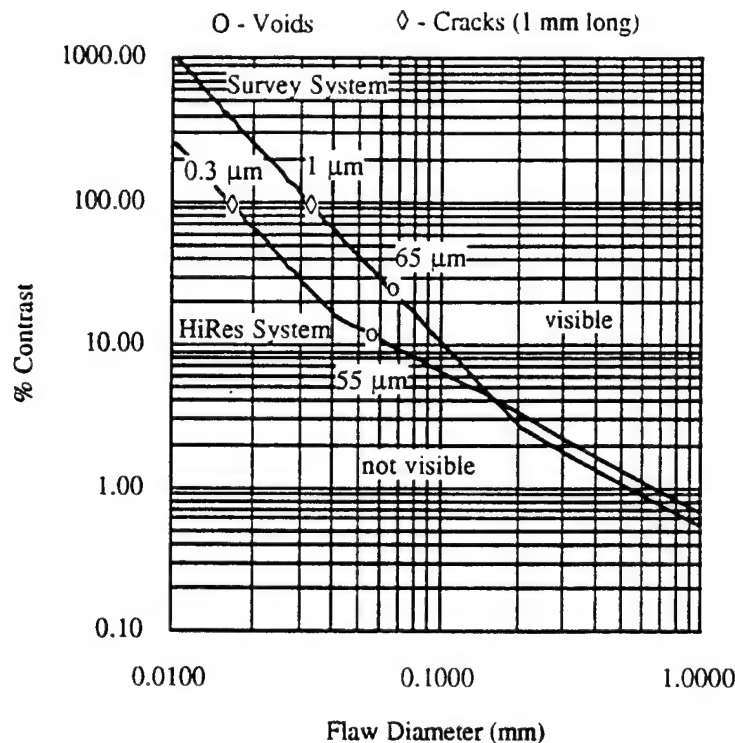


**Figure 4.4** The Contrast Dose Detail chart shows flaw detectability of the CT systems optimized for ceramic inspection. The HiRes system detects cracks measuring  $0.3 \mu\text{m} \times 1 \text{ mm}$  and  $55 \mu\text{m}$  voids.

Several types of defects in the finished product may lead to premature failures. Sub-surface voids weaken the structure and may eventually open up to the outside surface. High density inclusions on or near the surface may lead to uneven wear or damage to the races. Significant nonuniformity of density distribution may unbalance the balls and lead to excessive vibration. CT inspection has the potential to detect and identify such flaws.

#### 4.4.2 Inspection of In-Process Materials

CT inspection was utilized on samples of program materials after the four processing stages of isopressing, prenitriding, nitriding and sintering. The part dimensions and densities are shown in Table 4.5.



**Table 4.5 – Ceramic Bearing Blank Dimensions and Densities  
at Four Processing Points**

	Isopressed	Pre-Nitrided and Ground	Nitrided	Sintered
Diameter (mm)	19	13.9	14	12.5
Length (mm)	155	154	153	124
Density (g/cc)	1.67	1.60	2.35	3.28

The first inspection system was designed to survey multiple parts in the minimum time. A 320 kV x-ray source was used with a high resolution detector system to scan bundles of rods from end to end taking slices at 1 mm increments. The maximum area that can be scanned with this detector is 80 mm diameter but there is a trade-off between object size and resolution. To maximize resolution, the diameter was limited to 40 mm. Three 19 mm diameter parts, five 14 mm diameter parts or seven 12.5 mm diameter parts were grouped together in a 40 mm diameter tube. The airspace between parts was filled with glass beads in order to minimize density variations caused by the energy nonlinearity of x-ray absorption. The glass beads filled the cylinder out to a nearly uniform density which presents the ideal case for CT imaging. The fragile isopressed parts proved to be very susceptible to breakage through handling, so the evaluation was limited to pre-nitrided, nitrided and sintered parts.

Each CT slice was acquired in one minute so the inspection time for a 120 mm long group of seven sintered parts was two hours or 17 minutes per part. This time can be reduced to ten minutes per part by using a 420 kV x-ray source to produce more signal. A further reduction to five minutes is possible by scanning more parts in a larger holder at lower resolution. Sample results from the survey mode of scanning are shown in Figures 4.5 and 4.6.

In Figure 4.5, three different compositions of nitrided samples show overall density differences of 2%. Small low density areas are less than 0.5% lower than normal. A high density inclusion is seen in the sample at three o'clock. The density of this inclusion is 28% higher than normal. In Figure 4.6, all four formulations of sintered samples show overall density variations according to the formulation. A small void is seen in the center sample and a larger low density area is seen in the sample at one o'clock. The range of density seen in Figure 4.6 is  $\pm 1\%$ . In general, the sintered samples had very few indications as opposed to the other samples.

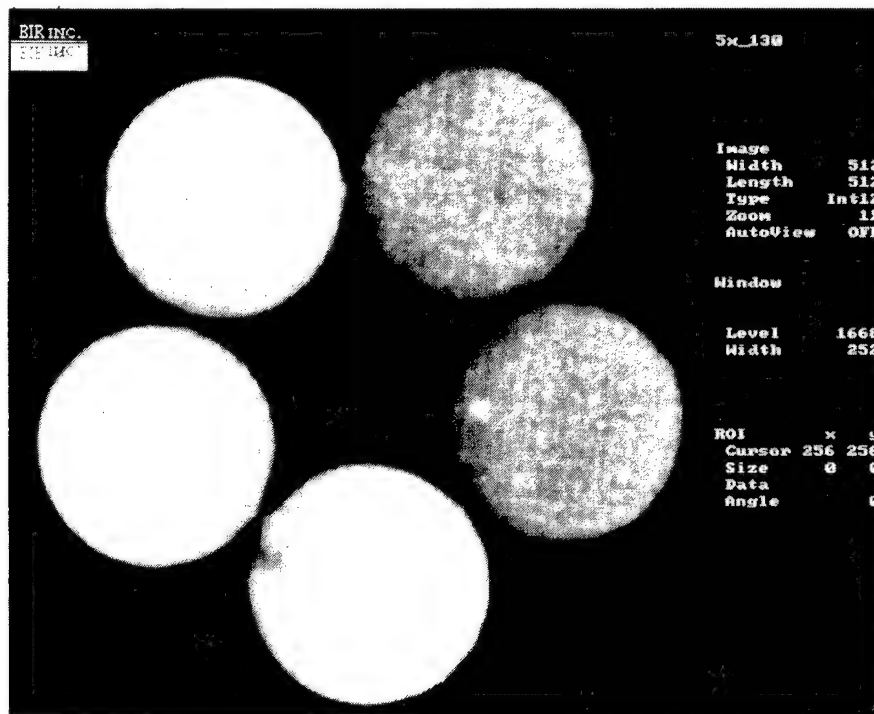


**Figure 4.5** CT slice of 14 mm nitrided samples.

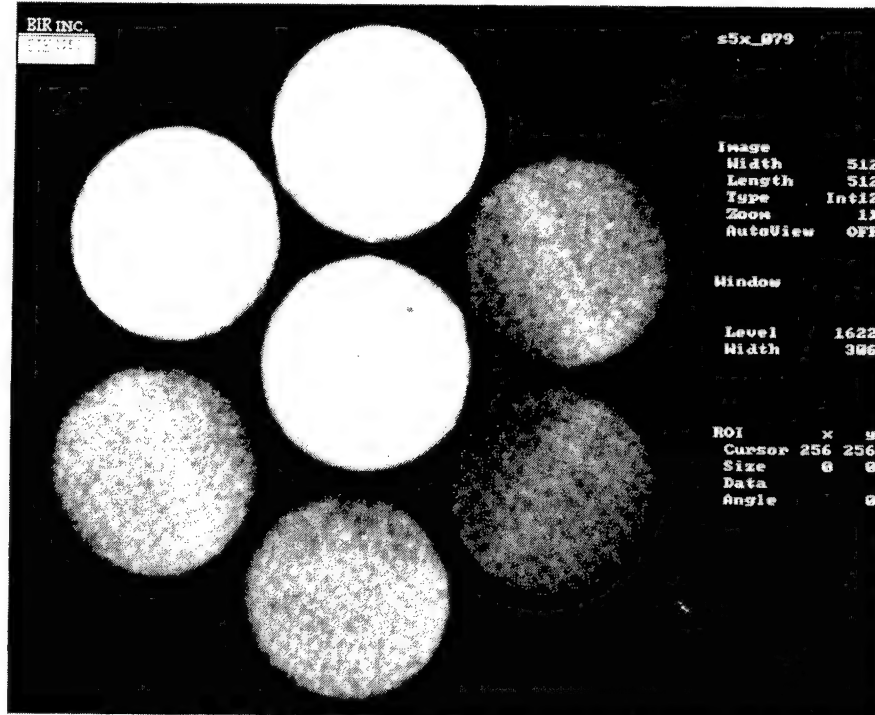


**Figure 4.6** CT slice of 12.5 mm sintered samples.

After the survey phase of scanning, several flawed parts were scanned on a high resolution CT system in order to characterize the flaws in greater detail. This system uses a 160 kV microfocus x-ray source and an image intensifier to acquire multiple slices during each x-ray exposure for increased throughput. In this case, three slices were acquired simultaneously to achieve a scan rate of three slices per minute. The results of these high resolution scans are shown in Figure 4.7 and 4.8.

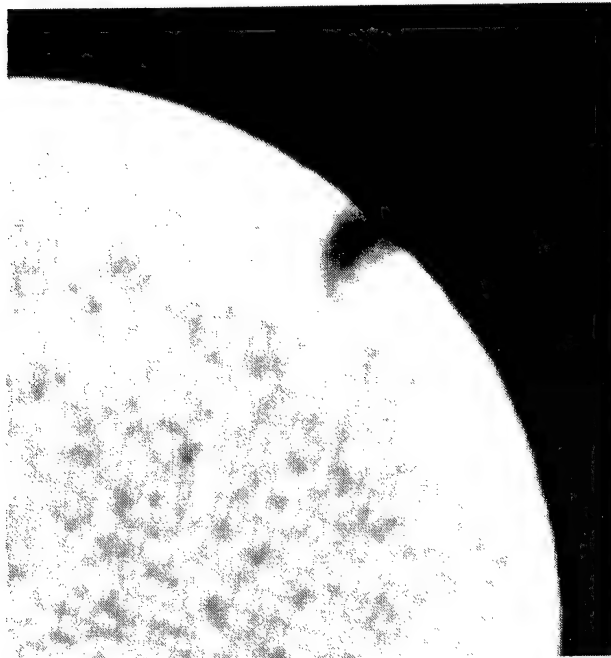


**Figure 4.7** *High resolution CT of near-surface void in nitrided sample 8/2/2 #2*

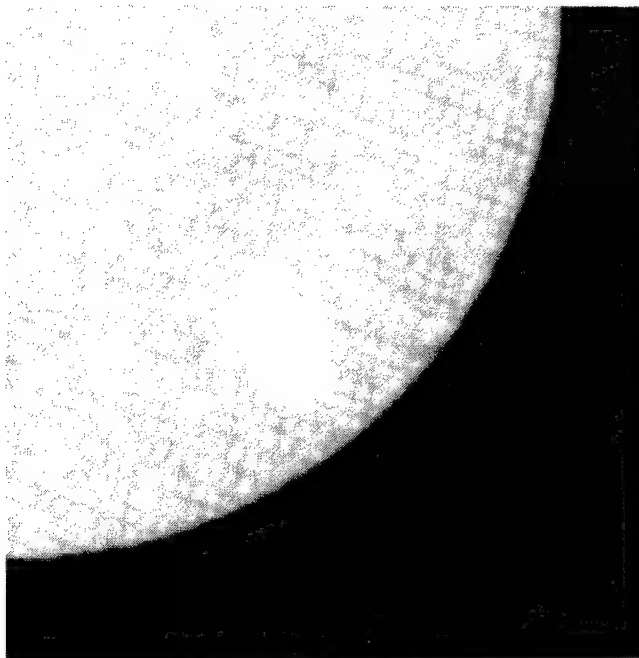


**Figure 4.8** *High-resolution CT of near-surface, high-density inclusion in nitrided sample 6/3/2 #2*

The high resolution scans have more detail than the survey scans while maintaining similar density discrimination capability. In Figure 4.7, a small void near the surface of a 14 mm nitrided part (8/2/2 #2) is surrounded by an area of slightly lower density. The high density inclusion of Figure 4.5 is seen in greater detail in the high resolution scan of the part (6/3/2 #2) in Figure 4.8.

The high density inclusion of Figure 4.8 was also analyzed using a dual energy CT technique. The scanner is first calibrated at two different energy levels using plastic and aluminum samples of known density and atomic number. In this case, the energy levels selected were 80 kV and 160 kV. The part was then scanned at the same energy levels and the results were processed to determine the effective atomic number of the high density inclusion. The inclusion's atomic number was found to be essentially the same as the surrounding ceramic material, suggesting that it was not a foreign material such as steel.

No cracks were detected in any of the samples. Small density variations were seen in all of the pre-nitrided and nitrided parts. These variations were typically less than  $\pm 1\%$  of the average density and 1 mm or smaller in diameter. Some low density areas were as large as 3 or 4 mm in diameter but were only 0.5% less dense than the surrounding material. The sintered parts had little evidence of the density variations seen in the pre-nitrided and nitrided parts. Instead of scattered small areas of slightly lower or higher density, the sintered parts showed very subtle density variations with annular ring structures. Since the CT system itself can introduce circular artifacts, care was taken to insure that the apparent annular density variation was actually a feature in the part and not caused by the CT system.

This was verified by placing the part off-center, rescanning, and noting that the density variation moved with the part instead of remaining at the CT system's rotation center. This annular density variation of the sintered part is

shown in Figure 4.9. This section was taken approximately 70 mm from the end of the 8/2/2 part marked #2.

The density variations of the prenitrided and nitrided parts are not seen in the sintered parts. This leads to the conclusion that such density variations are not necessarily a problem or precursors of significant flaws.

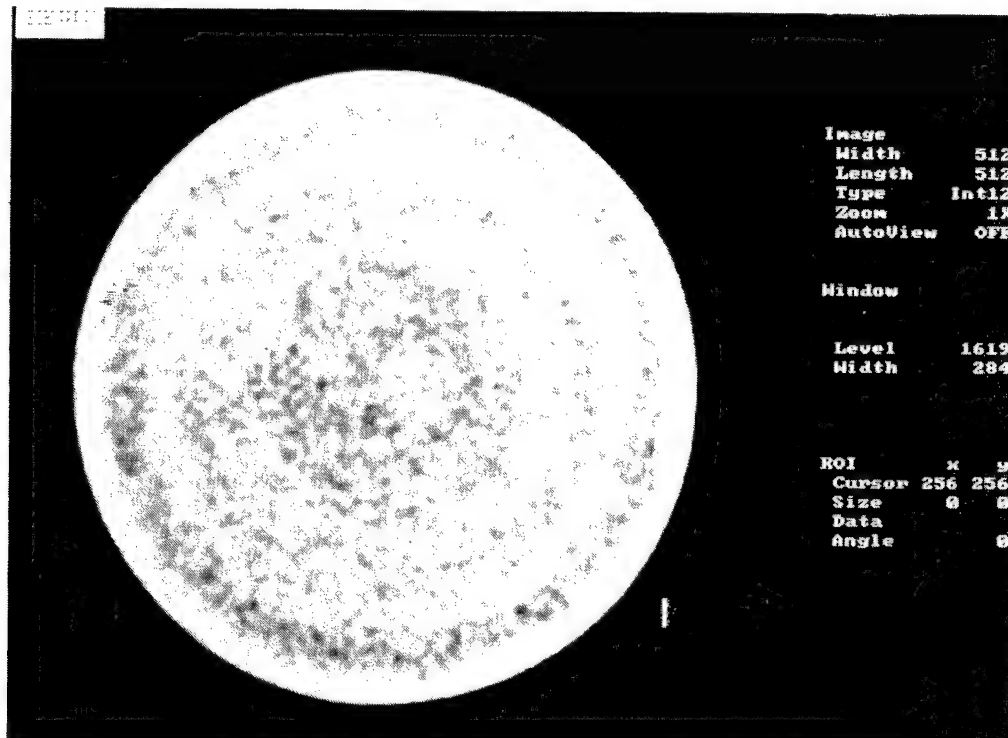


**Figure 4.9.** HiRes CT of sintered part (8/2/2 #2) showing annular density variations of 0.1%.

#### **4.4.3 Inspection of Deliverable RCF Specimens**

A set of 42 rolling contact fatigue samples measuring 12.5 mm in diameter by approximately 130 mm in length was scanned using the survey mode. Six samples at a time were scanned in a 38 mm diameter tube with glass beads used as a bolus or packing material to yield stable and uniform CT density values. A seventh sample at the center of the tube was used only to position the remaining six parts. A calibration error of the detector system produced artifacts at the center of the image that could be mistaken for flaws.

Thus at the end of the inspection process, the central part was moved to the outside and scanned with five other parts.

An improved detector system which allowed wider slices was used. The main difference was that an array of  $\text{CdWO}_4$  x-ray scintillator crystals was used as opposed to the GOS scintillator screen material. This new array features 768 crystals measuring 2.5 mm x 2.5 mm x 75  $\mu\text{m}$ . The 75  $\mu\text{m}$  dimension is used as the resolution aperture which also yields an improvement in resolution over the 100  $\mu\text{m}$  resolution of the GOS screen.

The scan parameters as shown below were slightly different than before:

Voltage	310 kV;
Current	5.2 mA;
Focus	1.8 mm;
Slice thickness	1.0 mm;
Slice increment	1.0 mm;
Scan time per slice	40 seconds;
Views per scan	600;
Samples per view	512;
Field of view	40 mm;
Image matrix	512 x 512;
Spatial resolution	75 $\mu\text{m}$ ;
Density resolution	1%.

The samples were grouped in sets of six parts, marked, and then scanned from one end to the other using 1 mm thick slices at 1 mm increments. Thus, approximately 140 slices were acquired for each batch. The images were reviewed by the operator as they were acquired. **No flaws were detected in any of the 42 samples.** There was no evidence of porosity, voids or high density inclusions. All images were archived to

magnetic tape in Unix TAR format. A typical example of one of the resulting images is shown in Figure 4.10.

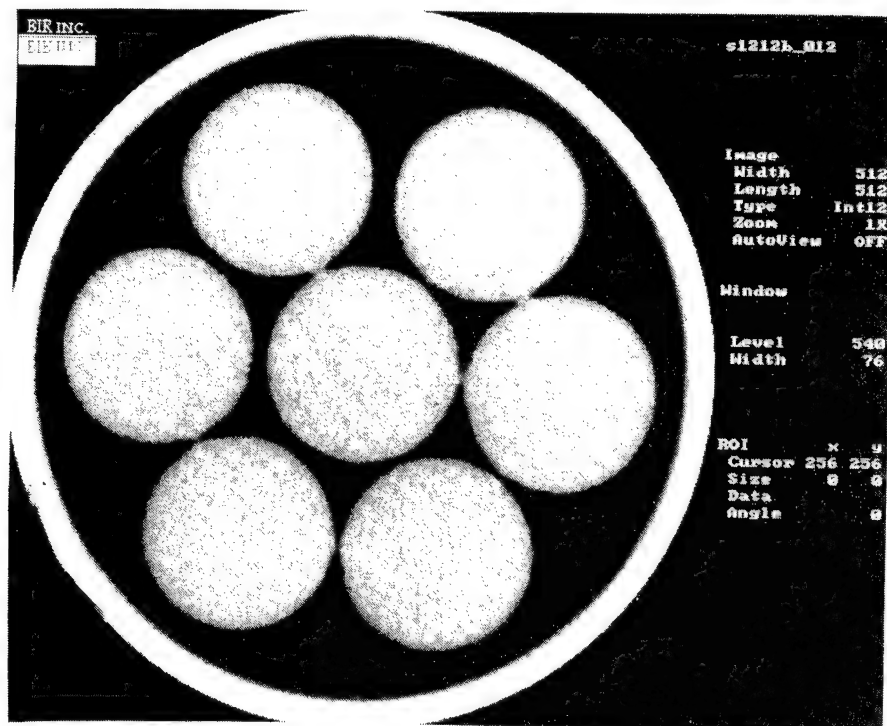


**Figure 4.10** A typical example of a x-ray tomographic image of the deliverable RCF specimens.



## 5.0

### SUMMARY

The objective of the program described in this report was to optimize the materials processing parameters used in silicon nitride rolling element fabrication to develop a process for producing materials of better quality than any others now available in the United States. Ball and roller bearing element blanks were fabricated in this program and delivered to the government for further evaluation.

The particular approach used in the present program takes advantage of the ability to form  $\text{Si}_3\text{N}_4$  / TiN particulate composites using reaction-bonded silicon nitride (RBSN) processing technologies. Foreign suppliers have demonstrated that silicon nitride-based materials with particulate additions of TaN or TiN perform exceptionally well as rolling elements in bearing applications. Exceptional performance not only includes long life during field testing, but also includes excellent lot-to-lot consistency.

These foreign materials are fabricated using mixtures of  $\text{Si}_3\text{N}_4$ ,  $\text{Y}_2\text{O}_3$ ,  $\text{Al}_2\text{O}_3$  and TiN or TaN powders. The starting materials for our program are Si,  $\text{Y}_2\text{O}_3$ ,  $\text{Al}_2\text{O}_3$ , AlN, and  $\text{TiO}_2$ . Titania is transformed *in situ* to TiN during the RBSN process. This unique approach of introducing TiN into  $\text{Si}_3\text{N}_4$  through the use of inexpensive  $\text{TiO}_2$  precursors produces a beneficial modification of the oxidation state of the liquid intergranular phase that alters the sintering kinetics and the ratio of beta-to-alpha phase silicon nitride.

In addition to the program objectives already stated, some ancillary objectives relating to process optimization have also been addressed, including:

- a) impart handleability to isopressed blanks through the use of prenitriding in lieu of traditional binder/plasticizer additions;
- b) demonstrate green machining as a high-rate, low-cost production technique;
- c) show the feasibility of thermal processing by using pressureless sintering, and
- d) demonstrate that  $\text{Si}_3\text{N}_4$  with TiN can be HIPed without the use of canning materials.

The hardware deliverables in this program were 1/2 in. diameter balls and 1/2 in. diameter, 6 in. long rods made from optimized  $\text{Si}_3\text{N}_4$  material. Both the balls and the rods were machined on a centerless grinder from prenitrided rods. The prenitriding process involves the interruption of the full nitriding cycle after just enough reaction bonding has occurred for the material to possess sufficient cohesive strength to withstand the grinding process. After grinding is completed, the parts are returned to the nitriding furnace and reacted to completion. Compared to more conventional ceramic processing where fugitive binders would be used to produce green strength, this method avoids the contamination of binder residue. It also permits greater control over the strength and brittleness of the part to be ground, so that the grinding process can be made more efficient. If the prenitriding is not sufficient, then the part strength is low and a high breakage rate may occur in the grinder. If the part is prenitrided too long, however, then it becomes too brittle and the grinding yield again suffers.

Another key process methodology adopted in this program is the use of hot isostatic pressing without reliance on glass envelopes. The usual practice employed in the HIPing of ceramic materials is to encapsulate the articles to be HIPed in glass. This glass softens at the processing

temperature to permit the transmission of isostatic pressure while blocking the passage of gas into the residual porosity within the part. The fabrication and later removal of this glass envelope is an expensive and technically difficult additional processing step which we hoped to circumvent. Successful efforts in this area will be described later in this report.

In this report, an 18 month program is described that sought to develop a manufacturing process and a material composition capable of yielding premium quality silicon nitride bearing balls and rolling elements. The program culminated in the production and delivery of 50 rolling contact fatigue specimens and 50 bearing ball blanks to the Government. An add-on segment to this program will continue through July of 1994, in which material composition will be optimized beyond the state achieved in the original program.

The work performed in this program consisted of extensive experimental and analytical work to develop roughly optimized process parameters for each of the unit processes which together constitute the manufacturing process for the bearing element blank materials. The word "blank" is used because Cercom did not perform the final machining and finishing operations necessary to create usable bearing elements. The end product of this work is in a form which the bearing manufacturer could use to fabricate finished components. The constituent unit processes are:

1. Powder Blending
2. Cold Isostatic Pressing
3. Pre-nitriding
4. Green Machining
5. Nitriding
6. Sintering
7. Hot Isostatic Pressing (HIP)

Each of these processes was studied as a separate task within the program. The first program task was to choose a material composition and to select and characterize the raw materials to be used in the process. All subsequent program tasks were based on each of the seven unit processes listed above. The methods of Statistical Design of Experiment (DOE) were used to make the most efficient use of our research resources. DOE methods were employed in the layout of test matrices and in the statistical analysis of results.

## 5.1 Powder Blending

In this task, the raw materials were selected and the blending conditions were optimized. The selected raw materials are listed in Table 5.1.

**Table 5.1 – Powders Selected for Use in Program**

Material	Supplier	Grade
Silicon	Permascand	Sicomil
Aluminum Oxide	Ceralox	HPA-0.5 AF
Yttrium Oxide	Nippon Yttrium Corp. (NYC)	Ultrafine, 99.9% pure
Aluminum Nitride	Neomat	
Titanium Oxide	Fisher Scientific	T315-500 (Anatase)

A range of material compositions was evaluated in the program and used in all of the process optimization tasks. The composition that was down-selected at the end of the program was the 4/4/1/3 composition, meaning 4%Y<sub>2</sub>O<sub>3</sub>- 4%Al<sub>2</sub>O<sub>3</sub> -1% TiO<sub>2</sub> -3%AlN by weight.

The experimental matrices performed to optimize blending conditions resulted in the following blending method: The powders are dispersed in a liquid vehicle consisting of an azeotropic mixture of ethanol and MEK with an added dispersing agent; the slurry is milled in a ball mill with silicon nitride

grinding media for 48 hours; the blended slurry is passed through a 40  $\mu\text{m}$  ultrasonic filter, and then oven dried; the dried cake is dry-milled in a ball mill for 1 hour, and then passed through 5 and 40 mesh screens. This blending method was demonstrated by SEM characterization to result in very uniform blending of powder constituents.

## **5.2 Cold Isostatic Pressing**

Two issues were addressed in this task, design and fabrication of a multiple-rod bag assembly, and selection of an optimum pressing pressure. For efficient manufacturing, it was necessary to design a rubber bag that could produce as many rods as possible in a single pressure cycle, given the size constraints of the Cercom cold isostatic press (isopress). The design used was a configuration having multiple closed-end rubber tubes descending from an upper filling bowl. A multiply-vented metal container fits around the outside of the tubes, keeping them straight during compression.

The relationship between pressure and green density was determined through a series of isopressing experiments. This work showed that increasing the pressure beyond 15 kpsi leads to only minimal increases in green density above 1.5 g/cc. The 15 kpsi pressure was adopted as the standard isopressing pressure because it produces an appropriate green density.

## **5.3 Pre-nitriding**

The objective of this task was to develop a process to impart sufficient strength to the isopressed rods by thermal treatment so that they could be efficiently machined in a centerless grinder. Both partial nitriding and argon sintering were evaluated, and the partial nitriding was found to be superior.

Isopressed rods fabricated from selected powder compositions were prenitrided using normal nitriding conditions, except that the nitriding times were substantially shortened. The prenitrided rods were evaluated by measuring the strength, density, open porosity and handleability in centerless grinding trials. The microstructure and uniformity were characterized using optical and scanning electron microscopy.

It was found that the optimum prenitriding treatment resulted in a 4% weight gain. This weight gain would be achieved by different nitriding cycle times, depending on the powder composition and furnace charge. The Cercom nitriding furnace is controlled by a nitrogen gas demand monitoring system. A 4% weight gain is thus achieved by running the furnace long enough to consume a quantity of nitrogen calculated to produce that weight gain. The actual length of time will depend on the quantity of material loaded into the furnace, and the temperature.

#### **5.4 Green Machining**

The objective of the green machining task was to machine prenitrided stock to size without failure. High-speed machining of the prenitrided stock was performed with a Glebar centerless grinder. This grinder could grind the rough rods to a uniform, fixed diameter, or grind spherical ball blanks from rough rod stock.

A summary of the results of the machining yield experiments is as follows: A rubber regulating wheel gives much better yield than an alumina regulating wheel. A feed rate of 1 to 2 inches per minute was better than 0.5 to 0.7 inches per minute in order to keep sufficient friction against the grinding wheel and maintain part rotation. There was also a direct relationship between yield and weight gain during prenitriding. The higher the weight gain, the higher the yield as well as heat generated during dry

grinding. It was found that using a rubber regulating wheel at 60 rpm traveling at 1 to 2 inches per minute, dry grinding will produce satisfactory balls with prenitride weight gains of 3 to 6 percent. With lower weight gains, faster feed rates are needed and with higher weight gains, slower feeds are called for.

## **5.5 Nitriding**

The work conducted in the nitriding task was not aimed at optimizing the nitriding process, but rather at studying the chemical and phase transformations that occur during nitriding, and using this information to optimize the starting composition of the material. The actual nitriding process used by Cercom was already optimized and is a routine production process.

Material samples from before and after nitriding were subjected to x-ray diffraction phase analysis and to chemical analysis by a variety of spectrometric methods. These analyses not only provided intergranular phase development information but also verified that all of the titania added to the starting blend was converted to titanium nitride during the nitriding process.

## **5.6 Sintering**

The goal for this task was to develop an optimized sintering cycle for the program materials. An optimized sintering cycle is defined as one where the temperature and time profiles result in a sintered density level sufficient for containerless HIPing, and which results in good material properties such as density, hardness and fracture toughness, and homogeneous microstructure. It was our strategy to conduct sintering on a pressureless basis (ambient).

Based on the results from this task, it was concluded that 1700°C (3092°F) was the optimum sintering temperature for the down-selected composition.

No significant difference was seen between nitrogen and an inert gas atmosphere, so the inert gas was selected, because it prolongs the life of the sintering furnace. The optimum sintering time was found to be 10 hours.

Low density RBSN retorts were used in place of the conventional packing powder scheme. The retort concept provided the required localized environment to ensure efficient sintering.

An important observation made during the sintering study was that the added titania appears to enhance the acicularity of  $\beta$ - $\text{Si}_3\text{N}_4$  grains.

## **5.7 Hot Isostatic Pressing**

This program employed the sinter-HIP approach to densification, that is, the parts were first sintered in a sintering furnace and then HIPed after reaching a critical density of at least 97 percent of theoretical density. At this level, no open porosity remains, and the parts can be HIPed without a container. Containerless HIPing is essential for efficient and economical manufacturing. The goal of the HIP studies was to determine the optimum HIP process conditions, i.e., temperature, holding time, pressure, and atmosphere.

HIP experiments were conducted using seven different material compositions. Temperatures between 1750°C (3182°F) and 1875°C (3407°F), pressures between 10 MPa (1500 psi) and 70 MPa (10,000 psi), and times between 2 and 14 hours were investigated. The HIPed material was characterized on a wide variety of parameters to determine the relationships between composition, processing conditions, physical and mechanical properties, and microstructure.

The optimum HIPing cycle was determined to consist of high temperature (1875°C (3407°F)), low pressure (34 MPa (5,000 psi)), and short soak time (30 minutes). The atmosphere is a mixture of argon and nitrogen.



Nitrogen is detrimental to the graphite furnace; therefore, the nitrogen partial pressure should be kept low to reduce the amount of furnace maintenance. However, the nitrogen partial pressure should be high enough for preventing microporosity. Results showed that 1.7 MPa (250 psi) of N<sub>2</sub> cold pressurization is sufficient.

## 5.8 Characterization of Final Materials

Using the downselected 4/4/1/3 composition (% Y<sub>2</sub>O<sub>3</sub>/Al<sub>2</sub>O<sub>3</sub>/TiO<sub>2</sub>/AlN) and fabrication process, a quantity of ball blanks and rolling contact fatigue (RCF) specimen blanks was fabricated as deliverable samples for the program. Additional material was also produced for testing. The program contract required the delivery of 50 ball blanks, 50 RCF blanks, and an unspecified quantity of rejected ball and RCF blanks for comparison. Material produced from the deliverable batch was subjected to mechanical properties testing. Some of the deliverable samples were also inspected by microfocus x-ray computed tomography.

An array of mechanical property testing was conducted on samples from the same batch of materials fabricated for delivery. The results of these tests are presented in Table 5.2. Microfocus x-ray computed tomography was used to nondestructively inspect the RCF specimens. This inspection did not detect any flaws or density fluctuations in any of the specimens.

**Table 5.2 – Results of Mechanical Testing on Deliverable Material**

Average Flexural Strength	135 kpsi (930 MPa)
Characteristic Flexural Strength	146 kpsi (1010 MPa)
Weibull Modulus	14.7
Fracture Toughness	5.60 MPa√m
Vickers Hardness	1485 kg/mm <sup>2</sup>

## 6. REFERENCES

1. R. N. Katz and J.G. Hannoosh, "Ceramics for High-Performance Rolling Element Bearings: A Review and Assessment," *Int. J. High Technol. Ceram.* **1**:69-79 (1985).
2. H. R. Baumgartner, "Evaluation of Roller Bearing Containing Hot-Pressed Silicon Nitride Rolling Elements," *Ceramics for High-Performance Applications*, Proc. 2nd Army Materials Technology Conference, Hyannis MA, Nov. 1 1973, J. J. Burke, A. E. Gorum, and R. N. Katz, editors, pp 713-727.
3. Y. P. Chiu and H. Dalai, "Lubricant Interaction with Silicon Nitride in Rolling Contact Applications," *ibid*, pp 589-607.
4. "Ceramic Mainshaft Roller Bearing Performance in a Gas Turbine Engine," Final Report dated February 1979 for the period August 1975-November 1978, Naval Air Propulsion Test Center, Contract N000140-76-C-1104.
5. G. W. Hosang, "Results and Design Techniques from the Application of Ceramic Ball Bearings to the MERADCOM 10 kW Turbine," Proc. AIAA/SAE/ASME/ASEE 23rd Joint Propulsion Conf., San Diego, 1987, AIAA-87-1844.
6. *ibid*.
7. L. C. Damon and R. A. L. Drew, "Dispersion Methods of Yttria in Silicon Nitride by Comminution," *J. Am. Ceram. Soc.*, **72**(1989), pp 495-98.
8. J. I. Goldshein et al., "Scanning Electron Micrography and X-Ray Microanalysis," Plenum Press: New York, New York (1981)), p 77.

## APPENDIX A

### Selection of Methods for Quality Assurance Procedure for Homogeneity

*1. Back-scattered electron imaging* – Back-scattered electron (BSE) imaging is an imaging mode of the scanning electron microscope (SEM) which shows atomic number contrast. Elements of higher atomic number,  $Z$ , appear brighter because they more efficiently back-scatter incident electrons.

The powder blends contain Si, Al, Ti, and Y elements. The atomic number of these elements and their back-scatter coefficients,  $\eta$ , are listed in Table A.1<sup>8</sup>. The back-scatter coefficients indicate the relative brightness of each element. The table shows that for BSE images of powder blends, Y is the brightest element, Ti is also brighter than Si, and Al is nearly identical in brightness to Si. Back-scatter images of powder blends showed bri

**Table A.1 – Atomic Number and Back-Scatter Coefficient,  $\eta$ , of Elements in Powder Blends.**

Element	Z	$\eta$
Si	13	0.15
Al	14	0.16
Ti	22	0.25
Y	39	0.34

**1.2 Energy dispersive x-ray mapping (EDXS)** – Energy dispersive x-ray mapping allows mapping of individual elements by selecting an EDX spectrum peak corresponding to the element of interest. This method was found to be a suitable technique for evaluating homogenization of  $\text{TiO}_2$  and  $\text{Al}_2\text{O}_3$ . It was observed that EDXS maps for Ti were uniformly bright for blends with Fisher anatase and had many bright spots for blends with ICD rutile. These results indicated that the anatase was well homogenized while rutile was not. Maps of Al showed only few bright spots, indicating  $\text{Al}_2\text{O}_3$  was well homogenized. Maps of Y were considered unnecessary because of the satisfactory imaging of Y by BSE imaging.

**1.3 Standard deviation of concentration** – This method was not selected for the quality assurance procedure because it was less effective than the other two methods.

**1.4 Quality assurance specification for homogeneity of powder blends for  $\text{Si}_3\text{N}_4$  bearings**

*a) Sample Preparation :*

For each lot to be tested, choose one isopressed rod of the smallest diameter available. Cut a disc of about 1 cm thickness from the rod using the diamond table saw. Gently trim the outer diameter of the disc so that it is about 15 mm, using a grinding wheel with 600 grit abrasive paper. Gently trim the disc to a final diameter of 10-12 mm by polishing with plain white photocopy paper. Polish the flat surface of the sample gently with plain white photocopy paper. Remove free powder from the surface with gas from an ultrajet dust remover can. Affix the sample to the aluminum SEM mount with carbon cement, polished side up. Have the sample coated with carbon.

*c) Sample Analysis :*

Analyze the sample with SEM using the following parameters:

Probe current = 1.00 nA

WD = 25 mm

Magnification = 1000 X

1)  $Y_2O_3$  : White Area

- a) Choose a magnification of 1000 X.
- b) Select the BSE image mode.
- c) Select a scan rate of 16 /sec.

- d) Adjust brightness and contrast on BSE amp so large  $Y_2O_3$  particles appear white against a gray background. Figure A.1 is an example of properly adjusted image.
- e) Select an area with a representative image.
- f) Frame average and take photo.
- g) Count the white areas of the specimen using the transparent grid shown in Figure A.2. The grid is made of 1200 elemental squares arranged in 48 larger blocks. For each block, count, to the nearest 1/8 square, the number of elemental squares which are white.
- h) Sum the number of elemental white squares and calculate the white area of the image in per cent according to:

$$W = (\# \text{ white squares} / 1200) \times 100 \%$$

Homogeneity of  $Y_2O_3$  is acceptable if W is less than 2 %.

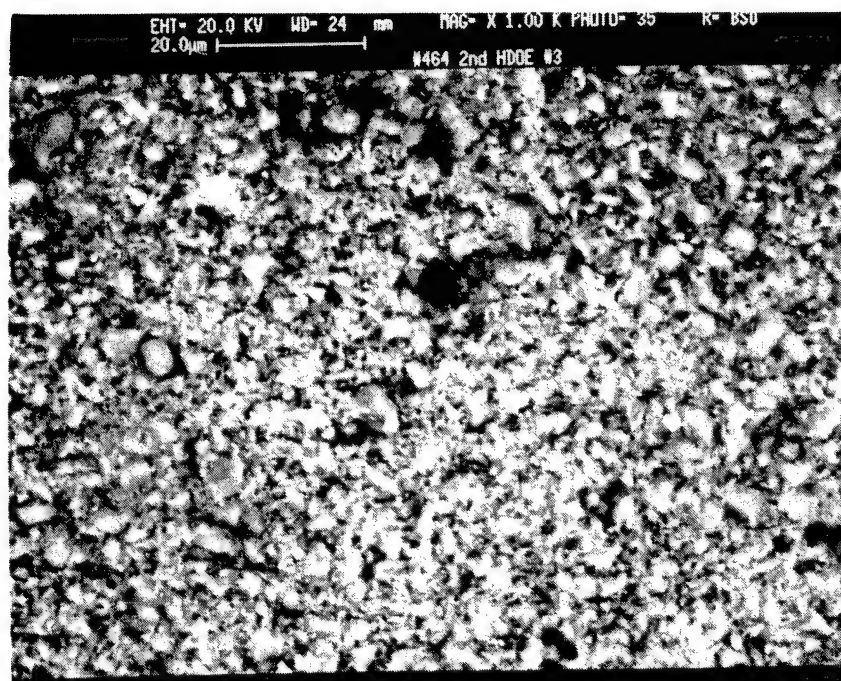


**Figure A.1** Properly adjusted BSE image.

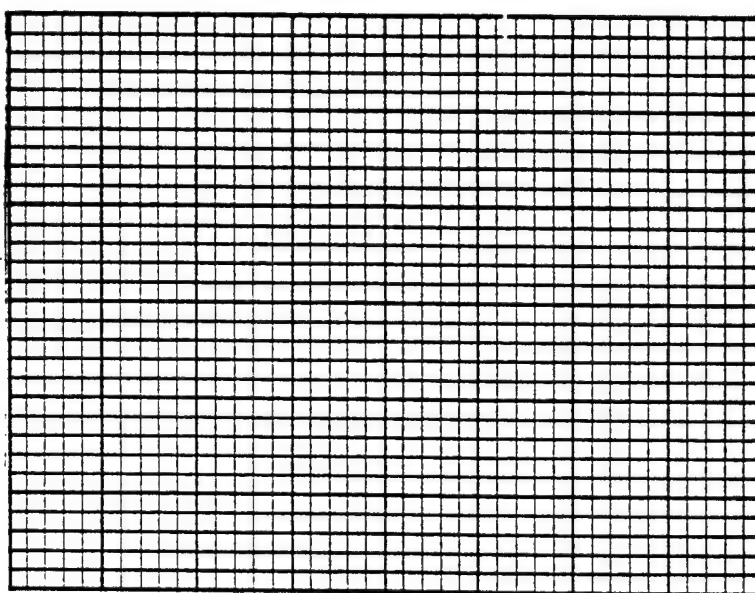


**Figure A.2** Grid for measuring white area of BSE imaging.

- h) Calculate the surface concentration of  $Y_2O_3$  particles  $\geq 10 \mu m$ ,  $n$ , according to  $n (\#/mm^2) = N/5.84$ .
- i) Homogeneity of  $Y_2O_3$  is acceptable if  $n$  is less than  $5/mm^2$ .

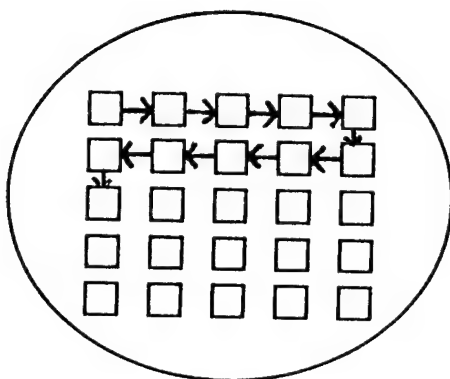


**Figure A.3** Traverse pattern for counting large bright spots in BSE images.

- 3)  $TiO_2$ : EDXS map
  - a) Choose a magnification of 1000 X.
  - b) While acquiring the x-ray spectra, adjust EDX detector position to maximize live count rate.
  - c) Select a window of 4.46 - 4.58 Kev.
  - d) Select the EDXS mode.
  - e) Select a scan rate of 2 /sec.
  - f) Collect the EDXS image for 45 min.



- g) Take photo.
- h) Homogeneity of  $\text{TiO}_2$  is acceptable if the image appears uniform and without any bright areas. Figure A.4 is a Ti EDXS photo of a sample with acceptable homogeneity of  $\text{TiO}_2$ .

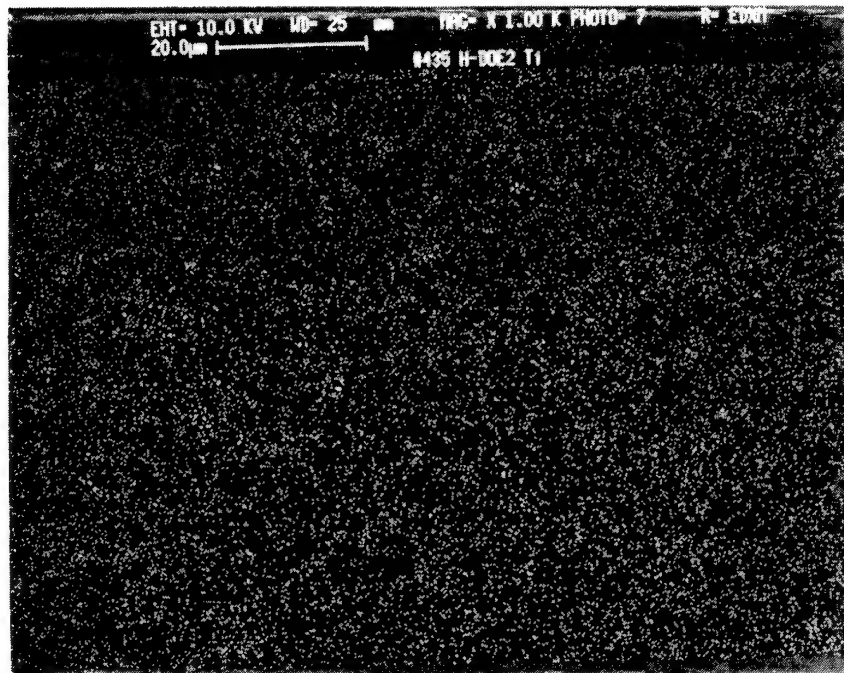


**Figure A. 4** EDXS photo for Ti of a sample with acceptable homogeneity of  $\text{TiO}_2$ .

#### 4) $\text{Al}_2\text{O}_3$ : EDXS map

- a) Choose a magnification of 1000 X.
- b) Leave the EDX detector position adjusted as described above.
- c) Select a window of 1.46 - 1.54 Kev.
- d) Select the EDXS mode.
- e) Select a scan rate of 2 /sec.

- f) Collect the EDXS image for 20 min.
- g) Take photo.
- h) Homogeneity of  $\text{Al}_2\text{O}_3$  is acceptable if the image has 5 or less bright areas larger than  $5\ \mu\text{m}$ . Figure A.5 is a Al EDXS map of a sample with one bright area. This sample has an acceptable homogeneity of  $\text{Al}_2\text{O}_3$ .

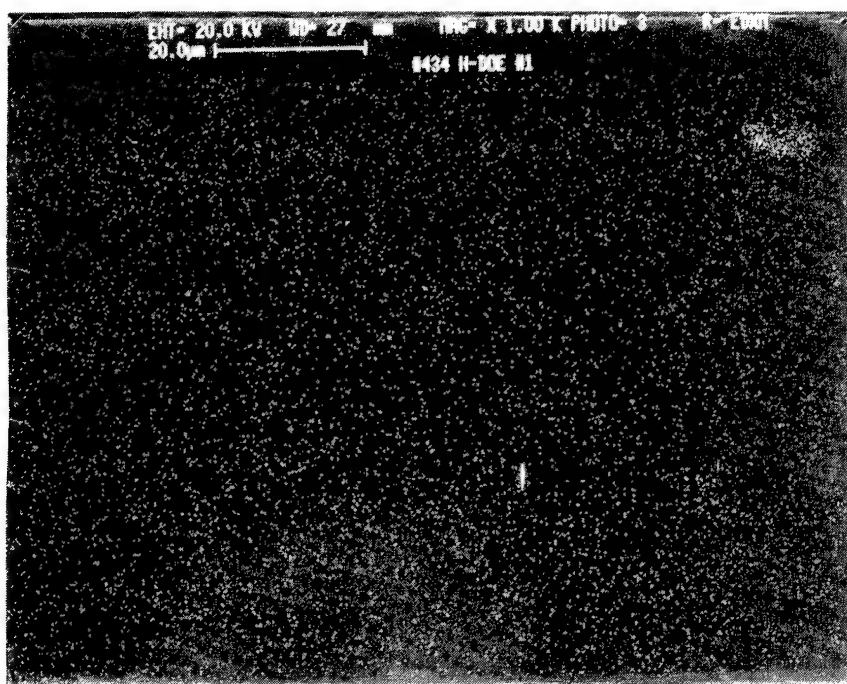


**Figure A.5** EDXS map of Al in a sample with acceptable homogeneity of  $\text{Al}_2\text{O}_3$ . The image has only one bright area.

## **APPENDIX B**

### **Evaluation Method for Classifying Microstructures**

Porosity is defined as pits or holes other than those caused by pull-out during sample preparation. Metallic phases are bright, highly reflective phases in the silicon nitride matrix material, visible at a magnification of 100X and smaller in size than 25  $\mu\text{m}$ . Intergranular or ceramic secondary phases are visible at a magnification of 100X and are either darker or lighter in color than the silicon nitride matrix. These phases are not highly reflective in nature. Inclusions are areas of metallic phases, ceramic-second phases, or combinations of both types greater than 25  $\mu\text{m}$  in size measured at the widest point.

The microstructural assessment is made on the distribution and size of the porosity, metallic and ceramic second phases. The assessments are then classified according to type:

Type A - uniform to 10  $\mu\text{m}$

Type B - uniform to 10-25  $\mu\text{m}$

Type C - defined by clustered morphology

The assessment also rates phase content by assigning a volume percent using comparison standards established by ASTM Standard 276. That is, optical micrographs of the material are first generated at 100 or 200X. The feature of interest is identified in the photomicrograph, for instance porosity, and then compared/matched to ASTM Standard images. The matching is

made not only on distribution of the feature (e.g., type A, B or C) but also on the observed volume percent. This matching process allows the rating or designation profile to be constructed. Table B.1 summarizes the assessment methodology and provides designation examples.

Table B.2 defines the allowable limits for each material class according to each microstructural feature, including maximum feature size. Note that for a Class I material the maximum allowable porosity, expressed in volume percent, cannot exceed 0.02. Additionally, individual pores cannot be greater than 10  $\mu\text{m}$  in size. Similar restrictions are placed on metallic and ceramic secondary phases.

**Table B.1 – Microstructural Assessment: Determination of the Presence, Level and Distribution of Porosity, Metallic Phases, Ceramic Second Phase and Inclusions**

ASSESSED PHASE	PREFIX	TYPE	RATING BASED ON VOLUME %	DESIGNATION EXAMPLES
POROSITY	P	A B C	02, 04  06, 08	PA02 PB04 PC08
METALLIC PHASES	M	A B C		MA04 MB02 MC06
CERAMIC SECOND PHASES	C	A B C		CA02 CB06 CC04

TYPE A - UNIFORM TO 10  $\mu\text{m}$

TYPE B - UNIFORM 10 TO 25  $\mu\text{m}$

TYPE C - DEFINED BY CLUSTERED MORPHOLOGY

EXAMPLE: POROSITY, TYPE AND RATING VOLUME % =  
DESIGNATION

**Table B.2 – Maximum Limits for Microstructural Features of Each Material Class**

Microstructure Feature		Material Class		
		I	II	III
Porosity:	- Volume %	0.02	0.06	0.06
	- Size (µm)	10	10	25
	- Rating	PA02	PA04	PB04
Metallic Phases:	- Volume %	0.2	0.6	0.6
	- Size (µm)	10	10	25
	- Rating	MA06	MA08	MB08
Ceramic 2nd Phases:	- Volume %	0.2	0.6	0.6
	- Size (µm)	25	25	25
	- Rating	CA06	CA08	CA08
		or CB06	CB08	CB08
		or CC04	CC08	CC08

TYPE A - UNIFORM TO 10 µm

TYPE B - UNIFORM 10 TO 25 µm

TYPE C - DEFINED BY CLUSTERED MORPHOLOGY

EXAMPLE: POROSITY, TYPE AND RATING VOLUME % =  
DESIGNATION

For example, Figures B.1 and B.2 are optical micrographs (200X) of two CERCOM manufactured materials, PSX and PSG-H respectively. The assessment procedure rates the Figure B.1 microstructure features as PA04, MA06 and CA08; a Class II material as indicated in Table B.2. In contrast, the HIPed PSG material represented by Figure B.2 is a Class I microstructure.

*Inclusions:* The number of ceramic, metallic or mixed inclusions observed in polished cross-sections should not exceed the limits given in Table B.3.

**Table B.3 – Maximum Number of Inclusions per cm<sup>2</sup> of Cross-Section**

Size of Inclusion (μm)	Material Class		
	I	II	III
200 -	0	0	1
100 - 200	0	1	2
50 - 100	1	2	4
25 - 50	4	8	16

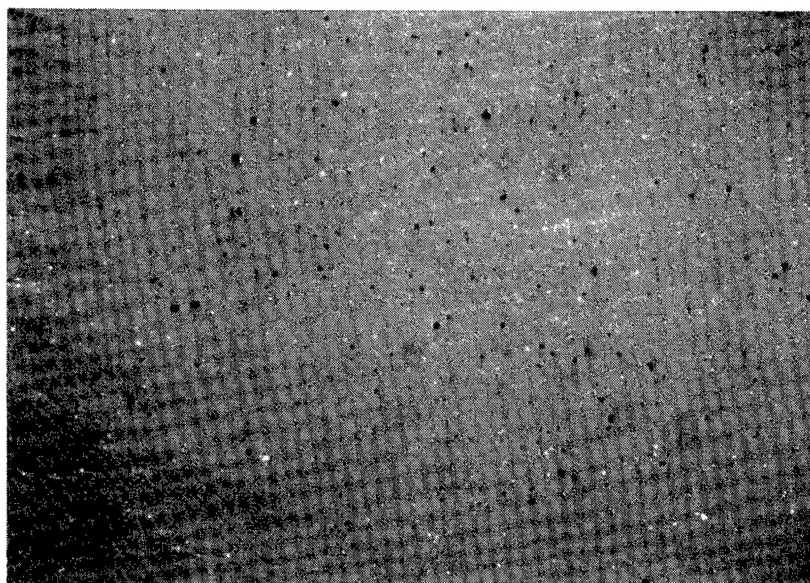


**Figure B.1** *Optical micrograph of a polished PSX Si<sub>3</sub>N<sub>4</sub> cross-section taken at 200X. The black and white "dots" constitute porosity and ceramic second phase, respectively. This microstructure is representative of a Class II material.*

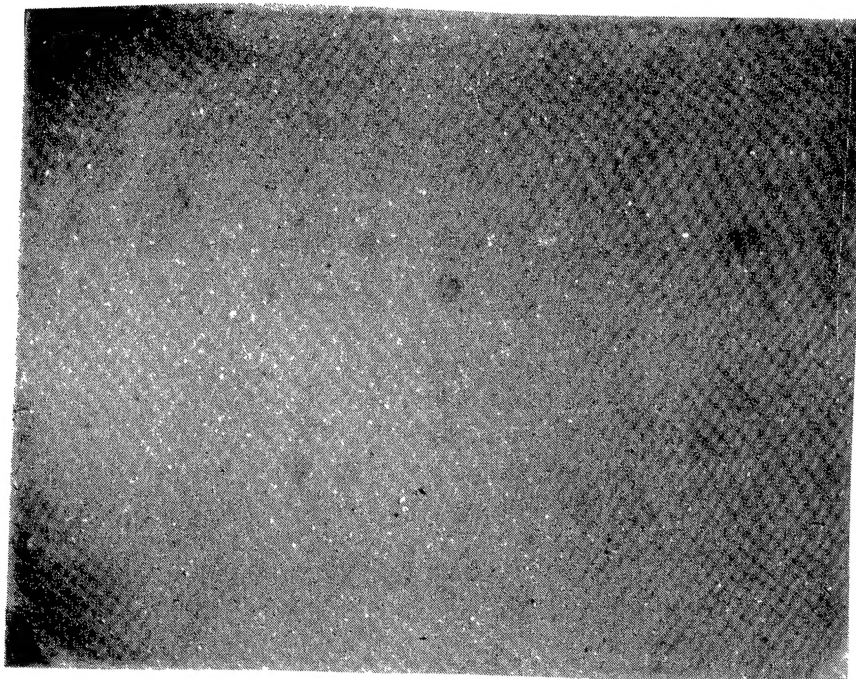


**Figure B.2** *Optical micrograph of a polished PSG-H Si<sub>3</sub>N<sub>4</sub> cross-section at 200X. The white "dots" represent the distribution of ceramic second phase. Absence of black "dots" shows that virtually all porosity has been eliminated during HIP treatment. The microstructure is representative of a Class I material.*

Vickers microhardness was measured using a 5 kg load. Toughness ( $K_{IC}$ ) was measured using Vickers indentation technique at 5 kg loading and calculated by the Nikhara equation as follows:

$$K_{IC} = 10.281 E^{0.4} P^{0.6} a^{-0.7} (c/a)^{-1.5} \text{ MPa}\cdot\text{m}^{1/2}$$

where  $a$  = mean half diagonal value ( $\mu\text{m}$ )

$c$  = mean half tip-to-tip crack length ( $\mu\text{m}$ )

$E$  = Elastic Modulus (GPa)

$P$  = Vickers Load (kg)

(the Elastic modulus for all calculations was assumed to be 310 GPa)